Investigation of Oxygen Defect Formation in Supported Vanadium Oxide Catalysts by Impedance Spectroscopy

Vorgelegt von Diplom-Ingenieur

Manuel Harth

aus Berlin

Von der Fakultät III – Prozesswissenschaften

der Technischen Universität Berlin

zur Erlangung des akademischen Grades

Doktor der Ingenieurwissenschaften

- Dr. Ing. -

genehmigte Dissertation

Promotionsausschuss:

Vorsitzender: Prof. Dr. Walter Reimers
Berichter: Prof. Dr. Helmut Schubert † / Prof. Dr. Matthias Kraume
Berichter: Prof. Dr. Hans-Dieter Wiemhöfer
Berichter: Prof. Dr. Reinhard Schomäcker

Tag der wissenschaftlichen Aussprache: 29.08.2012

Berlin 2013
D 83

Contents

1. Introduction

Light olefins like ethene or propene are very important chemicals used for the synthesis of various polymers or solvents. In Europe the largest amount of propene is synthesized via steam cracking processes (70 – 75 %), followed by fluid catalytic cracking (28 %) and to a small amount (2 %) by catalytic dehydrogenation. But these processes require high temperature (above 800 °C) and show poor selectivity. The necessity of elevated temperature means high energy consumption and thus generation of large amounts of carbon dioxide. Another disadvantage is the formation of coke which leads to a deactivation of the catalyst and requires costly regeneration. Or worse, the catalysts deactivate permanently due to the high reaction temperature. Hence, it is desired to develop reactions that run at much lower temperature. An alternative might be the oxidative dehydrogenation (ODH) of alkane that depending on the educt and catalyst proceeds at temperatures in the range of 200 – 600 °C. It is an exothermal redox reaction that is running in an oxygen containing environment and is thus less prone to coking. [1]

Many transition metal oxides are active for the ODH but especially vanadium oxide has been investigated due to its high redox activity [2,3,4,5]. It is a heterogeneous catalytic reaction in which the surface of the VO_x catalyst reacts with propane to form propene and water. This process follows a redox cycle known as Mars-van-Krevelen mechanism [6] (see Figure 1-1). In this mechanism donation of oxygen from VO_x plays an important role. In the reduction cycle lattice oxygen accepts hydrogen from the alkane and desorbs as water leaving a vacancy in the catalyst. The role of oxygen as a hydrogen acceptor is the reason for the reaction to be exothermal and therefore energetically favourable in contrast to normal dehydrogenation reactions [7]. These vacancies are then refilled from the gas phase oxygen in the reoxidation cycle. In this part transport of oxygen ions through the lattice is assumed and thus the oxidation can occur at a different site than it was reduced.

For many reactions pure vanadium pentoxide is not very active or selective but it is found that vanadium oxide supported on different metal oxides shows improved performance. The type and dispersion of vanadia species depends on the loading and their catalytic properties are strongly altered by the support [2,3,8,4,9,10,11,12]. The nature of this effect is diversely

discussed in the literature. Some correlate the catalyst's activity to the TPR reducibility [8] or to the Sanderson electro-negativity [9] and in theoretical investigation the oxygen defect formation enthalpy as a reactivity descriptor is tested [13,14,15,16,17,18,19].
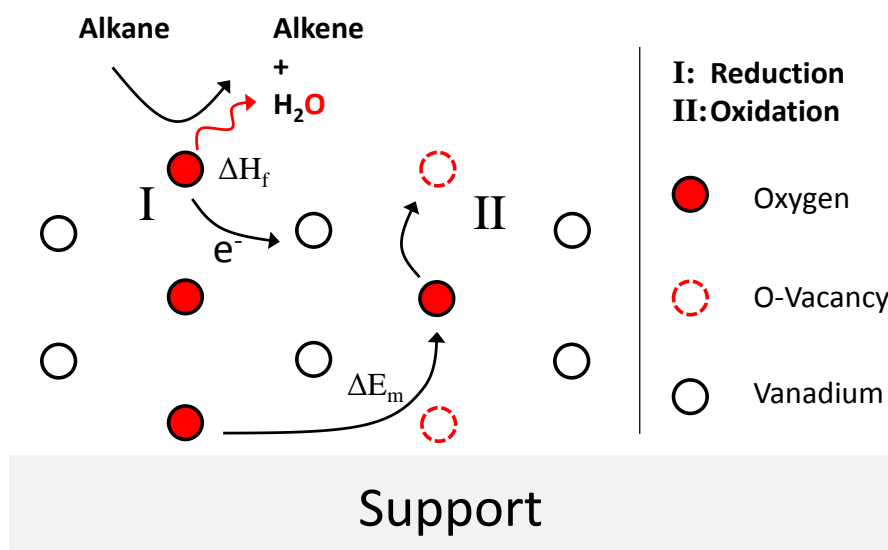
Figure 1-1: A Mars-van-Krevelen-like reaction mechanism. On reduction electrons are injected into the catalyst and are localized at nearby vanadia centres. Oxidation may occur through lattice diffusion. Thus, oxygen uptake may take place at a different site than it was reduced.

In this work impedance spectroscopic experiments are used to investigate the defect formation processes and to study the impact of solid state aspects on catalytic properties. This is possible because electronic and ionic charge carriers are exchanged on reduction and oxidation and thus enable us to use conductivity experiments as a probe.

At first in Chapter 4.1.1 the properties of the pure vanadium pentoxide are investigated and a method is developed that allows experimental determination of oxygen defect formation enthalpies ΔH_f. Then supported catalysts are examined in order to elucidate its effect on the solid state properties. For gaining deeper insight into transport paths, conduction mechanism, and the redox properties of the complex systems a systematic approach is chosen and starting at systems of very high loading (Chapter 4.1.2) the amount of vanadium pentoxide is successively lowered (Chapter 4.1.3) until monolayer coverage catalysts are investigated (Chapter 4.1.4). Then in Chapter 4.2 follows a discussion on the origin of the effect of the support on the solid state properties and finally, its impact on catalysis is discussed in Chapter 4.3.

2. Basics

2.1. Transport Properties

The total conductivity (σ_t) of a solid is the sum of all partial conductivities (σ_a):

$$\sigma_t = \sum_a (q_a \mu_a c_a) \qquad \qquad 2\text{-}1$$

The major charge carriers are ions (i), electrons (e) and electron holes (h). Therefore, equation (3-4) can be expressed as:

$$\sigma_t = \sigma_i + \sigma_e + \sigma_h \qquad \qquad 2\text{-}2$$

$$\sigma_t = \sum_i (z_i q_i \mu_i c_i) - q_e \mu_e c_e + q_h \mu_h c_h \qquad \qquad 2\text{-}3$$

The number of effective charges is z, q the magnitude of electronic charge, μ the mobility and c the carrier density. Therefore, two parameters, the carrier density and mobility, can be modified in order to enhance the conductivity. [20]

The mobility depends on several parameters. Examples are the potential barrier for ion migration, the polarizability of the lattice and electrostatic interactions of the moving charge carrier with its surroundings. There are different strategies to increase the carrier density: (1) A classical approach is homogeneous doping with aliovalent ions that are dissolved in the matrix of the solid conductor. In order to maintain electrical neutrality, defects of opposite charge are formed and hence the concentration of charge carriers is increased. (2) Another possibility to generate defect is non-stoichiometry. Here, via a gas phase reaction the oxide is reduced or oxidized and excess vacancies or interstitials are formed. With this process ionic and electronic conductivity is modified. (3) Further influence on the charge carrier concentration have interface effects like space charge or chemical strain. [21]

In the following chapters the basics of defect chemistry is discussed and applied to the ionic and electronic conduction mechanism.

2.1.1. Defects in Solids

Every well ordered solid exhibits deviations from the perfect lattice structure when the temperature is raised above absolute zero. These irregularities are called defects and have a

significant influence on physical and chemical properties in particular on the transport of charge carriers and are therefore discussed in the following.

2.1.1.1.1 Ionic Disorder

The ionic disorder is shown and discussed for a model oxide MO_2 that forms predominantly anti-Frenkel type defects. This intrinsic defect structure is well known for ionic conducting oxides like ZrO_2, ThO_2 and CeO_2. By forming anti-Frenkel defects, the anionic sublattice equilibrates with anionic vacancies and interstitial positions [22,23,24,25,26].

Using the Kröger-Vink notation [27] this defect reaction can be written as:

$$M_M^x + O_O^x \leftrightarrow M_M^x + O_i^{''} + U_O^{\bullet\bullet} \qquad\qquad 2\text{-}4$$
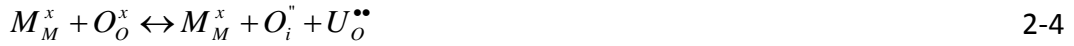
M_M^x is a neutral metal cation, O_O^x is a neutral oxygen on its lattice position, $O_i^{''}$ a twice negative charged (in respect to the lattice) oxygen interstitial and $U_O^{\bullet\bullet}$ is a twice positive charged oxygen vacancy. Usually the symbol $V_O^{\bullet\bullet}$ is used for the vacancy. But due to the vanadium investigated in this work, vanadium will be V and a vacancy U. This defect reaction shows, that the cationic sublattice is not altered by the anti-Frenkel defects.

Usually the pure oxides do not exhibit high ionic conductivity but this can be altered by generating further defects. This is done by doping with cations of lower valence. These substitute the cations in the lattice and introduce large amounts of point defects. An example for doping MO_2 with a trivalent impurity is given in reaction 2-5:

$$M_2^{'}O_3 \leftrightarrow 2M_M^{'} + U_O^{\bullet\bullet} + 3O_O^x \qquad\qquad 2\text{-}5$$

For 2 M^{3+} substituted for M^{4+} a vacancy is formed in order to maintain electroneutrality.

2.1.1.1.2 Electronic Disorder

Many ionic conductors exhibit partial electronic conduction. This can be an intrinsic property of the material. Electrons are thermally activated to the conduction band generating a hole in the valence band:

$$0 \leftrightarrow e^{'} + h^{\bullet} \qquad\qquad 2\text{-}6$$

But due to the large band gap of ionic oxides (above 2 eV) the contribution of intrinsic conduction is negligible.

Electronic conduction due to extrinsic disorder is more common. This may arise due to impurities generating donor or acceptor states as known from semiconductors. But electronic defects can also evolve due to deviations from stoichiometry. Therefore, in oxides, it can be altered due to changes of the chemical potential of oxygen in the atmosphere [28].

Partial Pressure Dependency

At high oxygen partial pressure, oxygen will be incorporated into the lattice filling oxygen vacancies. In order to maintain electroneutrality, electron holes are formed:

$$1/2 O_2 + U_O^{\bullet\bullet} \rightarrow O_O^x + 2h^\bullet \qquad \text{2-7}$$

In reducing conditions (low oxygen partial pressure) oxygen is extracted from the lattice forming an oxygen vacancy and two electrons:

$$O_O^x \rightarrow 1/2 O_2 + U_O^{\bullet\bullet} + 2e^{'} \qquad \text{2-8}$$

The activity of lattice defects in a solid solution is approximately identical to the concentration because it is considered as dilute species [29]. Due to the highly disordered lattice, large amounts of point defects are present (reactions 2-7 and 2-8). Thus, the concentration of $[O_O^x]$ or $[U_i^x]$ is taken as constant when the oxygen partial pressure is changed. Therefore, following equilibrium constants result for reaction (2-7) and (2-8):

$$K_h = \frac{[h^\bullet]^2}{p_{O_2}^{1/2} \cdot [U_O^{\bullet\bullet}]} \qquad \text{2-9}$$

$$K_e = p_{O_2}^{1/2} \cdot [e^{'}]^2 \cdot [U_O^{\bullet\bullet}] \qquad \text{2-10}$$

The defects that are formed are strongly partial pressure dependent. Only the concentration of the defects formed by substitution doping is virtually partial pressure independent because their quantity is so large, that the concentration change is negligible. Thus, their concentration is assumed to be constant:

$$[U_O^{\bullet\bullet}] \approx const. \qquad \text{2-11}$$

The electronic defect concentration is a function of the partial pressure and these are usually illustrated in a Kröger-Vink-diagram diagram (Figure 2-1).
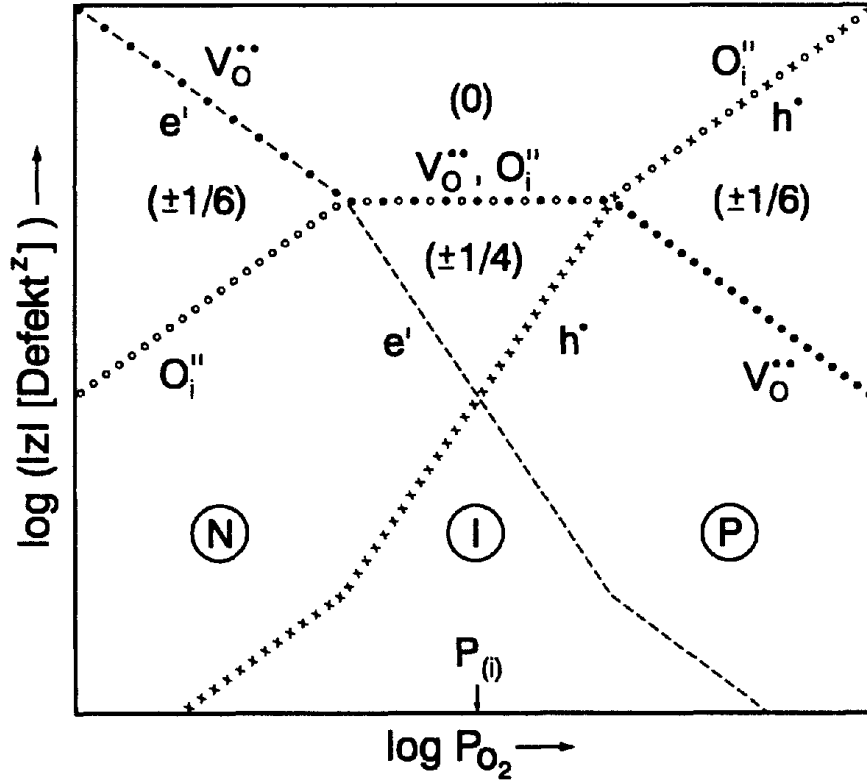
Figure 2-1: Kröger-Vink-digram. The defect concentration as a function of partial pressure is shown. P indicates the p-type conduction region, I the ionic and N the n-type region. [30]

At high partial pressure a p-type dominated region according to equation 2-7 is found and in this pressure range, the electroneutrality condition is:

$$2[U_O^{\bullet\bullet}] = -[h^{\bullet}]$$
2-12

This gives with equation 2-9 a partial pressure dependency of the defect electron concentration of +1/6:

$$K_h = -1/2[h^{\bullet}]^3 p_{O_2}^{-1/2}$$
2-13

$$[h^{\bullet}] \propto p_{O_2}^{1/6}$$
2-14

At low oxygen partial pressure the n-type conductivity dominates and the electroneutrality condition is:

$$2[U_O^{\bullet\bullet}] = [e^{'}]$$
2-15

Using equation 2-8 for the formation of electronic defects a partial pressure dependency of -1/6 is found:

$$K_e = 1/2 \left[e^{'} \right]^3 p_{O_2}^{1/2} \qquad\qquad 2\text{-}16$$

$$\left[e^{'} \right] \propto p_{O_2}^{-1/6} \qquad\qquad 2\text{-}17$$

At intermediate partial pressure the ionic defects exhibit the highest concentration and as already discussed their concentration is partial pressure independent. Thus, the equations 2-13 and 2-16 change to:

$$K_h = -1/2 \left[h^{\bullet} \right]^2 p_{O_2}^{-1/2} \qquad\qquad 2\text{-}18$$

$$K_e = 1/2 \left[e^{'} \right]^2 p_{O_2}^{1/2} \qquad\qquad 2\text{-}19$$

Hence, in the ionic conducting domain, the concentration of electrons and defect electrons are proportional to +1/4 and -1/4, respectively.

According to equation 2-1 the conductivity is directly proportional to the charge carrier concentration and therefore at constant mobility the conductivity exhibits the same pressure dependency as discussed above.

2.2. Impedance Spectroscopy

Electrochemical impedance spectroscopy (EIS) is a versatile method that allows investigation of dynamic processes of charged particles. Material properties like conductivity, mobility and dielectric constants can be investigated and the method gives the possibility to characterize transport mechanisms in the volume or at interfaces like redox and diffusion processes. Using EIS the frequency dependent conductivity can be investigated over a broad bandwidth (mHz to MHz) giving thus the possibility to resolve transport processes exhibiting different time constants. Detailed information can be found in [31].

Impedance spectroscopy uses an alternating voltage U^{*} and the resulting alternating current I^{*} is analysed in respect to phase difference φ and amplitude. This is used to calculate the frequency dependent impedance Z of the system. For the interpretation the resulting impedance plot is modelled by using an adequate equivalent circuit in order to gain insight into the electrochemical processes. The most commonly used elements are resistive *(R)*, capacitive *(C)* and inductive *(L)* elements. These are connected in series or parallel and can be completed using further elements for the description of e.g. diffusion processes.

If an alternating voltage U^*

$$U^* = U_0 \exp j(\varpi t + \varphi_U)$$

2-20

is applied to an electrochemical cell an electrical current I^* flows through the sample:
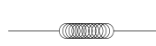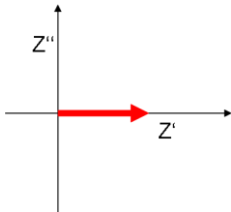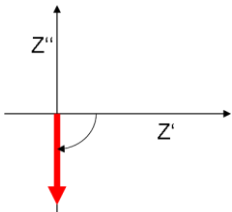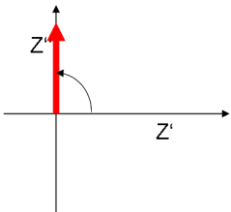
$$I^* = I_0 \exp j(\varpi t + \varphi_I)$$

2-21

Current and voltage are described by the amplitude, I_0 and U_0, the complex number j, the pulsatance $\varpi = 2\pi\upsilon$ with the frequency υ, and the phase difference φ_U and φ_I. The phase difference between voltage and current is given by $\varphi_U - \varphi_I = \varphi$. According to Ohm's law the complex impedance is

$$Z = \frac{U_0}{I_0} \exp j(\varphi_U - \varphi_I) = Z_0 \cos\varphi + Z_0 j \sin\varphi = Z' + jZ''.$$

2-22

Z' is the real and Z'' is the imaginary part. Some elements have a frequency dependent impedance and thus the characteristics of the three basic elements are depicted in Table 2-1:

Table 2-1: Frequency dependency of the basic elements for the equivalent circuits. The red arrow indicates the direction of increased frequency.

Impedance Element	Resistance	Capacity	Inductance
Symbol			
Impedance	$Z = R$	$Z = (j\varpi C)^{-1}$	$Z = j\varpi L$
Nyquist Plot			
Phase	$\varphi = 0°$	$\varphi = -90°$	$\varphi = 90°$

The ohmic resistance is a frequency independent element and takes only real values. While the capacity and inductance take only imaginary values. This gives for the capacity a phase difference of - *90°* and for the inductance a value of *+ 90°*.

Usually the equivalent circuits consist of several elements connected to a network and the overall impedance is calculated according to Kirchhoff's laws. Hence, the impedance of a

series connection is the sum of all elements while for a parallel connection it is the sum of the reciprocal values. But real samples contain inhomogeneities and thus show a deviation from the perfect behaviour of the equivalent circuit elements. Responsible is a distribution of macroscopic material properties like a rough electrode that shows behaviour different from a perfect capacitor and can be modelled using a constant phase element (CPE). The impedance of the CPE is

$$Z_{CPE} = A(j\varpi)^{-m} \qquad\qquad 2\text{-}23$$

The distribution of the properties is modelled by the variables A and α. For $m=1$ and $A=1/C$ the CPE corresponds to an ideal capacitor. For $m=0$ and $A=R$ it is equal to a resistance and for $m=-1$ and $A=L$ it describes an inductive element. For $m=0$ it is the Warburg diffusion impedance. [32,33].

The frequency dependent impedance can be shown in a Nyquist plot (Figure 2-2). In this diagram the imaginary and real part are depicted for every frequency. Therefore the frequency information is lost but the arrow indicates the direction of increasing frequency.
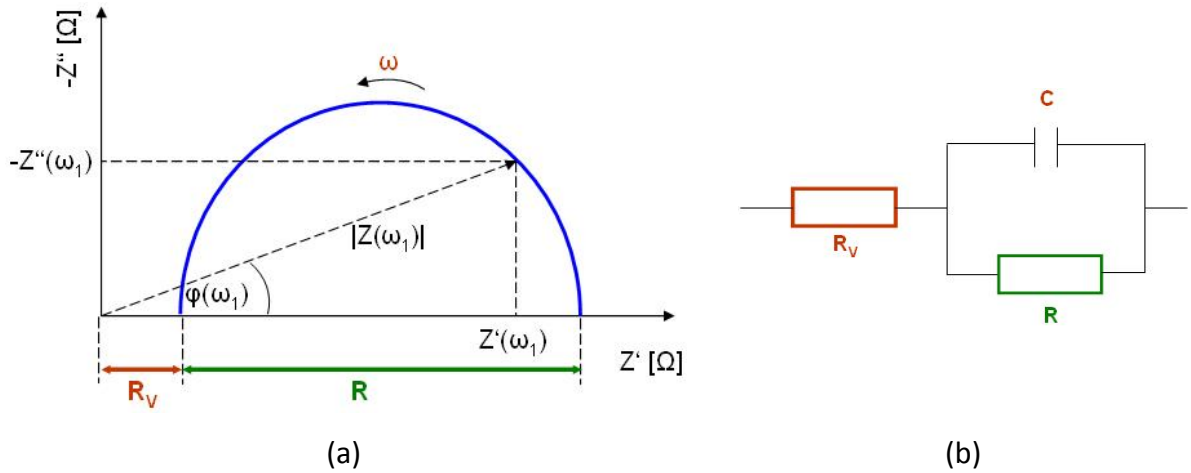
Figure 2-2:   (a) Nyquist plot for parallel RC-circuit with a series resistance R_V. (b) Corresponding equivalent circuit.

In Figure 2-2 the Nyquist plot for a parallel RC-circuit with a resistance in series is depicted and the impedance of this equivalent circuit is calculated as follows:

$$Z(\omega) = R_V + (1/R + j\varpi C)^{-1}. \qquad\qquad 2\text{-}24$$

For an increase of the pulsatance $\varpi \to \infty$ the second term vanishes and the impedance takes only real values:

$$Z(\varpi \to \infty) = R_V. \qquad\qquad 2\text{-}25$$

If the frequency takes very small values ($\varpi \to 0$), then, as shown in Figure 2-2, the impedance is the sum of R_v and R:

$$Z(\varpi \to 0) = R + R_V.$$

2-26

The maximum of the imaginary part is found at the pulsatance:

$$\varpi_{\max} = (RC)^{-1}$$

2-27

Another diagram for the impedance is the Bode plot (Figure 2-3). It shows the absolute value of the impedance $|Z|$ and the pulsatance as a function of the frequency. This diagram contains the same information but the frequency information is not lost. But the interpretation in respect to choosing the equivalent circuit is easier in the Nyquist plot.
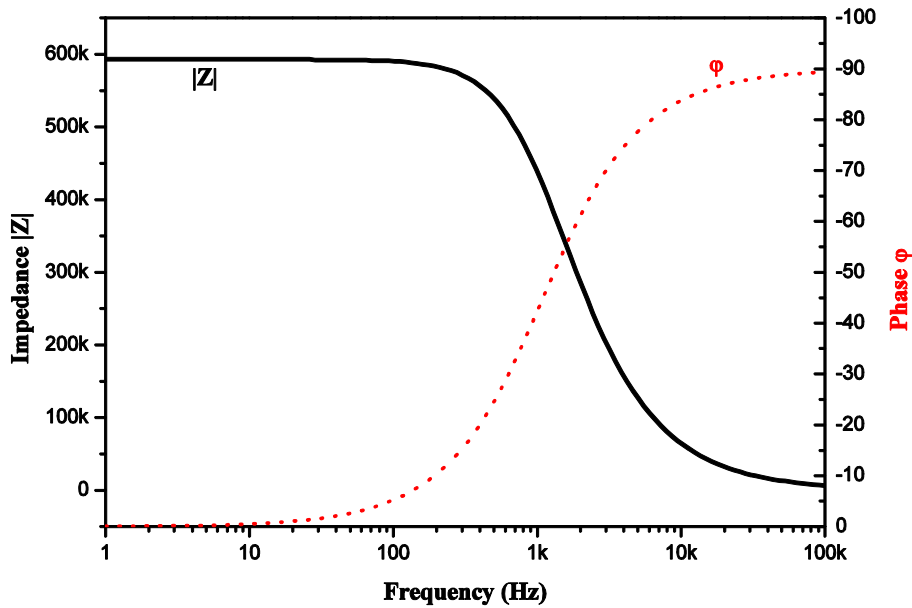
Figure 2-3: Bode plot of a simple RC-circuit.

2.3. Physical Properties of the Vanadium Oxides

In this chapter the structural and electrical properties of vanadium pentoxide are be briefly reviewed.

2.3.1. Structure of the Vanadium Oxides

Vanadium pentoxide (V_2O_5) has a layered orthorhombic structure of the type Pmmn. The lattice parameters are a = 11.512(3) Å, b = 3.564(1) Å and c = 4.368(1) Å [34]. Figure 2-4 depicts the bulk structure of V_2O_5. There are three differently coordinated oxygen atoms: the vanadyl oxygen O^1, O^2 linking chains along the a-axis and O^3 connecting chains in the a-b plain. The layers are connected via weak van der Waals bonds along the c-axis. Due to the

easy change of valence from V^{5+} to V^{4+} and V^{3+} many phases exist in the system V_2O_5-VO_2 and the compounds V_2O_5, V_3O_7, V_4O_9, V_6O_{13}, and VO_2 are known [35].
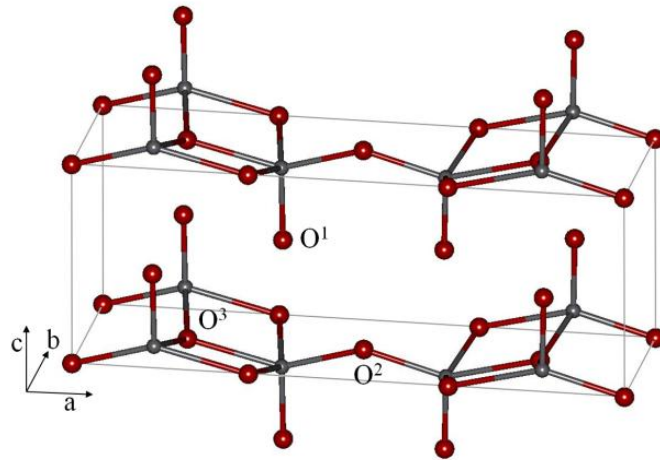
Figure 2-4: **The structure of vanadium pentoxide [34]. Red is oxygen and grey vanadium. The coordination of the oxygen atoms is indicated by the numbers.**

2.3.2. Electrical Properties of Vanadium Pentoxide

The electrical properties of vanadium pentoxide have been extensively investigated, but often in a temperature range where the defect concentration is independent of temperature or partial pressure [35,36,37,38,39,40,41]. Vanadium pentoxide is an n-type semi conductor with low electron mobility and the electronic transport at low temperature occurs via small polarons [36,37,38,42,43]. There are some investigation at higher temperature, but often the surface area of the sample (often a sintered body or single crystal) restricted the equilibration of the partial pressure of oxygen in the sample with the surrounding atmosphere because the surface reaction is usually the rate determining step [44,45]. Some authors found a hysteresis in the conductivity on heating and cooling at higher temperature which was attributed to the presence of lower oxides [46] or interactions with oxygen in the gas phase [47]. Allersma et al. [43] investigated the conductivity of molten vanadium pentoxide, which exhibits faster equilibration kinetics. The authors investigated the dissociation of vanadium pentoxide as a function of partial pressure and determined the enthalpy of formation for an oxygen vacancy to 1.3 eV. They found an apparent activation energy of the vanadium pentoxide melt of 0.63 eV and ascribed it to a combination of dissociation and migration enthalpy. By using the migration enthalpy ΔE_m of a single crystal they were able to calculate the defect formation enthalpy according to following approach:

The oxygen vacancy formation reaction 2-28 exhibits for the conductivity a partial pressure dependency of -1/6 as already discussed on page 11.

$$2V_V^x + O_O^x \xrightarrow{\text{reduction}} 2V_V^{'} + \cup_O^{\bullet\bullet} + 1/2\,O_2 \qquad \text{2-28}$$
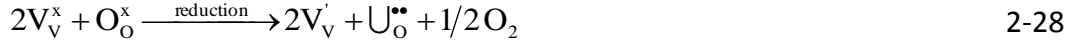
V is vanadium and $V_V^{'}$ is a V^{4+} ion that is formed on reduction. Experiments on the melt confirmed the partial pressure dependency and thus following mass action law for the reduction reaction was used [43]:

$$K = \left[V_V^{'}\right]^2 \cdot \cup_O^{\bullet\bullet} \cdot P_{O_2}^{\frac{1}{2}} \qquad \text{2-29}$$

As $\left[V_V^{'}\right] = 2\left[\cup_O^{\bullet\bullet}\right]$:

$$K = 1/2\left[V_V^{'}\right]^3 \cdot P_{O_2}^{\frac{1}{2}} \qquad \text{2-30}$$

and $\left[V_V^{'}\right] = (2K)^{\frac{1}{3}} \cdot P_{O_2}^{-\frac{1}{6}}$. $\qquad$ 2-31

From $K = K_0 \cdot \exp\left(-\Delta H_f^0 / RT\right)$, where ΔH_f^0 is the enthalpy of formation of the $\cup_O^{\bullet\bullet}$ defect follows with equation (2-31):

$$\left[V_V^{'}\right] = K_1 \cdot \exp\left(-\Delta H_f^0 / 3kT\right) \cdot P_{O_2}^{-\frac{1}{6}} \qquad \text{2-32}$$

The conductivity of vanadium pentoxide depends on the concentration of $\left[V_V^{'}\right]$:

$$\sigma = \left[V_V^{'}\right] \cdot \exp\left(-\Delta E_m / kT\right) \qquad \text{2-33}$$

ΔE_m is the ionization energy for the localized electron at the $\left[V_V^{'}\right]$ site. Substituting $\left[V_V^{'}\right]$ in equation (2-33) with equation (2-32), the conductivity is described by equation (2-34) with a pressure dependence of -1/6:

$$\sigma = K_2 \cdot \exp\left(-\left(\Delta H_f^0 / 3kT + \Delta E_m / kT\right)\right) \cdot P_{O_2}^{-\frac{1}{6}} \qquad \text{2-34}$$

$$\sigma = K_2 \cdot \exp\left(-\Delta E^* / kT\right) \cdot P_{O_2}^{-\frac{1}{6}} \qquad \text{2-35}$$

Therefore at constant P_{O_2} the enthalpy of formation for an oxygen vacancy ΔH_f^0 can be calculated using equation (2-36):

$$\sigma = K_2 \cdot \exp\left(-\Delta E^* / kT\right) \qquad \text{2-36}$$

where ΔE^* is the measured activation energy derived from the conductivity data. As ΔE^* is

$$\Delta E^* = \Delta H_f^0 / 3 + \Delta E_m \qquad \text{2-37}$$

the value of ΔH_f^0 can be derived from the Arrhenius-plot if ΔE_m is known.

2.4. Catalytic Properties of Vanadium Oxide Catalysts

In this chapter the catalytic properties of vanadium pentoxide are reviewed.

2.4.1. The Oxidative Dehydrogenation of Propane

The Oxidative Dehydrogenation of Propane (ODH) is a heterogeneous catalytic reaction and in this kind of reaction alkanes react with oxygen to form water and alkenes:

$$C_3H_8 + 1/2 O_2 \rightarrow C_3H_6 + H_2O \qquad \text{2-38}$$

The reaction enthalpy is $\Delta H^0_{298} = -105\,\mathrm{kJmol^{-1}}$ and is thus thermodynamic favourable and allows high conversion in contrast to the catalytic dehydrogenation:

$$C_3H_8 \rightarrow C_3H_6 + H_2 \qquad \text{2-39}$$

that exhibits an enthalpy of $\Delta H^0_{298} = +136\,\mathrm{kJmol^{-1}}$ and is thus endothermic. However, selectivity problems may arise for the ODH because the products of the total oxidation are more stable than the desired alkenes. [48]
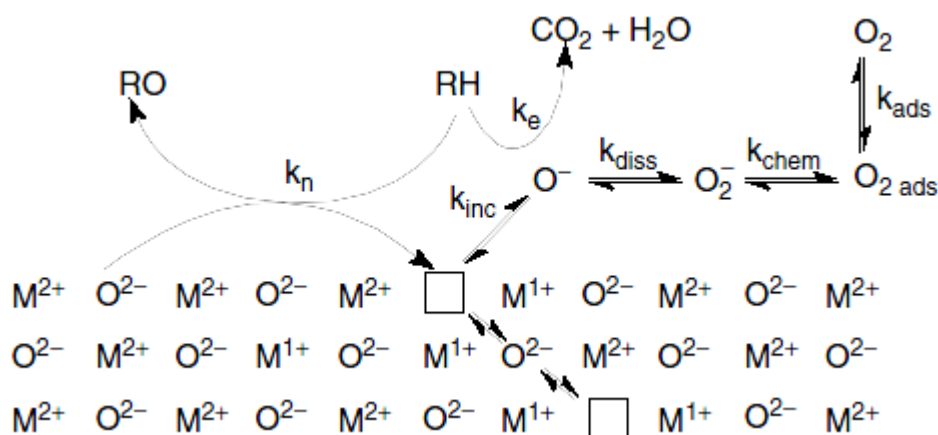
Figure 2-5: Reaction mechanism for the ODH. The squares are oxygen vacancies that can diffuse in the metal oxide lattice. Furthermore, the reaction of the alkane RH to RO or the total oxidation products CO_2 and H_2O is shown. The reduced catalyst is oxidized from the gas phase oxygen that adsorbs at the surface and dissociates before being incorporated into the lattice. [48]

The ODH follows a Mars-van-Krevelen mechanism [6] which is a redox reaction with contribution of lattice oxygen from the catalyst. It is called a redox mechanism because the reduction and oxidation cycle can be described as separate steps. In the reduction cycle the catalyst releases oxygen and oxidizes the alkane. In this step an oxygen vacancy is formed at the surface. This vacancy is refilled in the oxidation cycle but the reoxidation may occur at a

different site that the catalyst was reduced because transport of oxygen through the lattice is assumed (see Figure 2-5).

2.4.2. The Support Effect

Many authors found an influence of the support material on the catalytic performance [2,3,8,4,9,10,11,12] but the role of the support is still a matter of discussion. Often a high reducibility of the support is correlated with a higher activity of the catalyst which is ascribed to the properties of the V-O-support bridging bonds [2,49,50]. Others propose, that the support determines only the structure of the resulting vanadium species (crystallites, polymers and monomers) [11] or that a complex interaction of supporting oxide and vanadia surface species are the origin of the support effect [4]. At low coverage isolated monomeric VO_4 species are found and with increasing loading the extent of polymerization rises [51,52,53,54] forming finally 3 dimensional crystalline vanadium pentoxide. The vanadium species exhibit different reducibility [10,55] and the support influences the speciation and dispersion of the VO_x species and thus the catalytic performance [11,12,56,50]. Several models are proposed for the mono- and polymeric vanadia structures and are displayed in Figure 2-6:
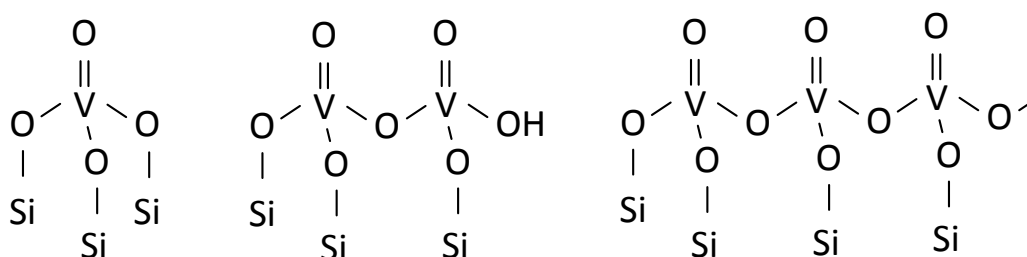
Figure 2-6: Structural models for the supported vanadia species on silica support. Left: monomers, middle and right represent polymeric structures. [57,58,59]

In [60,61,62,63,64] the redox properties of vanadia-based mixed bulk oxides and supported catalysts are investigated using coulometric titration. Redox isotherms are determined and it is shown, that the transition to lower oxidation states proceeds at different oxygen partial pressures. Moreover, for mixed bulk oxides different oxidation enthalpies are found. However, supported catalysts of low loading showed nearly identical properties.

3. Methods

3.1. Catalyst preparation

3.1.1. High Loading

The powder catalysts were obtained by thermal spreading of vanadium pentoxide (GfE Materialien GmbH) over the supporting oxides (Table 3-1). The support and vanadium oxide was mixed in a ball mill (Retch, type PM4, 30 min, 120 Umin^{-1}, 30 Al$_2$O$_3$ balls) in cyclohexane and then subsequently dried at 70 °C for 1 day. The dried powder was calcined in a quartz furnace at 500 °C for 4 hours in a stream of synthetic air (AirLiquide N50, 20 ml/min) passing through the powder bed (Appendix, Figure 7-4). The heating and cooling rate was 3 Kmin^{-1}. Table 3-2 shows the composition of the differently supported catalysts.

Table 3-1: Manufacturer information for the metal oxides used as support and active compound.

Oxide	Manufacturer	Lot.
V$_2$O$_5$	GfE Materialien GmbH	92393
SiO$_2$	Alfa Aesar	K207006
α-Al$_2$O$_3$	Sumitomo	AKP50, HD881
ZrO$_2$	Alfa Aeasar	H29T027
TiO$_2$	Kronos	Gl102/10827
MgO	Magnesia	Magnesia 298, 4309298

Table 3-2: Nomenclature and composition of supported catalysts. W is the mass fraction and x the mole fraction of vanadium pentoxide. Additionally the BET surface area is shown.

Sample	V$_2$O$_5$ (mol%)	V$_2$O$_5$ (m%)	Surface area (m^{2}g^{-1})
V$_2$O$_5$	100	100,0	2,01
VO$_x$/TiO$_2$	30	49,8	4,63
VO$_x$/m-ZrO$_2$	30	38,8	2,38
VO$_x$/SiO$_2$	30	56,5	1,73
VO$_x$/MgO	30	65,9	10,40
VO$_x$/α-Al$_2$O$_3$	30	43,3	9,04

3.1.2. Percolation Catalysts

The percolation catalysts were prepared with the same method as used above. Mixtures of different composition were prepared for m-ZrO_2 und SiO_2 supports (Table 3-3 and Table 3-4).

Table 3-3: **Nomenclature and composition of silica supported percolation samples. W is the mass fraction and x the mole fraction of vanadium pentoxide.**

Name	SiV56	SiV43	SiV35	SiV25	SiV20	SiV14	SiV7	SiV0
w (%)	56.5	43.1	34.8	25.2	19.7	13.7	7.2	0
x (%)	30	20	15	10	7.5	5	2.5	0

Table 3-4: **Nomenclature and composition of zirconia supported percolation samples. W is the mass fraction and x the mole fraction.**

Name	ZrV39	ZrV27	ZrV21	ZrV14	ZrV10	ZrV7	ZrV4	ZrV0
w (%)	38.8	27.0	20.7	14.1	10.7	7.2	3.6	0
x (%)	30	20	15	10	7.5	5	2.5	0

3.1.3. Amorphous Catalysts

The amorphous monolayer catalysts were obtained by a thermal spreading method. The supports (Table 3-5) were calcined at 750 °C for 4 hours in a quartz rotary furnace in a flow of synthetic air (50 ml/min, 20 % O_2/Ar) and then mixed with a precursor (vanadyl acetylacetonate) in an agate mortar. The mixture was again calcined at 500 °C for 4 hours.

Table 3-5: Nomenclature and physical properties of amorphous catalysts.

Name	Support manufacturer	Surface are (m^2g^{-1})	Surface density (V at/nm)	w (%)
VO_x/TiO_2	Saint-Gobain Norpro	17.1	3.5	0.6
VO_x/m-ZrO_2	Saint-Gobain Norpro	52.1	3.1	1.4
VO_x/γ-Al_2O_3	Saint-Gobain Norpro	200.9	3.1	4.9

3.2. Impedance Spectroscopy

For the impedance spectroscopic experiments, the powder catalysts were compacted into discs of 10 mm or 6 mm using an uniaxial press. These discs were isostatically redensified at 2.5 kbar. Then platinum contacts with a diameter of 5 mm were sputter coated (Balzers, SCD 050) on both sides at 44 mA and 240 s.
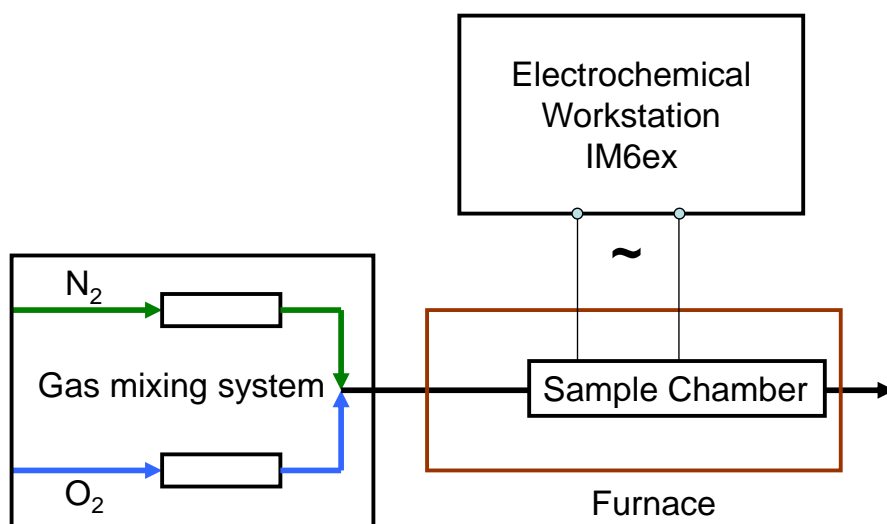
Figure 3-1:   Setup for electrochemical impedance spectroscopy.

The electrochemical measurements were done using a Zahner IM6ex with the software package Thales 3.13. The measurement setup enables experiments in different atmospheres and temperature up to 1100 °C (Figure 3-1).

For the experiments, the sample chamber was equilibrated at a starting temperature of 350 °C for about 5 hours. Then with a heating rate down to 0.1 K/min was used for the temperature dependent experiments on heating and cooling. Due to the low heating rate the experiments take up to 3 days (Figure 3-2).
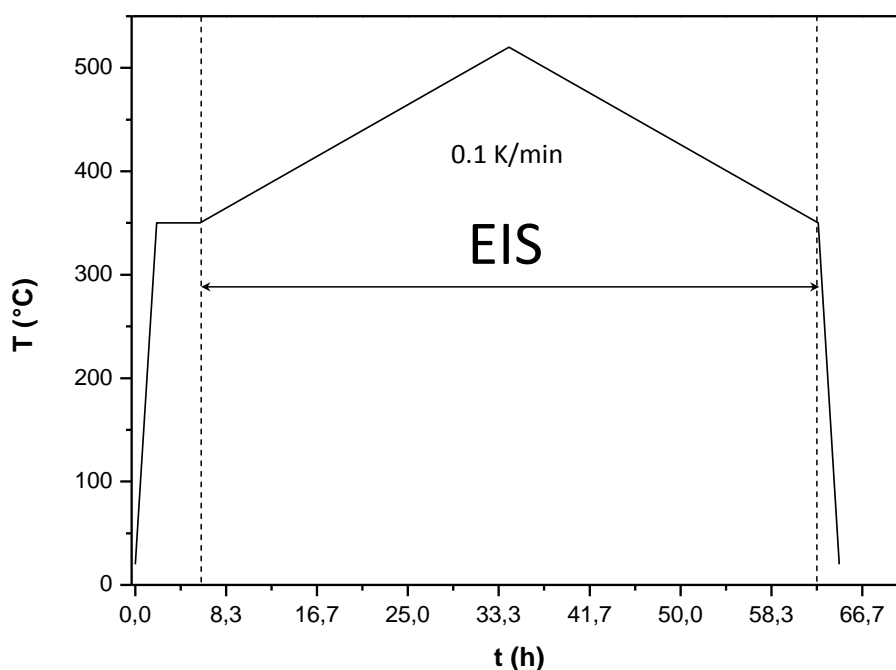

Figure 3-2:   Temperature profile for the conductivity experiments. Due to the low heating rate, one experiment runs up to 3 days.

Usually, an amplitude of 50 mV was applied and the frequency range was adapted to the required measurement range (e.g. 100 mHz to 3 MHz). The modelling of the impedance spectra was done using the Thales software and the conductivity σ was calculated using the equation:

$$\sigma = \frac{d}{A \cdot R}$$
<div align="right">3-1</div>

d is the sample thickness, A the cross section and R the resistance.

3.2.1. Conductivity Relaxation Experiments

The system was equilibrated at a certain oxygen partial pressure and temperature. Then the gas in the sample chamber was exchanged. For this purpose the chamber was evacuated (300 mbar) and rinsed with the new gas composition 3 times. Then the impedance spectra were taken for a certain time. For the evaluation of the data, an exponential dependency of conductivity and time was assumed and the data was fitted with the function:

$$\sigma = \sigma_0 + A \cdot \exp(rt)$$
<div align="right">3-2</div>

σ is the conductivity at time t, σ_0 is the conductivity at t = 0 s, A is the pre-exponential factor and r the rate constant.

3.2.2. Partial pressure Dependent Conductivity

The samples were heated in oxygen to the final temperature and then equilibrated for 5 days. Then the partial pressure was lowered and again equilibrated to 2 – 3 days. Equilibration was verified by observing the change of conductivity as a function of time. Then an impedance spectrum was taken.

Table 3-6: **Gas mixtures for the partial pressure dependent experiments. D is the gas flow in l/min.**

pO_2	N_2 flow (%)	O_2 flow (%)	D (l/min)
0.6	2	3	0.05
0.5	2	2	0.04
0.4	3	2	0.05
0.33	4	2	0.06

3.3. Neutron diffraction

Supported catalysts comprising 10 mol% of vanadium pentoxide were used for the diffraction experiments. As support α- and γ-alumina, titania and zirconia were used and the catalysts were prepared according to chapter 3.1.1.

Neutron diffraction measurements were done at instrument E6 at BENSC/HZB Berlin, Germany. 5 mg of catalyst were applied to the quartz glass crucible (diameter = 10 mm) and the experiments were done in a flow of oxygen (0.05 ml/min, *Linde*, purity 5.0). Measurements were done at following temperatures: 30 °C, 300 – 500 °C in 50 K steps. Each temperature increase was done in a single step and then equilibrated during repeated neutron diffraction. (Wave length 2.439 nm, range $10 \leq 2\Theta \leq 130°$, measuring time 50 min).

Equilibrium was achieved after 20 min (thermo couple) and the according measurement was used for evaluation. The lattice parameters were calculated using the software Full Prof.

3.4. X-ray Diffraction

The XRD experiments at 500 °C at different oxygen partial pressure were done in a D5000 with a Cu-anode (λ = 0.1542 nm) in a range $10 \leq 2\Theta \leq 70°$. A Buehler heating chamber (Pt-resistance heater) and a scintillator detector was used in this setup. The time for a single measurement was 24 hours.

Table 3-7: Program for the partial pressure dependent XRD experiments at 500 °C.

	Atmosphere	T (°C)	Comment
1	Air	10	Reference measurement
2	O_2	500	24 hour equilibration
3	O_2	500	measurement
4	Synt. Air	500	24 hour equilibration
5	Synt. Air.	500	measurement

Slurry of Vanadium pentoxide and alcohol was applied on the heating band and dried at room temperature. After the alcohol was evaporated, the sample chamber was heated at 1 K/min in a flow of oxygen to 500 °C. Then, after 24 hours for equilibration, the first

measurement was done and after that the partial pressure was changed and again after 24 hours the second measurement was done (see Table 3-7). The lattice parameters were calculated using the software Full Prof.

XRD phase analysis was done using a Philips PW 1070 with a Cu-anode ($\lambda = 0.1542$ nm) and monochromator in a range $10 \le 2\Theta \le 90°$ and was analyzed using the software package DiffracPlus.

3.5. UV-vis Spectroscopy

UV-Vis spectroscopy was done with a Perkin Elmer Lambda 900 UV/VIS/NIR-Spectrometer in reflection geometry on pressed powder pellets. The measurements were calibrated using $BaSO_4$ and performed in a range of 300 to 900 nm with a resolution of 1 nm. The spectra were transformed into the Kubelka-Munk function $\left(F(R_\infty)\right)$ with the OPUS software (Bruker). The optical band gap (E_g) was determined from the intersect of a linear function of $\left(F(R_\infty) \times h\nu\right)^{0.5}$ against $h\nu$ with the x-axis.

In order to investigate thermally induced defect formation the band gap of temperature pretreated samples was determined. For this purpose powder pellets were tempered for 8 days at different temperatures in air. They were taken from the hot furnace and stored in nitrogen atmosphere. The measurements were done in ambient air at room temperature.

3.6. Rutherford backscattering

In order to investigate the non-stoichiometry in the system V_2O_x, RBS (Rutherford Backscattering) was used. For these experiments, protons with a primary energy of E0 = 300 keV were used. In the setup the ion beam passed an aperture and a beam monitor and then irradiated the sample with an area of 1 mm in diameter. The proton yields are all related to an incident ion charge of 10 µC and the analysis of backscatter ions is done by an electrostatic cylinder capacitor analyser (ESA). The acceptance solid angle was equal to 7.5*10-4 sr, the energy resolution $\Delta E_{res}/E = c1 = 7.3*10^{-3}$. For the detection of protons a CsJ:Tl scintillator and a photo multiplier was used. The experiments were done at normal incidence and the scattering angle φ_2 corresponds to the angle between incident beam and outgoing beam and was 45° for these experiments.

Figure 3-3 depicts the energy spectra of backscattered protons for vanadium pentoxide single crystals, polycrystals, vanadium trioxide polycrystals and a sample of unknown oxygen content V_2O_x.
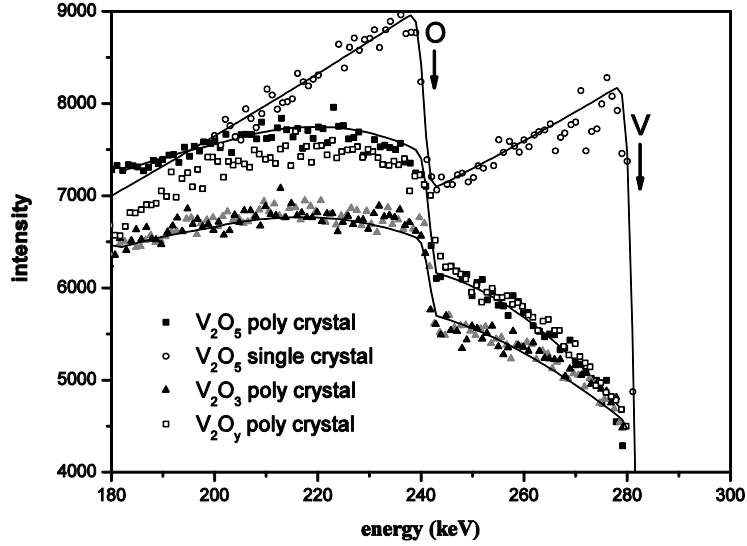

Figure 3-3: RBS spectra of V2O5 poly and single crystals

Specific threshold energies are found at 280 keV and 242 keV due to scattering at vanadium and oxygen atoms, respectively. Evaluation of the ratio of proton yield for oxygen and vanadium allows calculation of the oxygen concentration. The measured spectrum for the single crystal agrees with the simulation of a function with x = 5.

Taking into account the roughness of the sample surface [65], the RBS energy spectra were simulated for polycrystals. In order to verify the RBS method to determine the oxygen concentration, a V_2O_5 was reduced by CO to V_2O_3 at a 500 °C. The atom concentrations N_O/N_V are determined by the ratio of the proton yield at 240 keV and 280 keV for oxygen and vanadium, respectively. Taking the intensities of V_2O_5 as a reference for V_2O_x then it follows:

$$x = 5 * \frac{I_O(V_2O_x)}{I_O(V_2O_5)} \frac{I_V(V_2O_5)}{I_V(V_2O_x)}$$
3-3

This gives for polycrystalline V_2O_3 a good agreement with x = 3.1 ± 0.2.

3.7. TG-FTIR

The thermogravimetric experiments were done in a reducing gas atmosphere (CRYSTAL gas mixture, Air Liquide) consisting of O_2/Propane/N_2 (2.18 % / 7.97 % / 89.85 %) using a Netzsch STA409PC/PG and a Bruker Equinox IFS55 FTIR setup. Alumina crucibles were used and a gas flow of 80 ml/min was chosen.

3.8. Scanning Electron Microscopy

The EDX mappings and micrographs were done at the Hahn-Meitner-Institut (Berlin Wannsee) using a Zeiss FIB 1540 EsB Cross Beam and the specimens were evaporated with carbon.

3.9. Transmission Electron Microscopy

Transmission electron microscopy (TEM) investigation were done in a Zeiss LIBRA 200 FE operated at 200 kV accelerating voltage. Bright field micrographs were recorded while using the in-column energy filter to obtain zero energy loss filtered images. Samples for the TEM experiments were obtained by crushing the material and dispersing it onto copper grids covered with carbon film.

3.10. Catalytic Testing

Catalysts at High Loading

The powder was compacted at 30 MPa and then granulated and sieved to the fraction 100 – 200 µm.

The catalytic measurements were performed at ambient pressure in U-shaped fixed bed quartz reactors (Ø6 mm). The catalyst particles were diluted with inert silicon carbide in the mass ratio 1:2 (catalyst/SiC). The feed had a composition of C_3H_8/O_2/N_2 = 2/1/4. The experiments were performed in the temperature range from 350 to 500 °C under differential reaction conditions. The feed and the product components were analyzed by an on-line gas chromatograph.

Due to the high loading of the catalysts excess vanadium pentoxide not in contact with the support is present and thus it was not possible to calculate the loading of the surface. Hence,

the apparent propane activation energy $E_{a,app}$ was determined from the temperature dependent propane conversion X using the function:

$$X = X_0 \cdot \exp\left(- E_{a,app}/RT\right)$$

3-4

Amorphous Monolayer Catalysts

Catalytic testing was done in a stainless steel fixed bed reactor with a diameter of 8 mm. The inside of the tube is catalytic inactive due to a SilcoTek^{TM} silicon coating. The kinetic experiments were done under differential conditions using a standard stoichiometric feed composition of 6 kPa oxygen and 12 kPa ethanol with a total flow rate of 220 Nml/min. The temperature was varied in a range of 140 to 200 °C. The products were analyzed by a Shimadzu GC-2014 equipped with a methanizer, TCD, FID, and packed HayeSep Q and Molsieve 13X columns.

The apparent propane activation energy $E_{a,app}$ was determined from the temperature dependent ODP rate r at differential reaction conditions (conversion X < 10%) using the function:

$$r = \frac{\dot{n} \cdot X \cdot M}{m \cdot w}$$

3-5

$\dot{n}$ is the flux of propane, X the conversion, M the molar mass of vanadium, m the mass of the catalyst and w is the mass fraction of vanadium in the catalyst.

i

4. Results and Discussion

First the transport properties of vanadium pentoxide based catalysts are investigated and discussed in Chapter 4.1. Then, in Chapter 4.2 micro-structural influences on the conductivity are shown and finally in Chapter 4.3 the impact of transport properties on the catalytic reaction is discussed.

4.1. Transport Properties

4.1.1. The Method – Pure Vanadium Pentoxide

In this Chapter the transport properties of pure vanadium pentoxide are characterized and a method is developed that allows the experimental determination of the oxygen defect formation enthalpy.

4.1.1.1. Impedance Spectroscopic Investigations

The samples for conductivity measurements consist of pressed powder pellets. These exhibit a strong orientation along the c-axis due to the anisotropic lattice of vanadium pentoxide. A less pronounced orientation is present in the direction of the a-axis. These results - determined by XRD – are shown in Figure 4-1.
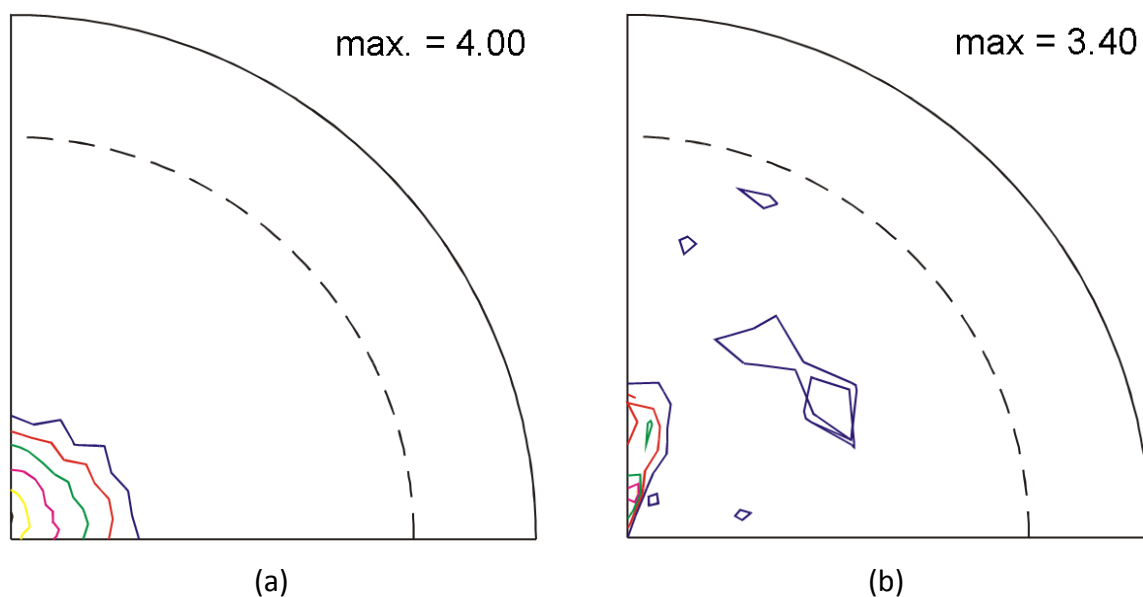

Figure 4-1:   **Experimental pole figure of compressed V2O5 pellet, (a) (001)-reflex, (b) (200)-reflex**

As the electrical properties are anisotropic [36,37,38,39,66], the measurements are governed by the properties parallel to the c-axis.

A typical plot of the impedance spectroscopic measurements is shown in Figure 4-2. This plot can be approximated by a single semi circle, and hence the electrical behavior of the investigated sample is described by a parallel RC-circuit.
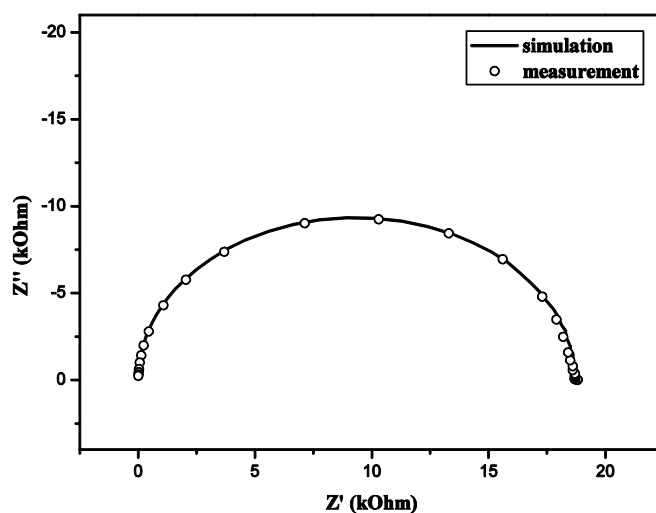

Figure 4-2: **Nyquist plot of V2O5 at room temperature.**

Charge carriers – polarization experiments and conduction path

For the determination of the contributing charge carriers, polarization experiments in the temperature range of 300 to 500 °C were carried out in synthetic air. As no polarization was detected, the charge transfer was concluded to be of electronic nature. In order to distinguish between bulk, grain boundary and electrode effects, the sample thickness and grain size was varied. Because no change of the capacitive element with sample thickness was observed and electrode effects were excluded the variation of grain size (see Figure 4-3) due to sintering had no effect on the capacitive element in the RC-circuit. Therefore, grain boundary conduction was also excluded. Hence the derived values can be attributed to bulk properties. Further indication results from the value of the capacitive element with C ≈ 250 pF which is in the order of magnitude of a bulk mechanism [67].
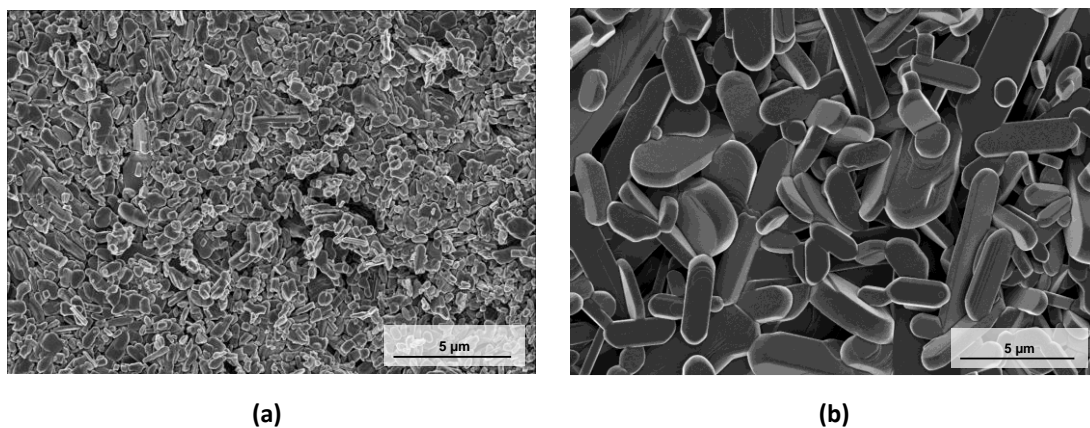
(a)   (b)

Figure 4-3: **SEM micrograph of compressed V_2O_5. 5k magnification. (a) original material and (b) annealed in air for 7 days 610 °C. The grain size is 0.13 and 8.8 µm, respectively.**

Conductivity and Redox State

In this chapter a connection between conductivity and the redox state of vanadium pentoxide is shown with special focus on formation of oxygen vacancies.
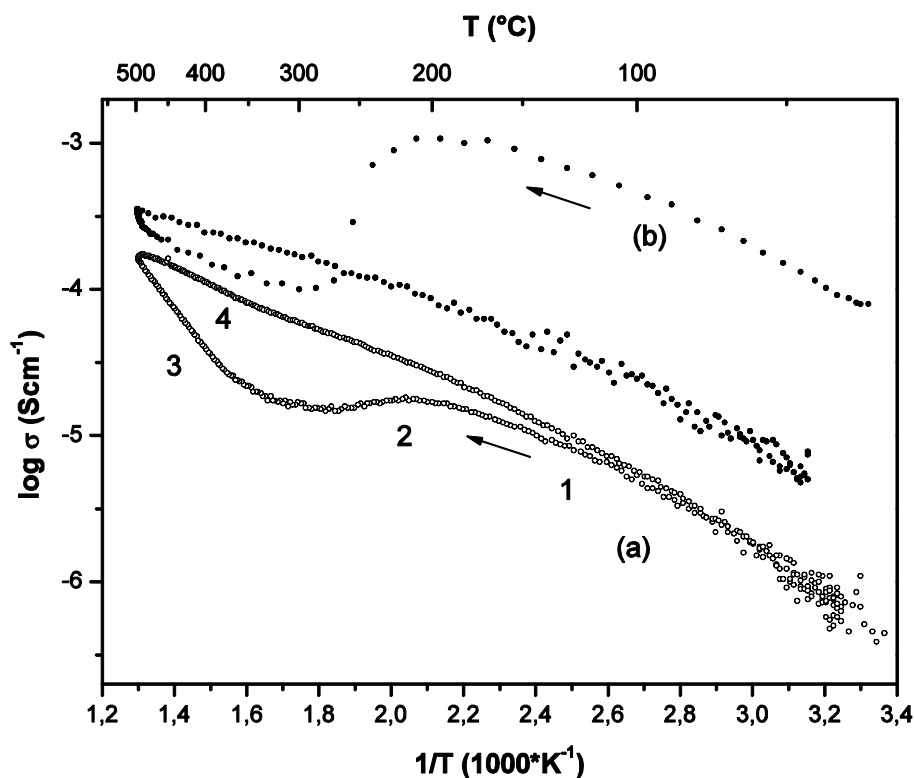

Figure 4-4: Arrhenius plot of V_2O_5 of different samples. Measurements were performed under synthetic air. (a) Untreated sample. (b) Annealed in air at 610 °C and quenched to room temperature.

In Figure 4-4 Arrhenius plots of conductivity σ vs. temperature T are shown. The heating direction of the temperature profile is given by an arrow. During heating of the untreated sample, in Figure 4-4 curve (a), two linear domains can be observed (no. 1 and no. 3). One at low temperature ending above 100 °C and one at higher temperature starting at about 380 °C. During cooling a different behaviour is observed (no. 4). At 209 °C a drop in conductivity is present (no. 2) which is more distinct, when a thermally reduced sample is used (curve (b)).

Figure 4-5 shows 3 Arrhenius plots of vanadium pentoxide samples heated at different rates. Heating at 3 Kmin^{-1} results into a non-linear conductivity increase above 380 °C. And a heating rate of 0.5 or 0.2 Kmin^{-1} gives a linear conductivity dependency.
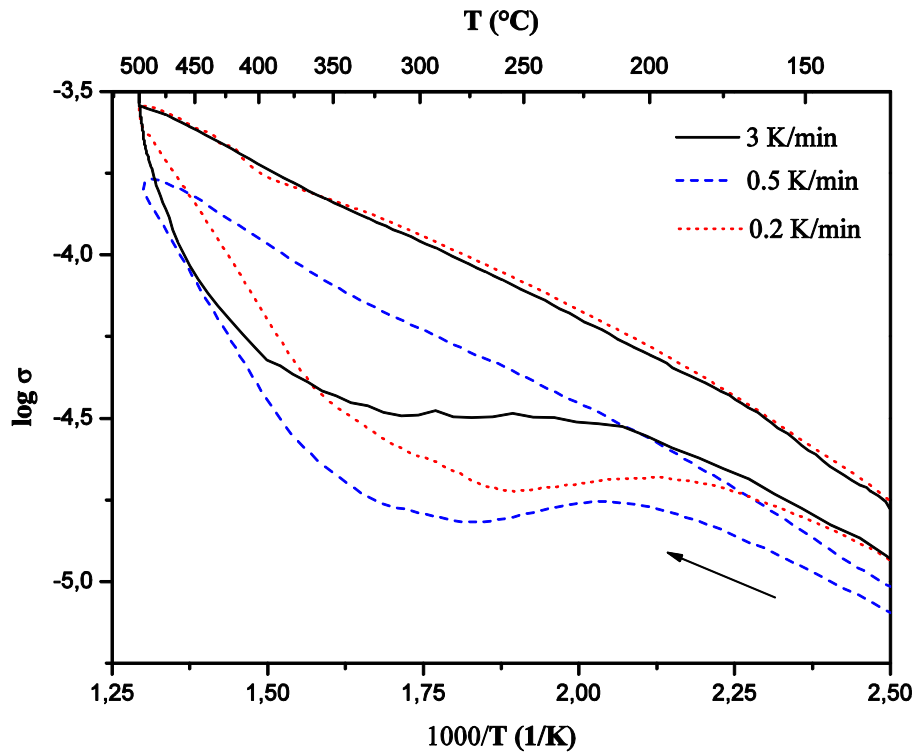
Figure 4-5: Arrhenius plot of conductivity for different heating rates. At 3 Kmin^{-1} a non-linear temperature dependency is observed. At 0.5 and 0.2 Kmin^{-1} a linear change with temperature is observed above 380 °C.

Figure 4-6 displays 4 cycles of the same specimen at 3 Kmin^{-1} are depicted. In the first cycle using a pristine sample, a large hysteresis is observed. In the subsequent cycle (2) the conductivity on heating and cooling follows the cooling curve of cycle 1. After the 2nd cycle the sample was annealed for 7 days in air at 200 °C. A 3rd cycle was run and the hysteresis behaviour reappears. The 4th cycle, directly after run 3, shows again like cycle 2 heating and cooling on the same curve.
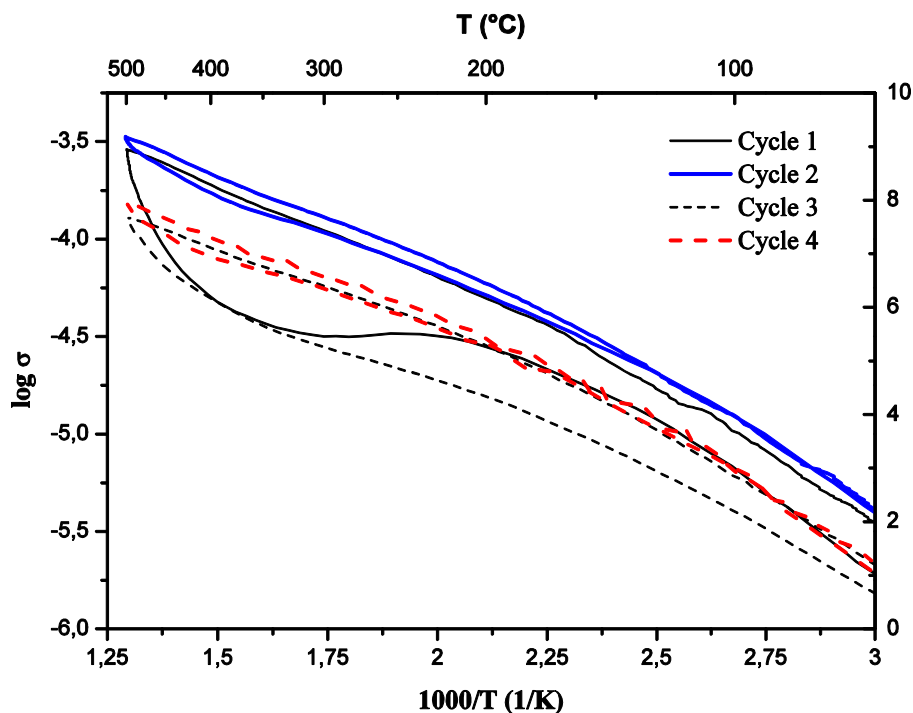
Figure 4-6: 4 cycles of the same vanadium pentoxide sample in synthetic air. A fast heating rate of 3 Kmin^{-1} was chosen. Therefore the conductivity increase above 380 °C is non-linear. 1st cycle: pristine sample shows hysteresis. 2nd cycle: heating and cooling follow the same line. 3rd cycle: after annealing the sample at 200 °C in air the hysteresis behavior reappears. 4th cycle: again heating and cooling is equal to the cooling conductivity of the 3rd cycle.

The variation of heating rate (Figure 4-5) shows that a heating rate of 0.5 Kmin^{-1} is sufficient to attain equilibrium. The results of the cycling experiment in Figure 4-6 display the reversibility of the process but shows that the time on cooling is not sufficient. Prolonged heating at 200 °C is necessary. The features in the Arrhenius plots can be correlated to redox processes. When reaching the Tammann-temperature of 209 °C [68] (no. 2), surface species are activated and reduced sites are reoxidized. Therefore donor centers are eliminated and the conductivity drops to lower values with rising temperature. This effect is more distinct in the thermally reduced sample in Figure 4-4 (b) as it exhibits more point defects. The freezing of defects up to a certain temperature is known and is responsible for the semi-conductive properties at lower temperatures for several oxides [69] (no. 1). Then, starting at 380 °C (no. 3) the conductivity exhibits an activation energy of 0.66±0,04 eV which is in good agreement with the value of 0.63 eV found by Allersma et al. for liquid vanadium pentoxide in air [43], where vanadyl oxygen is released with formation of an oxygen vacancy $U_O^{\bullet\bullet}$ left with two electrons. Again, this is supported by the Tammann rule, that predicts at 2/3T$_m$ (369 °C) an

avalanche of point defects leading to a breakdown of the structure, as discussed by Merkle [70]. The defect reaction for oxygen vacancy formation and electron generation is:

$$O_O^x \xrightarrow{\text{reduction}} U_O^{\bullet\bullet} + 2e^{'} + 1/2\,O_2 \qquad \text{4-1}$$

These electrons are then localized at two adjacent V^{5+} centers, creating two V^{4+} centers [71,72]. The V^{4+}-ions act as donor centers where the electrons can be thermally activated. The electrical conductivity of V_2O_5 is assumed to be due to hopping of localized electrons from V^{4+} to V^{5+} [37,40,43]:

$$V^{4+} - O - V^{5+} \xrightarrow{\Delta E} V^{5+} - O - V^{4+} \qquad \text{4-2}$$

With the conductivity for V_2O_5 as an n-type semiconductor given by

$$\sigma = C \cdot [V_V^{'}] \exp(-\Delta E/kT) \qquad \text{4-3}$$

the conductivity is directly related to the amount of reduction (see equation 4-1). $[V_V^{'}]$ is the concentration of V^{4+}, ΔE the activation energy, k the Boltzmann factor and T the temperature. During cooling a different activation energy is found (no. 4) in the same temperature region (500 – 380 °C) with a value of 0.23±0.01 eV. As it is very similar to the values found for the conduction in poly- and single-crystals (0.23 eV, 0.19 – 0.21 eV) [38,43] it is concluded that during cooling no further reduction or reoxidation occurs. This is also in agreement with calculations done on the stability of the reduced sites in [73].

For comparison, experiments under reducing conditions were performed: Conductivity experiments under vacuum ($2*10^{-4}$ bar) led to the formation of lower oxides (V_6O_{13} and VO_2).
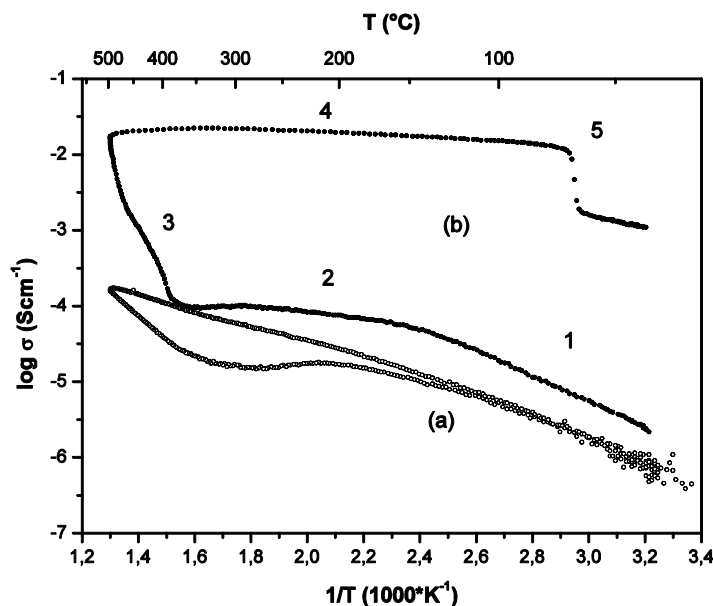
Figure 4-7: Arrhenius plot of vanadium pentoxide in synthetic air (a) and vacuum (b).

Starting at about 380 °C ((no. 3) in Figure 4-7, graph (b)) a strong reduction with phase transformation takes place, so that no activation energy can be determined. As many charge carriers by formation of oxygen vacancies are generated, the conductivity raises up to 2 orders of magnitude. During cooling a less pronounced temperature dependency of the conductivity is observed. At about 67 °C (no. 5) the characteristic metal to semiconductor transition of VO_2 can be identified [74]. The reduction of V_2O_5 proceeds via $V_2O_5 \rightarrow V_4O_9 \rightarrow V_6O_{13} \rightarrow VO_2 \rightarrow V_2O_3$ [72,45] and because XRD phase analysis revealed the presence of small amounts of V_2O_5 and V_6O_{13} the reduction was not complete (Figure 4-8).
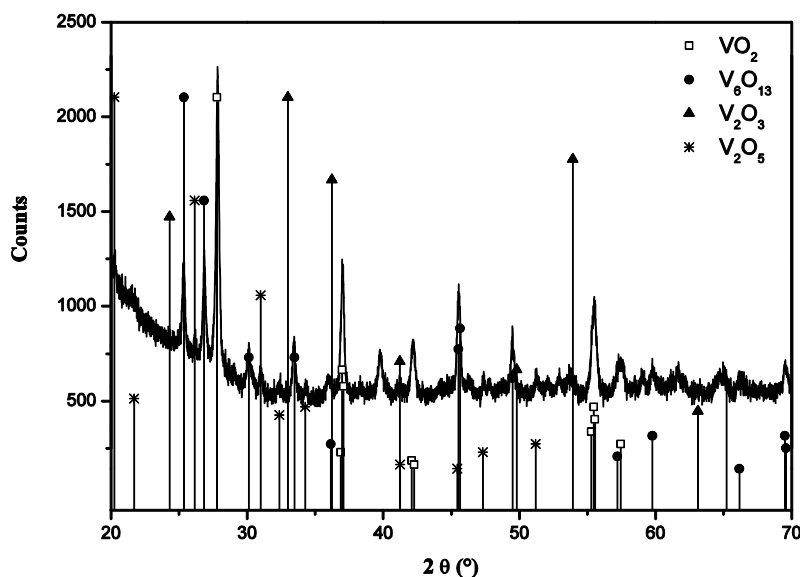
Figure 4-8: **XRD phase analysis of vacuum reduced sample.**

4.1.1.2. Evolution of Defects (UV-vis and RBS)

UV-vis Spectroscopic Experiments

In Figure 4-9 UV-Vis spectra of untreated and annealed (T = 500 and 610 °C) samples are displayed. The band gaps are 2.27 eV and 2.23 eV, respectively, which is in good agreement with literature values in [43,75,76,77,78]. In Figure 4-10 the pretreatment temperature dependent change of the band gap with respect to untreated vanadium pentoxide is displayed. With rising temperature the energy shifts to higher values with a maximum of 2.27 eV at 200 °C. Above 400 °C the gap shifts to lower energies.
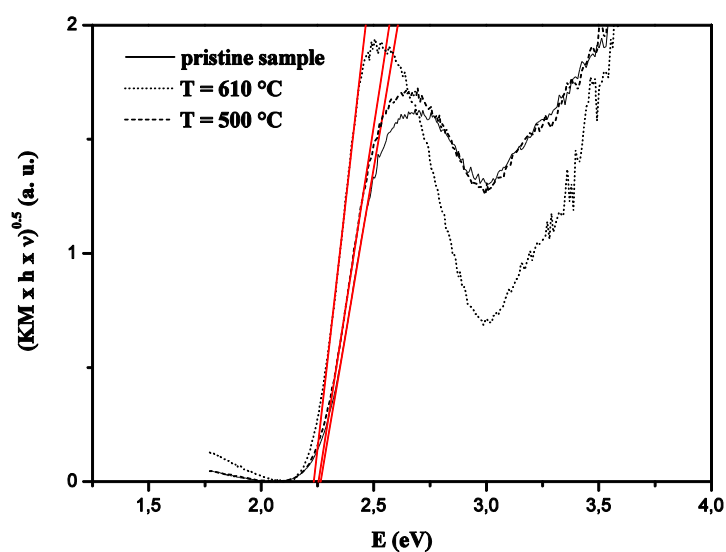
Figure 4-9: UV-Vis spectroscopic experiments on thermally treated vanadium pentoxide in air. Analysis of band gap according to Tauc's law.

The shift of the band gap is an evidence for a redox process as donor states are generated or eliminated in the forbidden zone by the formation or filling of oxygen vacancies as seen in reaction 4-1 [45,78,79]. Therefore in Figure 4-10 oxidation below 400 °C is observed and reduction above that temperature. The temperature dependency of the redox process correlates with the conductivity experiments.
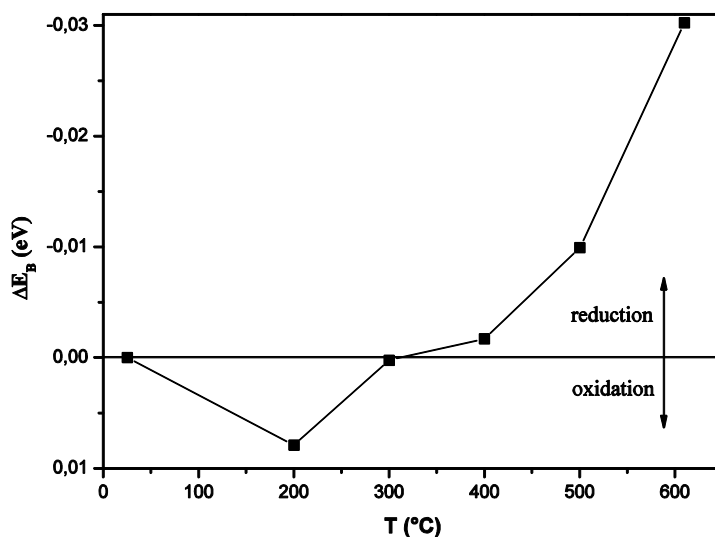

Figure 4-10: UV-Vis spectroscopic experiments on thermally treated vanadium pentoxide in air. Difference of band gap in respect to pristine sample is shown.

Rutherford Backscattering Experiments

The conductivity experiments indicate close to 200 °C fully oxidized vanadium pentoxide (V^{5+}, x = 5) and for temperature above 400 °C an oxidation state of V^{4+} (x = 4). In order to confirm those hypotheses RBS was used to determine the oxygen content x.

Figure 4-11 depicts the RBS energy spectra and the open squares correspond to the pristine vanadium pentoxide, the full squares to an annealed sample (200 °C) and the stars correspond to 2 different samples heat treated for 1 week at 500 °C in air. The fit parameters for the different spectra are shown in Table 4-1.

Table 4-1:   **Parameter for the fitted RBS-spectra. σ_{rough} is the surface roughness and x the oxygen content.**

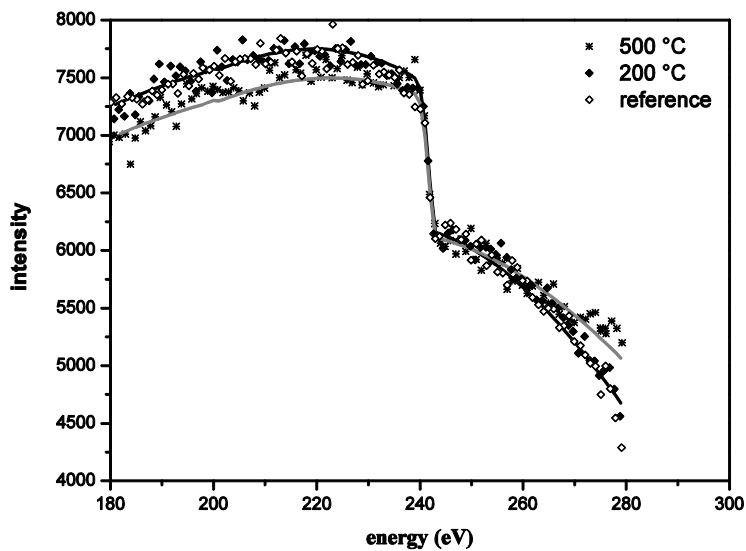| Sample	σ_{rough} [µm]	x
Annealed at 200 °C	0.3	5
Annealed at 500 °C	0.3	4.2 ± 0.2

Figure 4-11:   RBS spectra of V$_2$O$_5$ pre-treated at different temperature. A reduced oxygen concentration is visible in the 500 °C sample.

The samples annealed at 200 °C and the pristine sample are fully oxidized. These were calculated using an average grain diameter of σ_{rough} = 0.3 µm which is confirmed by SEM micrographs which are shown in Figure 4-12.

Annealing at 500 °C results into a lowered oxygen content x < 5 and the oxygen concentration can be calculated using equation 3-3. Analysis of the intensities at 280 keV and 240 keV gives x ≈ 4.1. From the simulation of the whole energy spectrum as described in [65], follows x = 4.2 ± 0.2. The value x = 4.2 is between x = 4.33 (V_6O_{13}) and x =4 (VO_2). Hence, for temperatures T > 400°C a reduction is observed from V_2O_5 to VO_2, with the reduction to VO_2 being not complete.

(a)　　　　　　　　　　　　　**(b)**
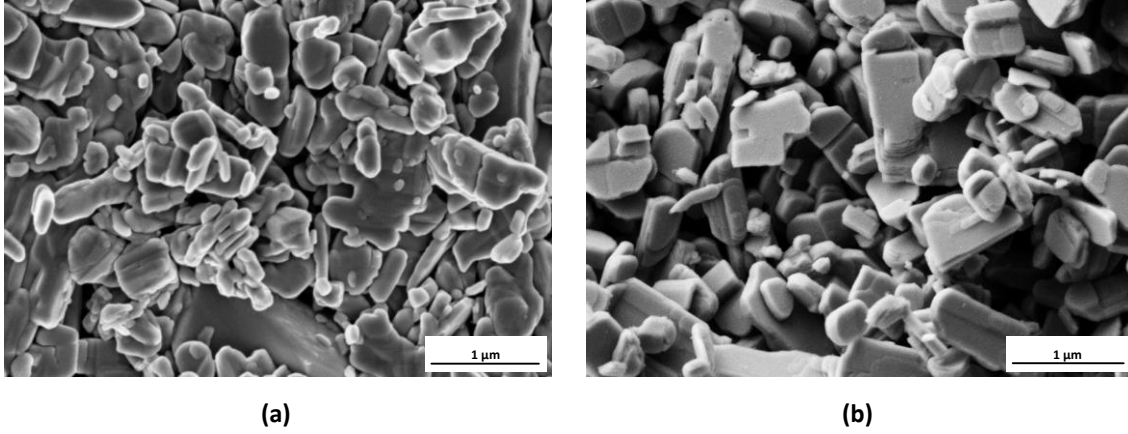
Figure 4-12:　SEM images of V_2O_5 (a) treated at 200 °C and (b) treated at 500 °C for 7 days in air.

4.1.1.3.　Defect Equilibrium and Defect Formation Enthalpy

We have studied the defect equilibrium with oxygen partial pressure via conductivity measurements. As it was determined by [71,72], the electrons after formation of an oxygen vacancy $\bigcup_O^{\bullet\bullet}$ are localized at two adjacent $V^{5+}(V_V^x)$ centers forming two $V^{4+}(V_V^{'})$:

$$2V_V^x + O_O^x \xrightarrow{\text{reduction}} 2V_V^{'} + \bigcup_O^{\bullet\bullet} + 1/2\,O_2 \qquad\qquad 4\text{-}4$$
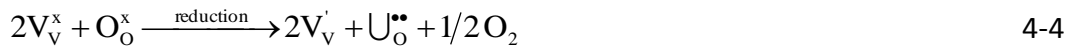
This is in agreement with DFT calculations done from [80], where the localization of electrons leads to the formation of a new covalent bond between two a-b layers accompanied by a relaxation of the lattice in c-direction [13]:

Figure 4-13:   Relaxation of the vanadium pentoxide lattice on reduction [13].

A mass action law for this case was given by [43] resulting into an oxygen partial pressure dependence of the conductivity of -1/6. The mass balance for the reduction reaction (4-4) is [43]:
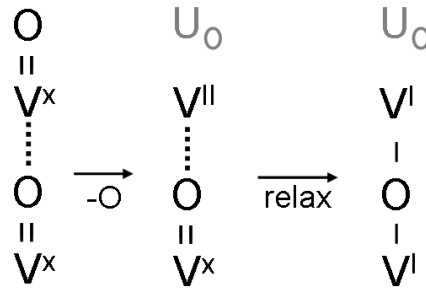
$$K = \left[V_V^{'}\right]^2 \cdot U_O^{\bullet\bullet} \cdot P_{O_2}^{1/2}$$
<div align="right">4-5</div>

Using van't Hoff's law (as discussed on page 16) it is possible to derive following connection of the measured apparent activation energy ΔE^*, the defect formation enthalpy ΔH_f^0 and the migration enthalpy ΔE_m:

$$\Delta E^* = \Delta H_f^0 / 3 + \Delta E_m$$
<div align="right">4-6</div>

The value of ΔH_f^0 can be derived from the Arrhenius-plot if the migration enthalpy is known.

The conductivity of a V_2O_5 sample was measured in an oxygen partial pressure range of $p(O_2) = 1.00 - 0.22$ bar at 508 °C starting with high oxygen pressure and lowering it subsequently. A re-equilibration after each pressure step was achieved in 1 to 2 days. Figure 4-14 displays the data of the conductivity measurements exhibiting a slope of -0.170 ± 0.003.
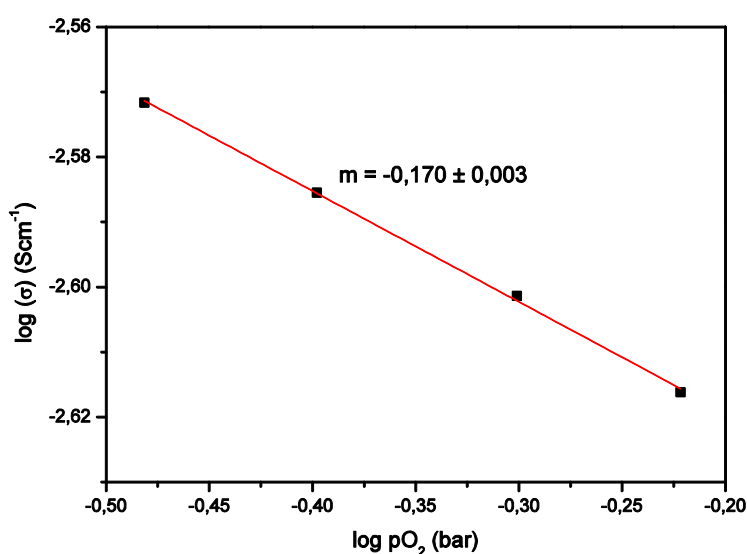
Figure 4-14: Oxygen partial pressure dependency of V_2O_5 at 510 °C. The slope of -1/6 supports defect equilibrium describe in equation 4-4.

Therefore the mechanism in equation 4-4 is valid for our samples. Further evidence for this model gave x-ray diffraction experiments at 500 °C. Lattice parameters were determined for different oxygen partial pressures and are summarized in Table 4-2.

Table 4-2: Lattice parameters determined by high temperature XRD of V_2O_{5-x} at 500 °C in oxygen and synthetic air.

$p(O_2)$ [bar]	lattice parameter [Å]			χ^2
	a	b	c	
1.00	11.5439 ± 0.0003	3.5620 ± 0.0001	4.5017 ± 0.0002	1.88
0.21	11.5447 ± 0.0004	3.5624 ± 0.0001	4.4983 ± 0.0002	2.83
extension	7.2E-05	1.2E-04	-7.5E-04	

When lowering the oxygen partial pressure from 1.00 to 0.21 bar the lattice contracts along the c-axis and extends in a- and b-direction. This is in agreement with lattice relaxation on reduction of the vandyl oxygen site as derived from DFT calculations done by Ganduglia-Pirovano and Sauer [80].
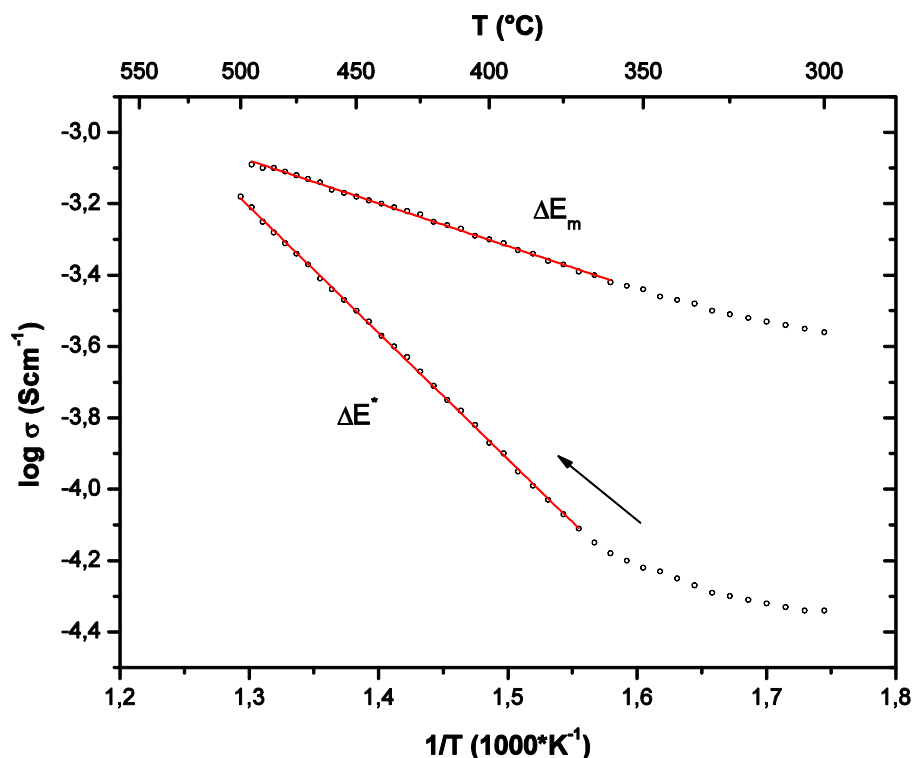
Figure 4-15: Arrhenius plot of vanadium pentoxide in oxygen with a heating rate of 0.5 Kmin^{-1}. ΔE* is the apparent activation enthalpy on heating and ΔE$_m$ is the migration enthalpy on cooling. The arrow indicates the direction of heating.

As the defect equilibrium is known, the enthalpy of formation for an oxygen vacancy can be calculated using equation 4-6. ΔE^* was derived from an Arrhenius-plot, like depicted in Figure 4-15, using the linear slope starting at about 400 °C. For this purpose the average of 6 measurements was taken giving a value of $\Delta E^* = 0.66 \pm 0.04$ eV which comprises activation of electrons and formation of oxygen vacancies. The mobility term ΔE_m can be determined from the slope during cooling, resulting in a value of $\Delta E_m = 0.23 \pm 0.01$ eV. This can be attributed to the ionization of localized electrons, as the re-equilibration reaction during cooling proceeds very slowly and can be neglected. Using relation 4-6 a value of $\Delta H_f^0 = 1.3 \pm 0.1 eV$ was calculated, which is in good agreement with results from experiments on molten V_2O_5 (1.3 eV) [43] and quantum-chemical calculations 1.17 eV [13].

4.1.2. Transport Properties of Supported Catalysts at High Loading

Pure V_2O_5 is used as a catalyst for several reactions [2]. But often supporting metal oxides are applied in order to improve the properties of the catalyst. These enhance the stability of the oxide by inhibiting sintering of the VO_x particles [81], increase the performance, and may further more alter the metal oxide bond strength [82,83] (change of defect formation

enthalpy at interface BaO/MgO and V_2O_5/TiO_2) and thus the reactivity of the catalyst. It is the goal of this chapter to investigate the defect formation in supported VO_x-catalysts of high loading. These are easier to investigate due to higher conductivity of V_2O_5 but not applied as catalyst, because they are unselective due to large amounts of bulk vanadium pentoxide not in contact to the support. The interpretation of the results is based on the assumption that these catalysts exhibit the same behaviour as pure V_2O_5. On the next pages the Arrhenius plots for the conductivity experiments of the different catalysts are depicted together with results from catalytic tests. The propane activation energies E_a are calculated using an Arrhenius approach (equation (3-4)) for the temperature dependent propane conversion X(propane). Furthermore the XRD patterns of aged catalysts (500 °C for 5 days in air) are given for phase analysis. In Table 4-3 the results of the conductivity experiments and catalytic tests are summarized on page 50.

4.1.2.1.   Hysteresis Characteristics

In this chapter the hysteresis characteristics are shown and the defect formation enthalpies are calculated. The results are summarized in Table 4-3 on page 50.

α-Alumina Supported Vanadium Oxide Catalyst

Figure 4-16 shows the conductivity results for the VO_x/α-Al_2O_3 catalyst.
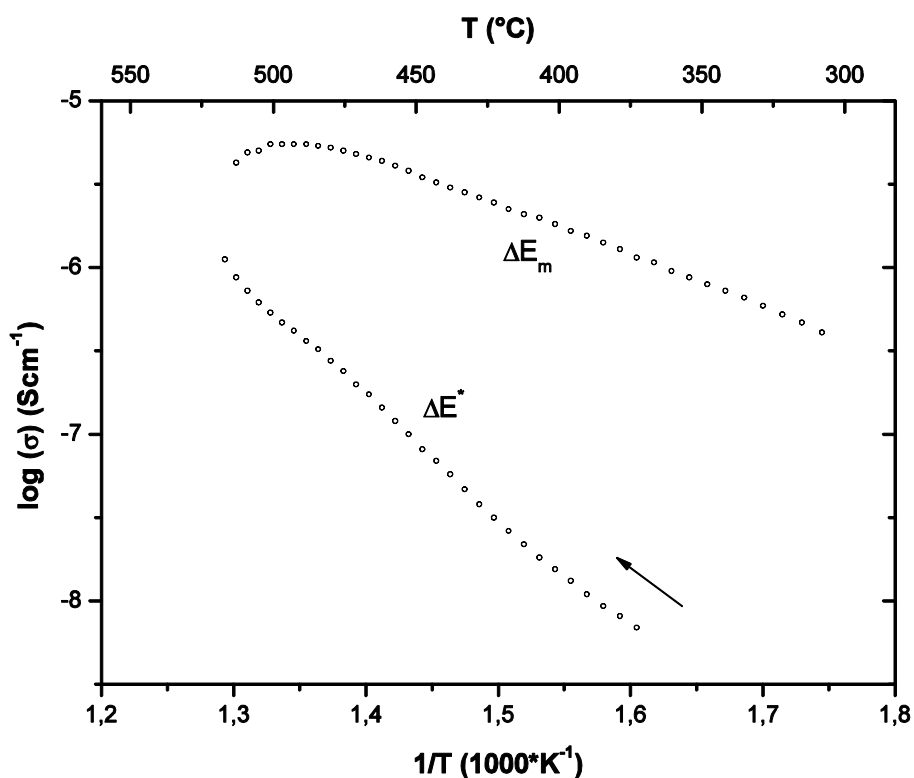
Figure 4-16:   **VO_x/α-Al2O3. Arrhenius plot of conductivity in oxygen (heating rate 0.5 K/min) with the corresponding propane conversion. The arrow shows the direction of heating.**

In the Arrhenius plot a large hysteresis of the conductivity on heating and cooling is visible. The thermal activated region starts at 400 °C and prevails up to 500 °C. On heating an apparent activation energy of $\Delta E^* = 1.4 \pm 0.1$ eV is measured. On cooling the migration energy is $\Delta E_m = 0.5 \pm 0.1$ eV. Using equation (4-6) a defect formation enthalpy of $\Delta H_f = 2.8 \pm 0.1$ eV is calculated. The x-ray diffractogram in Figure 4-17 shows the phases α-Al_2O_3 and V_2O_5 after prolonged heat treatment at 500 °C in air.
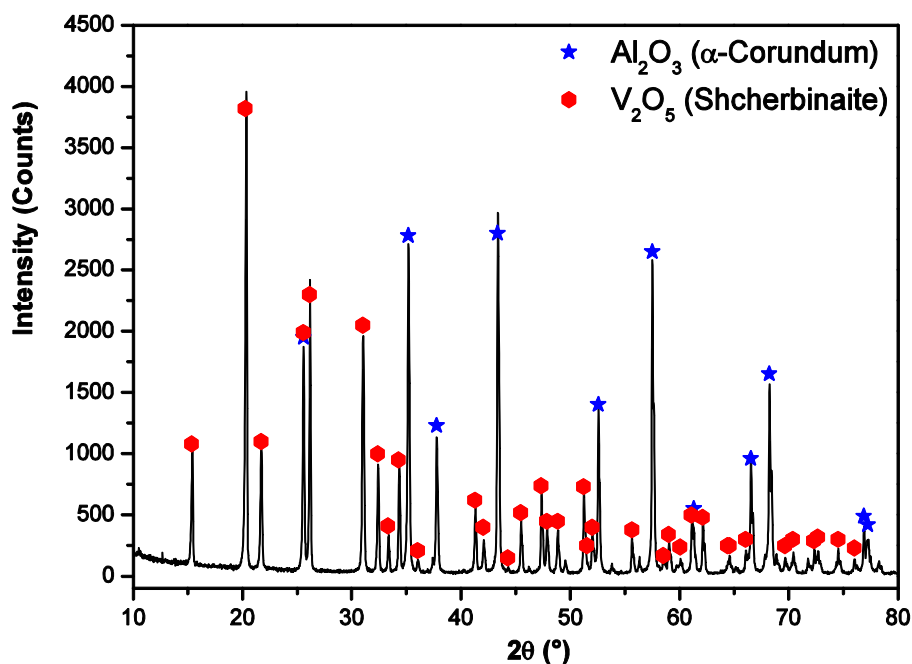
Figure 4-17: VO$_x$/α-Al2O3. XRD phase analysis (aged sample, 5 days at 500 °C in air). No phase transition is visible.

Magnesia Supported Vanadium Oxide Catalyst

In Figure 4-18 the results for the VO$_x$/MgO catalyst are depicted.
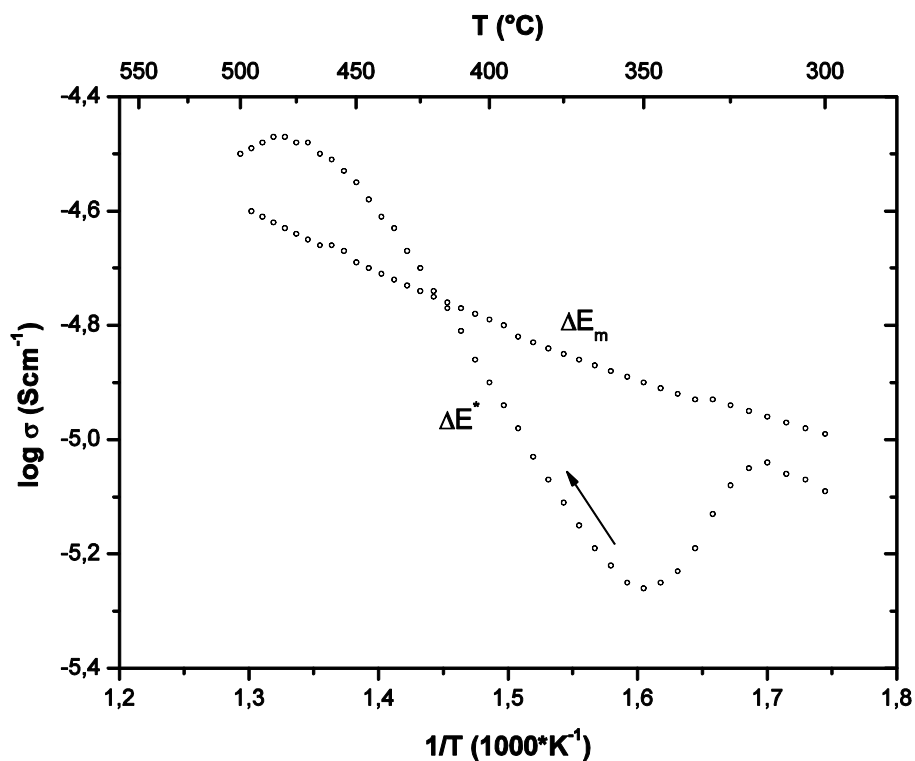
Figure 4-18: VO$_x$/MgO. Arrhenius plot of the conductivity in oxygen (0.5 K/min) with the corresponding propane conversion. On heating above 450 °C a deviation from the linear behaviour is visible. The arrow shows the direction of heating.

The conductivity shows stronger changes on heating than the $VO_x/\alpha\text{-}Al_2O_3$ catalyst. First the conductivity reaches a local maximum at about 325 °C and then drops into a minimum at 350 °C. With increasing temperature the conductivity rises linearly from 375 °C to 430 °C giving an apparent activation energy $\Delta E^* = 0.75 \pm 0.05$ eV. The conductivity reaches a global maximum at 475 °C and declines until 500 °C. On cooling no further deviation from linearity is observed down to 300 °C and a migration energy $\Delta E_m = 0.21 \pm 0.01$ eV results from linear regression. A defect formation enthalpy of $\Delta H_f = 1.62 \pm 0.09$ eV was calculated using these values. XRD phase analysis (Figure 4-19) of the aged sample gave evidence for MgO, V_2O_5 and larger amounts of mixed compounds (MgV_2O_6, $Mg_2V_2O_7$ and $Mg_3(VO_4)_2$).
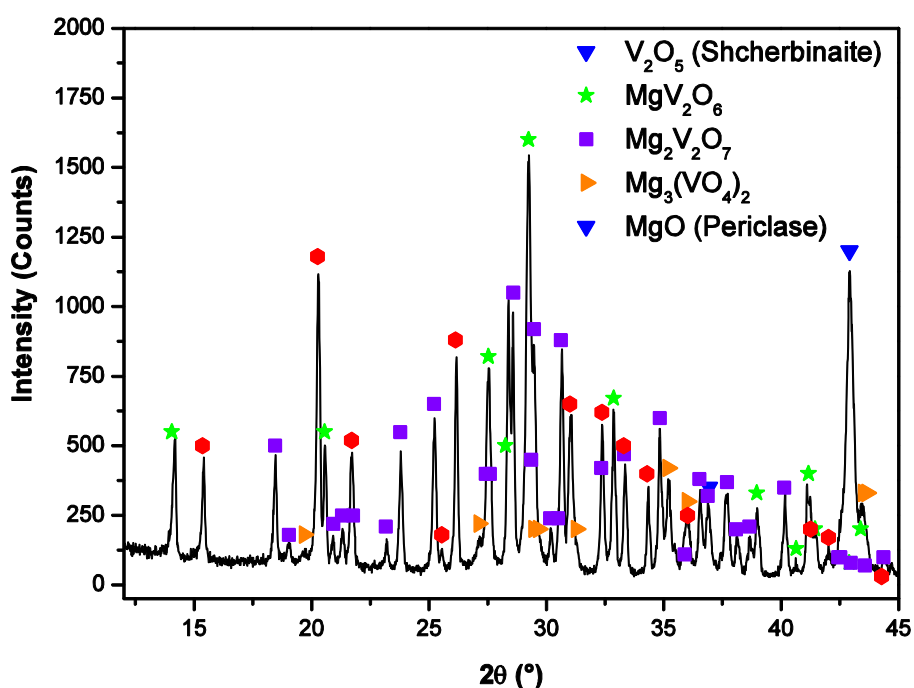

Figure 4-19: **VO_x/MgO. XRD phase analysis (aged sample, 5 days at 500 °C in air). A transition to MgO spinel phases is observed that might be responsible for the non-linearity above 450 °C in the conductivity plot.**

Silica Supported Vanadium Oxide Catalyst

The data for the VO_x/SiO_2 catalyst is displayed in Figure 4-20. The conductivity shows a simple temperature dependency with reaching a linear region at 370 °C with an apparent activation energy of $\Delta E^* = 0.57 \pm 0.01$ eV. On cooling from 500 to 300 °C a migration energy of $\Delta E_m = 0.20 \pm 0.01$ eV is obtained. This results into a defect formation enthalpy of $\Delta H_f = 1.11 \pm 0.08$ eV.

Figure 4-20: VO_x/SiO_2. **(a) Arrhenius plot of the conductivity in oxygen with the corresponding propane conversion. The arrow shows the direction of heating.**

XRD phase analysis of the aged sample (Figure 4-21) shows the presence of V_2O_5 and SiO_2.
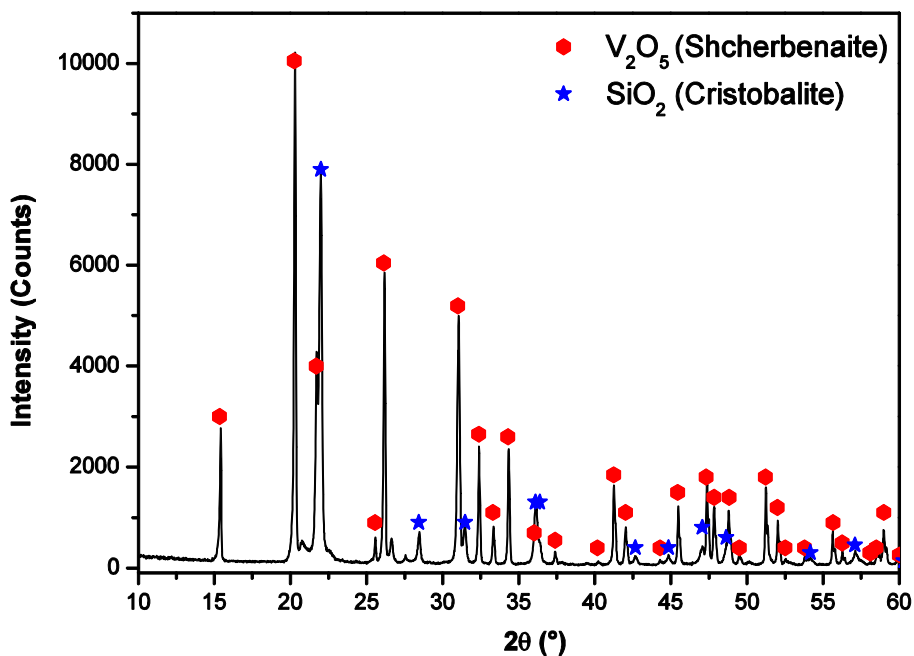
Figure 4-21: VO_x/SiO_2. **XRD phase analysis (aged sample, 5 days, 500 °C, air). No new phases evolve.**

Titania Supported Vanadium Oxide Catalyst

Figure 4-22 depicts the conductivity results of the VO_x/TiO_2 catalyst.
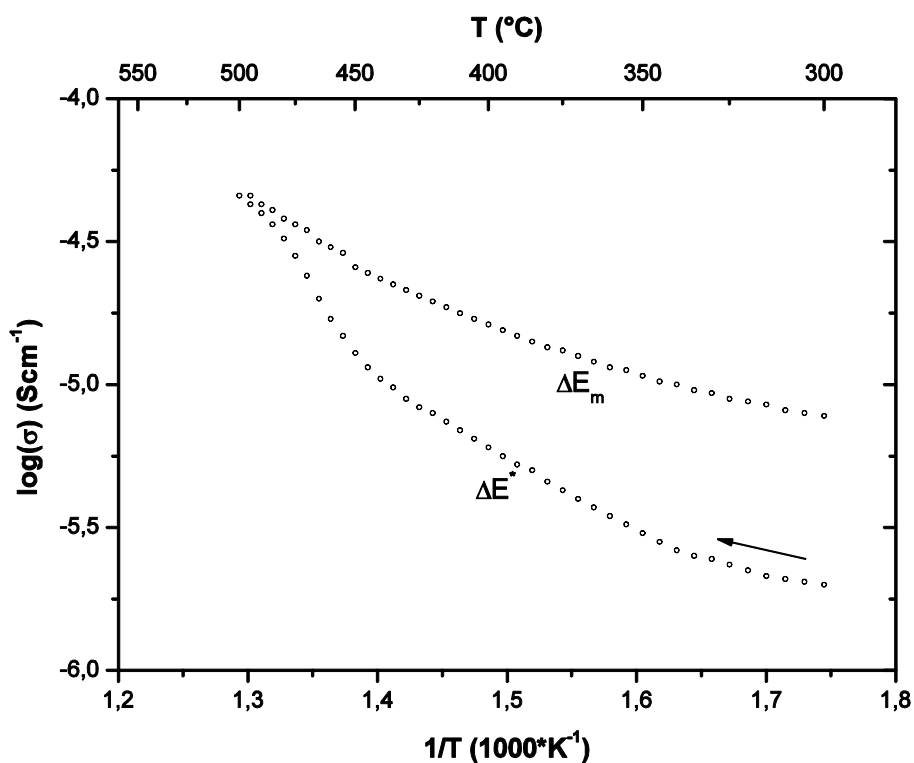
Figure 4-22: **VO$_x$/TiO$_2$. Arrhenius plot of the conductivity in oxygen with the corresponding propane conversion. On heating a transition reagion around 480 °C is evident. The arrow shows the direction of heating.**

A thermally activated region is present at 350 to 450 °C with an apparent activation energy $\Delta E^* = 0.56 \pm 0.06$ eV. Above 450 °C a transition to a different activated region is visible that may exist above 500 °C. On cooling a linear slope is obtained in the same range as on heating (450 °C to 350 °C) resulting into a migration energy of $\Delta E_m = 0.25 \pm 0.02$ eV. The calculated defect formation enthalpy for this catalyst is $\Delta H_f = 0.55 \pm 0.06$ eV. V_2O_5 and the TiO$_2$ phases Anatase as well as Rutile are detected in the aged sample (Figure 4-23).
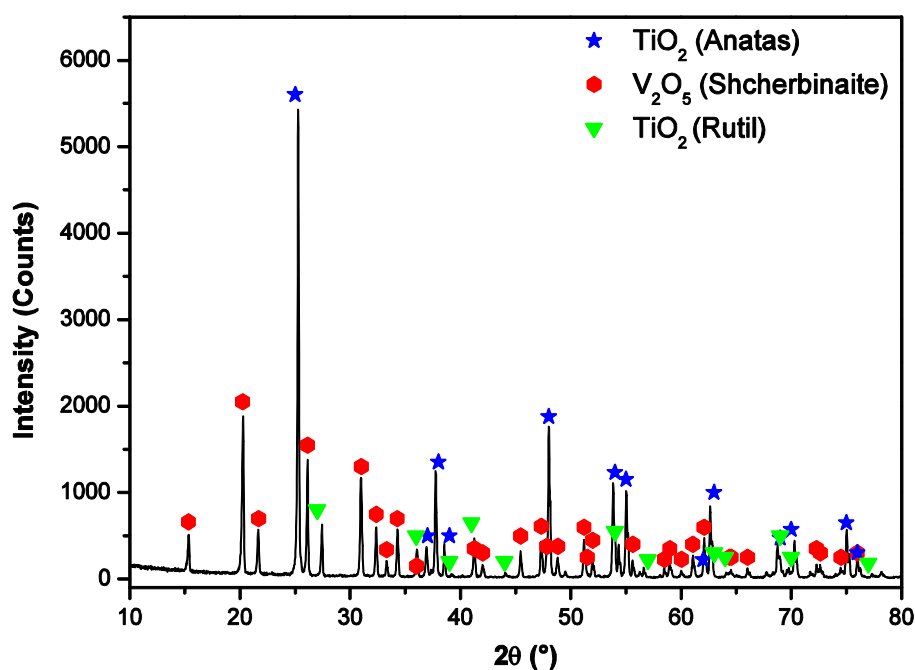
Figure 4-23: VO$_x$/TiO$_2$ XRD phase analysis (aged sample, 5 days, 500 °C, air). A transition to the rutile TiO$_2$ can be seen and may cause the transition region in the conductivity plot.

Zirconia Supported Vanadium Oxide Catalyst

Figure 4-24 shows the conductivity hysteresis of the VO$_x$/m-ZrO$_2$ catalyst.
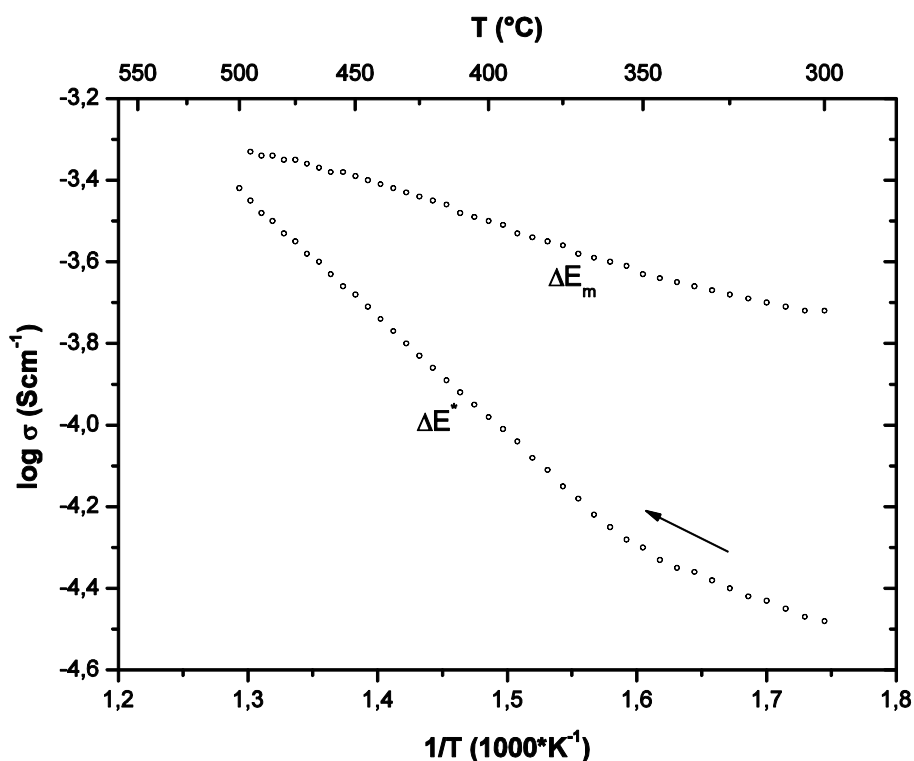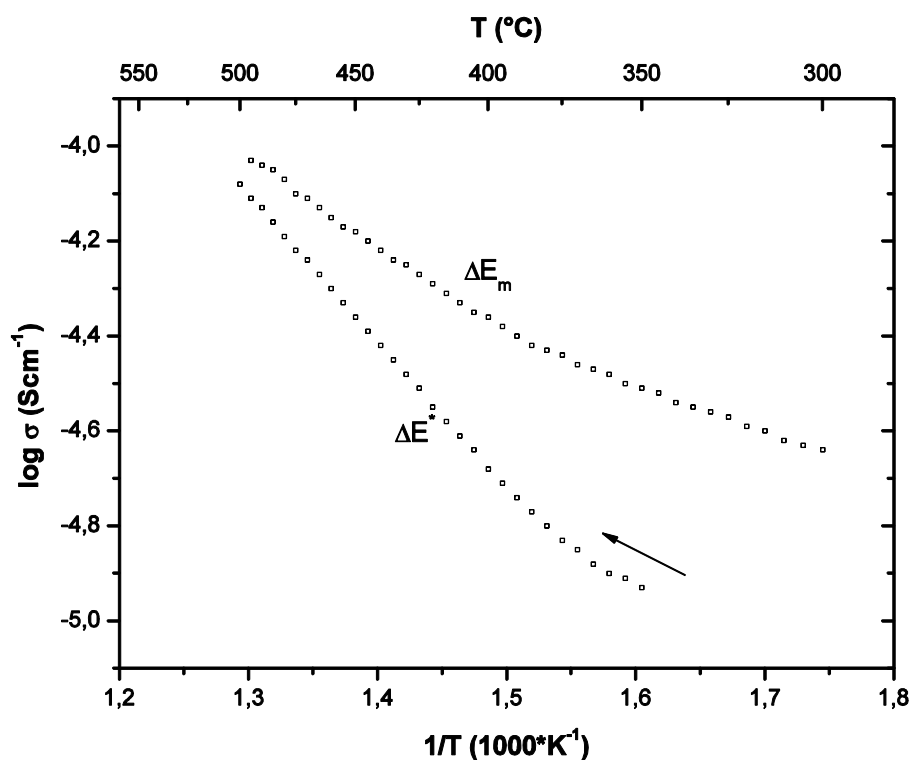

Figure 4-24: VO$_x$/m-ZrO$_2$. (a) Arrhenius plot of the conductivity in oxygen with the corresponding propane conversion. The arrow shows the direction of heating.

On heating, the onset of the linear region is 400 °C and remains for the whole temperature range. The apparent activation energy is $\Delta E^* = 0.63 \pm 0.02$ eV. On cooling the conductivity shows linear behaviour down to 400 °C with a migration energy of $\Delta E_m = 0.35 \pm 0.02$ eV and results into a defect formation enthalpy of $\Delta H_f = 0.85 \pm 0.01$ eV. Ageing of VO_x/m-ZrO_2 gave XRD pattern for monoclinic ZrO_2 and V_2O_5 (Figure 4-25).
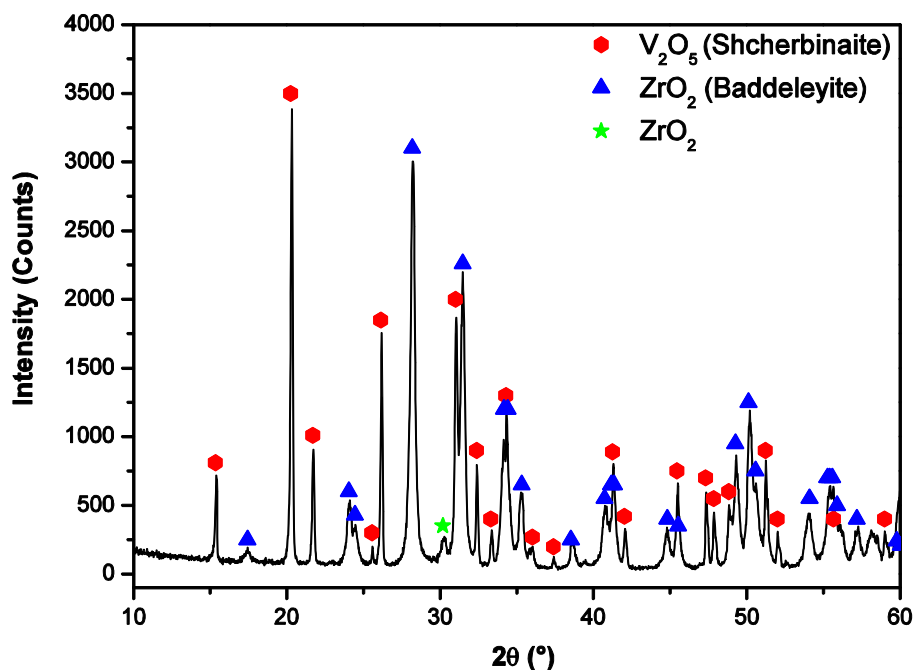
Figure 4-25: **VO_x/m-ZrO_2. XRD phase analysis (aged sample, 5 days, 500 °C, air). No new phases develop.**

Table 4-3: **Activation energies (apparent activation energy ΔE^*, migration energy ΔE_m), defect formation enthalpies (ΔH_f) and propane activation energy E_a for supported VO_x-catalysts with high loading.**

| Sample	T_{onset} (°C)	ΔE^* (eV)	ΔE_m (eV)	ΔH_f (eV)	E_a (eV)
V_2O_5	380-500	0.66 ± 0.04	0.23 ± 0.01	1.3 ± 0.1	0.73 ± 0.04
VO_x/TiO_2	350-450	0.56 ± 0.06	0.25 ± 0.02	0.55 ± 0.06	0.70 ± 0.02
VO_x/m-ZrO_2	400-500	0.63 ± 0.02	0.35 ± 0.02	0.85 ± 0.10	0.67 ± 0.05
VO_x/SiO_2	370-500	0.57 ± 0.01	0.20 ± 0.01	1.11 ± 0.08	1.06 ± 0.06
VO_x/MgO	375-430	0.75 ± 0.05	0.21 ± 0.01	1.62 ± 0.09	0.90 ± 0.01
VO_x/α-Al_2O_3	400-500	1.4 ± 0.1	0.50 ± 0.1	2.8 ± 0.3	1.13 ± 0.09

4.1.2.2. Defect Formation

The onset temperature of oxygen point defect formation is quite similar for all the catalysts and is in the range of 350 to 400 °C. When V_2O_5 is supported on MgO and TiO_2 (Anatase) the

slope of conductivity changes nonlinearly on heating above 475 and 450 °C, respectively. The catalysts with α-Al_2O_3, SiO_2 and m-ZrO_2 exhibit linear temperature dependency in the full temperature range. XRD on aged samples shows for the supports MgO and TiO_2 (Anatase) a transition to mixed compounds while for α-Al_2O_3, SiO_2 and m-ZrO_2 no transition is observed. Magnesia forms together with V_2O_5 several spinel phases like shown in Figure 4-19 and in thermal investigations done in [84]. Said and El-Wahab [85] found a decrease of conductivity on spinel formation and a migration energy of 0.24 eV which both is in agreement with results of this work on VO_x/MgO. In order to investigate the influence of the phase transition on the defect formation enthalpy, conductivity experiments were done below the transition temperature (300 to 425 °C) (see appendix: Figure 7-1). These experiments gave an oxygen defect formation enthalpy of $\Delta H_f = 1.7 \pm 0.1$ eV. This value is very close to the enthalpy determined with a temperature scan above the transition region (1.62 ± 0.09 eV) and it is concluded that the influence is negligible. It was shown in [65,86] that V_2O_5 facilitates the transition of Anatase to Rutile via incorporation of vanadium into the TiO_2 lattice. The transition temperature was found to be 525 °C and therefore above the temperature of 450 °C obtained from the Arrhenius plot in Figure 4-22. But it is possible, that minute amounts of Rutile are formed already at 450 °C and alter the electrical properties of the catalyst. These small amounts would not have been detected by XRD or DTA applied in [86]. Further indication for this mechanism is the presence of Rutile after prolonged heating of the sample at 500 °C (Figure 4-23). Different defect formation enthalpies are found depending on the support giving following ranking: VO_x/TiO_2 < VO_x/m-ZrO_2 < VO_x/SiO_2 < V_2O_5 < VO_x/MgO < VO_x/α-Al_2O_3. This is displayed in Figure 4-26 together with reference data.
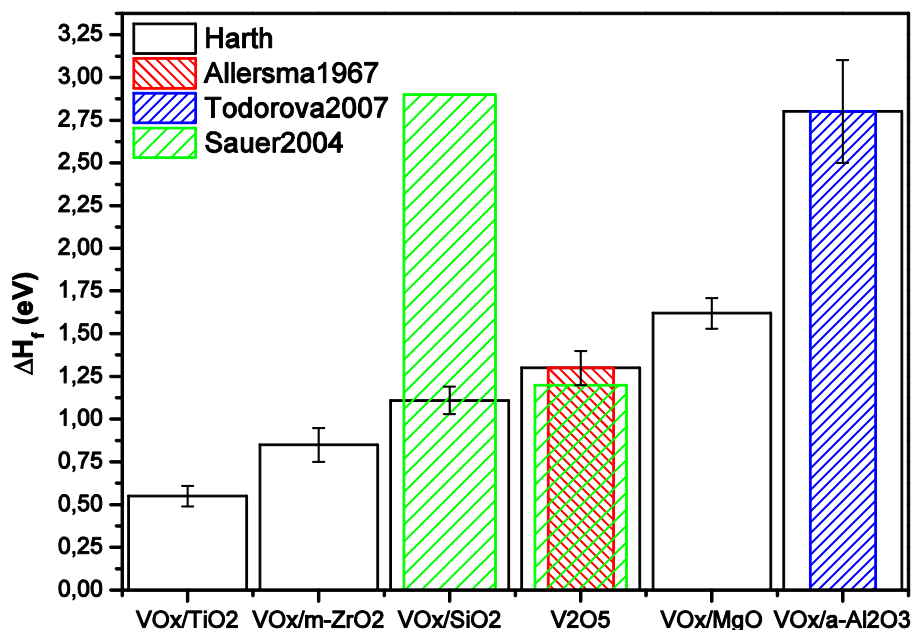
Figure 4-26: Comparison of defect formation enthalpies ΔH_f with literature data. Red [43], green [13], blue [16]. These are the results for the catalysts with high loading in oxygen with a heating rate of 0.5 K/min.

As discussed in the previous chapter (4.1.1.3), there are experimental [43] (1.3 eV) and calculated [13] (1.17 eV) results for pure V_2O_5 that are in good agreement with the experiments in this work (1.3 ± 0.1 eV). Furthermore, Todorova calculated for α-Al_2O_3 supported VO_x a defect formation enthalpy of 2.8 eV [16] which is also consistent with the result of 2.8 ± 0.3 eV. Calculations for VO_x on SiO_2 yield a defect formation enthalpy of 2.9 eV [13] which is in contradiction with the value of 1.11 ± 0.08 eV derived from the conductivity experiments. Different aspects may influence the result of the experiments and calculations, like the presence of impurities at the grain boundaries, phase transitions, percolation aspects or the chosen conditions and models for the calculations. The impact of percolation properties of a 2-phase mixture M_xO_y/VO_x will be discussed in Chapter 4.1.3 together with the influence of the interface support and active compound on the defect formation.

4.1.3. Concentration Dependent Conductivity of Supported Catalysts

In order to determine the kinetic path of the charge carriers and therefore the region that is characterized, the concentration dependent properties of $VO_x/m-ZrO_2$ and VO_x/SiO_2 catalysts are investigated. Furthermore, this gives the possibility to probe whether catalysts of low loading are suitable for this method.

In Figure 4-27 Arrhenius plots for VO_x/SiO_2 at different concentrations are depicted. On heating and cooling they show different apparent activation energies ΔE^* and migration energies ΔE_m, respectively, like discussed in Chapter 4.1.1.1 and 4.1.2.
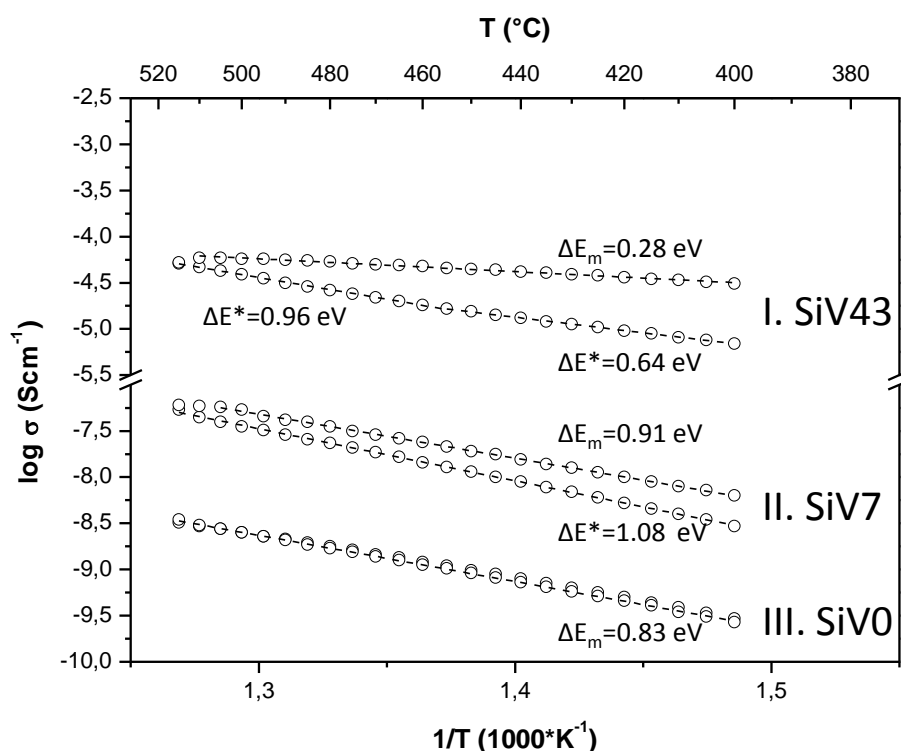
Figure 4-27: **Change of temperature dependency of conductivity in oxygen with concentration for VO_x/SiO_2-catalysts.**

This behaviour is categorized into 3 regions:

Region (I): At high concentration activation energies close to pure vanadium pentoxide and the highest conductivity is found. But on heating above 480 °C a transition to higher activation energy is already observed.

Region (II): Here a smaller hysteresis is present and activation energies of approximately 1 eV are found.

Region (III): Without vanadium pentoxide no hysteresis appears and the activation energy is lower than in region (II). These features will be discussed in this chapter.

Figure 4-28 and Figure 4-29 (page 55) show the total conductivity of VO_x/SiO_2 and VO_x/m-ZrO_2 as a function of V_2O_5 loading at 400, 450 and 500 °C. It is apparent that the conductivity behaviour for both catalysts can be divided into 3 regions:

Region (I): It shows a comparably high conductivity with $6.4*10^{-4}$ Scm^{-1} at 500 °C for pure vanadium pentoxide. With lower concentration a slight decrease of the conductivity is evident showing nearly a linear concentration dependency. A sudden drop at a mass fraction of 25 % (VO_x/SiO_2) and 20 % (VO_x/m-ZrO_2) is visible.

Region (II): In this region the VO_x/SiO_2 catalyst starts to plateau below $w = 20$ % at $1*10^{-7}$ Scm^{-1}. VOx/m-ZrO_2 shows similar behaviour and the conductivity appears to level out at $4.9*10\text{-}7$ Scm^{-1} at 7.2 m% V_2O_5 but jumps with the mass fraction lowered to 3.6 % to $7.1*10^{-7}$ Scm^{-1}.

Region (III): For both catalysts the conductivity drops without vanadium pentoxide to very low conductivity. For VO_x/SiO_2 the conductivity descends below $w = 7$ % down to $2.5*10^{-9}$ Scm^{-1}. The zirconia supported catalysts shows a conductivity one order of magnitude higher: $2.9*10^{-8}$ Scm^{-1}.
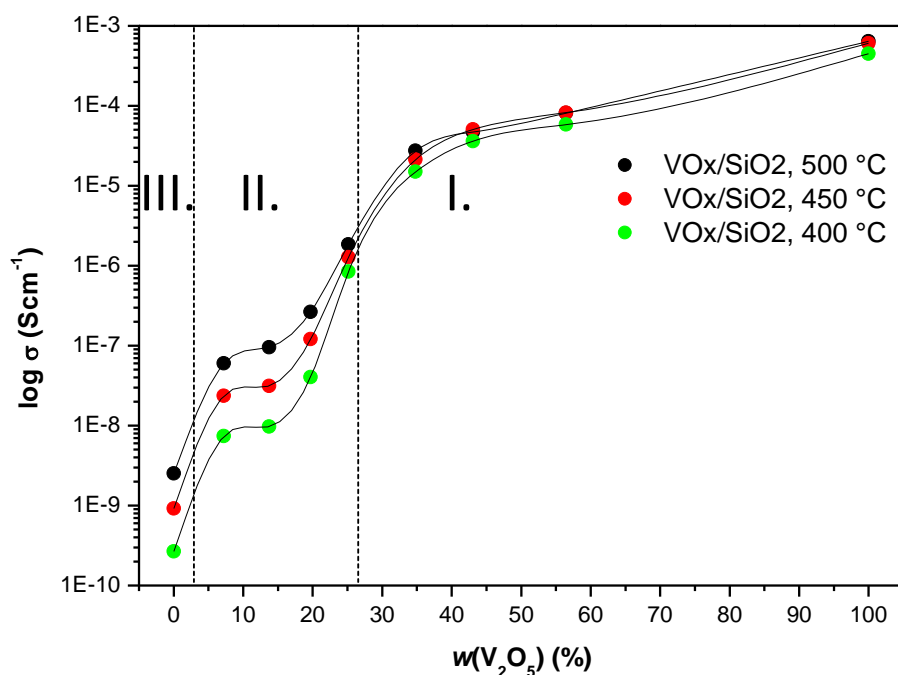
Figure 4-28: Concentration dependent conductivity of VO_x/SiO_2 catalyst at different temperature in O_2.
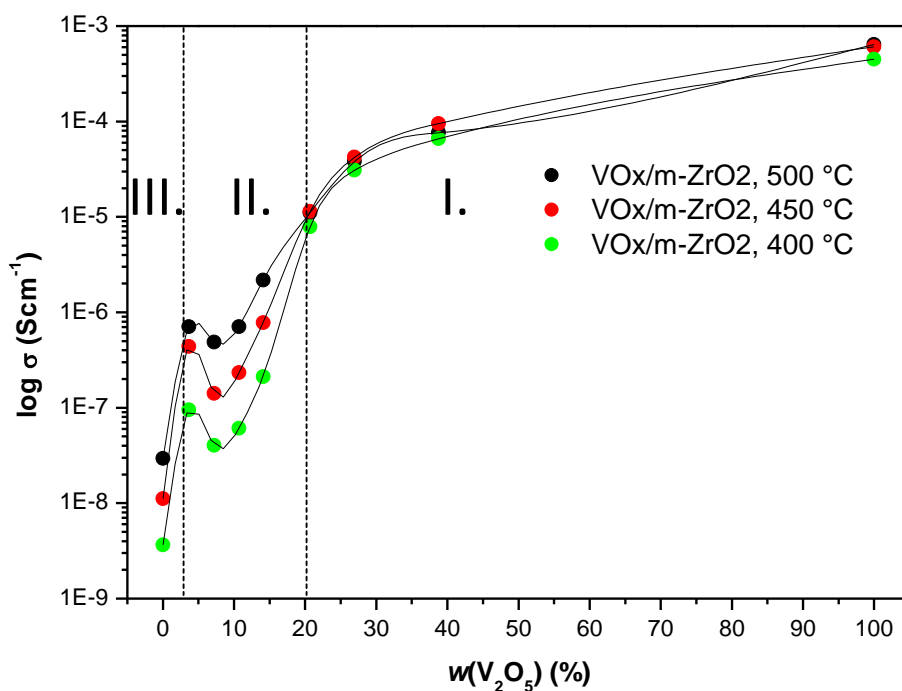
Figure 4-29: Concentration dependent conductivity of $VO_x/m\text{-}ZrO_2$ catalyst at different temperature in O_2.

The catalysts consist of a 2 phase mixture: V_2O_5 and the support SiO_2 or m-ZrO_2. Figure 4-30 shows the element distribution of vanadium (red) and silicon (yellow) at cross sections of VO_x/SiO_2 pellets used for conductivity experiments. This picture illustrates the percolation of SiO_2 and V_2O_5. At $w = 43\,\%$ a network of connected V_2O_5 areas is visible. With lower concentration these areas are getting smaller until at $w = 25\,\%$ most of the junctions vanish. Then at $w = 7\,\%$ the EDX mapping shows a homogeneous distribution of Si and V. These observations are consistent with the change of electrical properties in the same concentration range.

SiV43%   SiV35%   SiV25%

SiV20%   SiV7%

Si

V
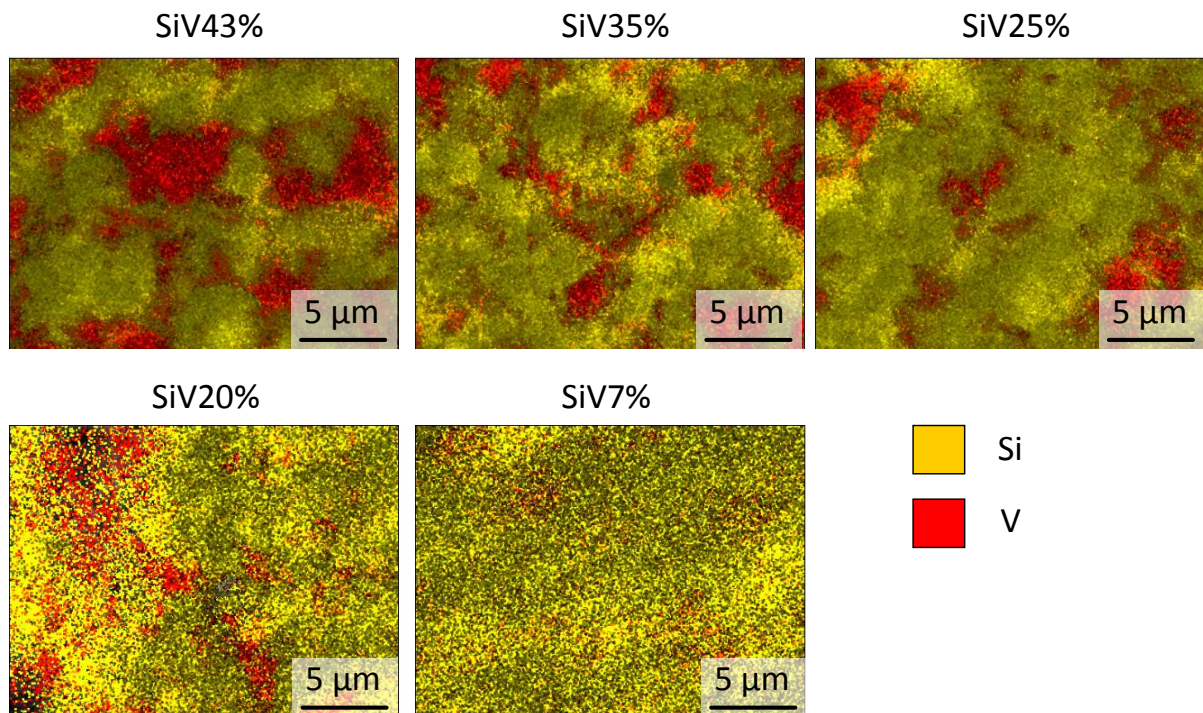
Figure 4-30: **EDX mapping of VO$_x$/SiO$_2$ cross sections. The element distribution of Si and V is shown for catalysts with different loadings. 14 kV, 5000x magnification.**

The conductivity of VO_x/SiO_2 and VO_x/m-ZrO_2 in Figure 4-28 and Figure 4-29 shows at high concentration in region (I) a conductivity close to that of pure V_2O_5. Furthermore a nearly linear concentration dependency is evident down to approximately $w = 30\,\%$. V_2O_5 is an n-type semiconductor and the supports are isolators with conductivities several orders of magnitude lower. Therefore at high concentration V_2O_5 forms a kinetic path for electrons. If its amount is reduced, the conducting cross section decreases. Due to the proportionality of the conductivity σ to the cross section A

$$\sigma = l/(RA)$$
4-7

the conductivity is lowered. Therefore in region (I) the properties of the V_2O_5 matrix phase dominate. This is visualized in Figure 4-31 (a).

<div align="center">(a)   (b)</div>
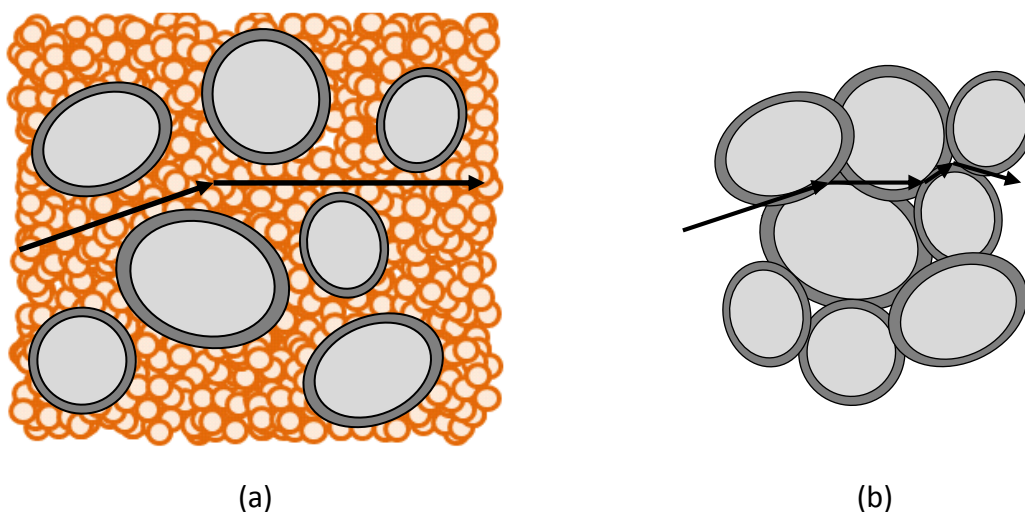
Figure 4-31: **Conductivity percolation model. The arrows indicate the kinetic path for the charge carriers. At high loading (a) a better conducting V_2O_5 matrix (orange) is present. At low loading (b) the percolation path through V_2O_5 vanishes and a new kinetic path along the interface M_xO_y/VO_x is formed (dark grey).**

The descent to a plateau in region (II) and the drop in region (III) cannot be explained by a simple mixture of 2 phases. In that case in region (II) the properties of the support would dominate and no further change like observed in region (III) would occur. A percolation model comprising an interface is suitable for explaining the experimental results and is depicted in Figure 4-31 (b). The junctions in the V_2O_5 matrix vanish at about $w = 30\,\%$ (see EDX mapping in Figure 4-30) and the conductivity drops to region (II) reflecting now the properties of the interface. The second percolation threshold in region (III) shows the transition to the isolator properties of the pure support. The sharp increase in conductivity for VO_x/m-ZrO_2 at $w = 7.2\,\%$ near the transition to region (III) may be caused by doping effects and hence promote electronic or ionic conduction. The temperature dependency in region (I) is less pronounced than in region (II) or (III) indicating a change in activation energy and transport mechanism.

4.1.3.1. Transport mechanism

In Figure 4-32 the total conductivity for VO_x/SiO_2 and VO_x/m-ZrO_2 at 500 °C is shown.
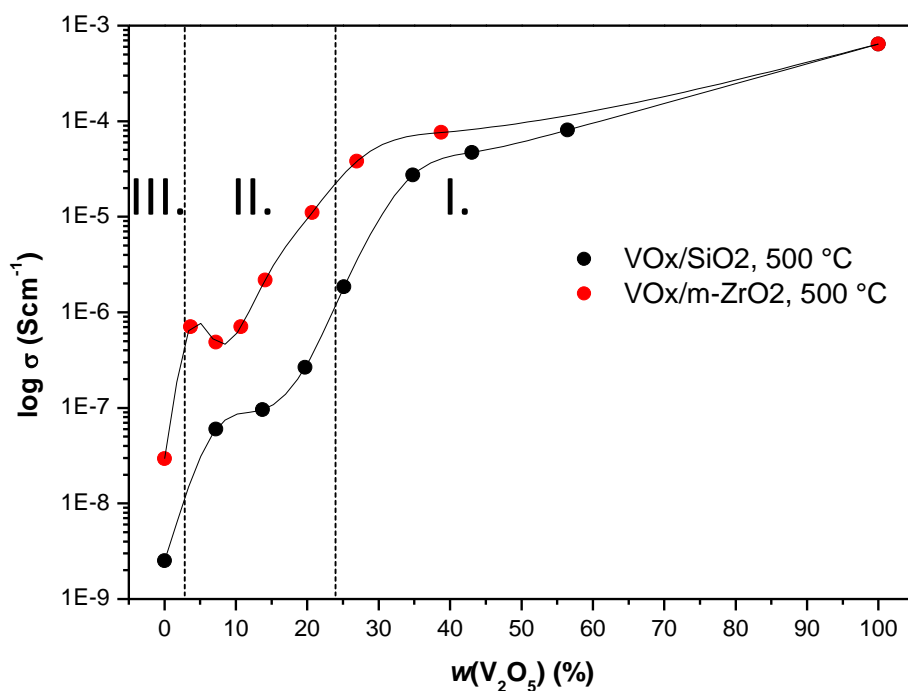
Figure 4-32: Conductivity percolation behaviour for VO$_x$/SiO$_2$ and VO$_x$/m-ZrO$_2$ at 500 °C in O$_2$.

Already at high concentration (region I) the support alters the electrical properties and VO$_x$/m-ZrO$_2$ exhibits a slightly higher conductivity. Below the drop in region (II) and (III) this difference is substantial and rises up to 1 order of magnitude.
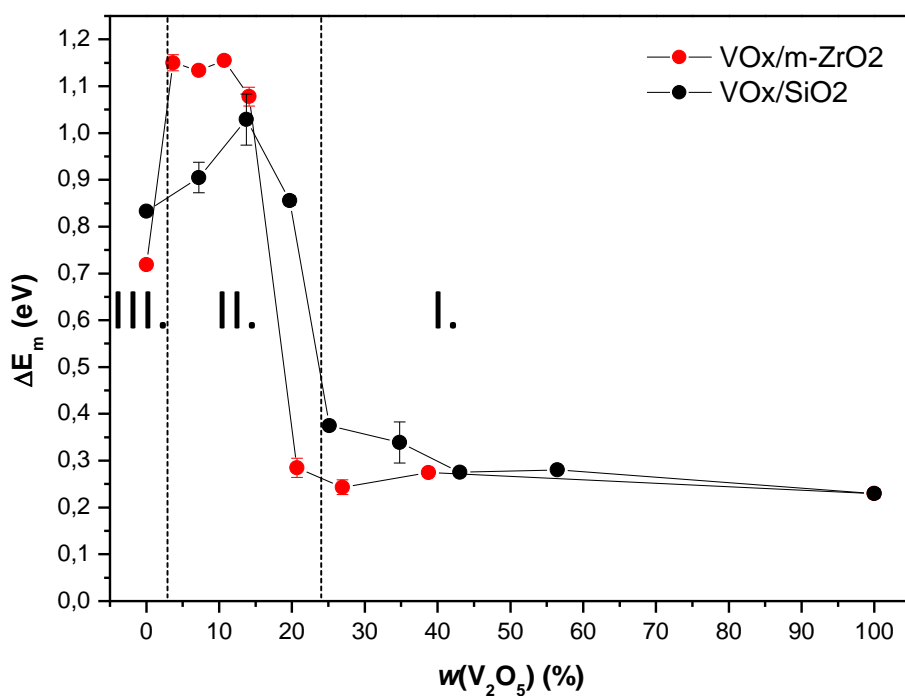
Figure 4-33: Migration energy for VO$_x$/SiO$_2$ and VO$_x$/m-ZrO$_2$ at 500 °C in O$_2$.

Figure 4-33 depicts the V_2O_5 concentration dependent migration energy ΔE_m for both systems. Like the conductivity these are divided into 3 regions that correspond to the conductivity plots in Figure 4-32.

Region (I): At high V_2O_5 mass fractions both catalytic systems exhibit a low migration energy $\Delta E_m \approx 0.3$ eV that is comparable to pure V_2O_5. But when lowering the concentration below $w = 40$ % the migration energy increases for VOx/SiO2 to 0.34 ($w = 34.8$ %) and 0.38 eV ($w = 25.2$ %) while it remains at 0.24 ($w = 27.0$ %) and 0.29 eV ($w = 20.7$ %) for the VO_x/m-ZrO2 catalyst.

Region (II): The migration energy of VO_x/SiO_2 starts to rise rapidly below $w = 25$ % and peaks at $w = 13.7$ % at $\Delta E_m = 1.03$ eV. As shown in the conductivity plots, VO_x/m-ZrO_2 exhibits a threshold lower than VO_x/SiO_2. The same behaviour is observed for the migration energy and the threshold is located at $w = 14.1$ % V_2O_5. At this mass fraction ΔE_m jumps from 0.29 to 1.08 eV and rises further to $\Delta E_m \approx 1.14$ eV. The migration energy remains constant down to a concentration of $w = 3.6$ %.

Region (III): In this region the activation energy descends to lower values and the silica support shows an energy of 0.83 eV while pure m-ZrO_2 exhibits a value of 0.72 eV.

The change of migration energy correlates with the 3 regions observed in the concentration dependent conductivity. Above the percolation threshold in region (I) the migration energy is close to the value for pure V_2O_5. This behaviour is expected for a better conducting V_2O_5 matrix (see Figure 4-31 (a)). In region (II) the migration energies rise to 1.03 eV (VO_x/SiO_2) and 1.14 eV (VO_x/m-ZrO_2) and hence indicate a change of the transport mechanism from electronic to ionic. Because these migration energies are different from the pure oxides in region (III) (0.83 eV for SiO_2 and 0.72 eV for m-ZrO_2) this finding supports the percolation model comprising a transport path along the interface depicted in Figure 4-31 (b). The most likely majority charge carriers at the interface are oxygen ions. The lower activation energies in region (III) might be an indicator for another change of majority charge carriers from anionic to cationic. The higher conductivity of VO_x/m-ZrO_2 (Figure 4-32) in region (I) at high concentration may originate from several effects. The percolation threshold for VO_x/m-ZrO_2 is located at lower concentration than for the VO_x/SiO_2 catalyst. Thus at equal concentration in region (I), VO_x/m-ZrO_2 should exhibit the higher conducting cross section A of the V_2O_5 matrix (see equation 4-7) and therefore a higher conductivity. The higher activation energy

of VO_x/SiO_2 below $w = 40$ % may also be a reason for the lower conductivity of VO_x/SiO_2. At the plateau in region (II) and in region (III) the difference of about 1 order of magnitude may be explained by different charge carrier concentrations or mobilities. But the same difference in conductivity is found for the m-ZrO_2 and SiO_2 in region (III) and therefore the discussed effect in region (II) may also arise due to the intrinsic properties of the supports.

Figure 4-34 to Figure 4-39 show the impedance spectra for VO_x/SiO_2 and VO_x/m-ZrO_2, respectively. In (a) the spectra for the different regions and in (b) the corresponding equivalent circuits are depicted. For VO_x/SiO_2 in region (I) (Figure 4-34) the spectra form perfect semicircles and are therefore modelled using RC-circuits.

(a)   (b)

Figure 4-34: **(a) Nyquist plot of VO_x/SiO_2 at 500 °C in O_2 in region (I) and (b) the corresponding equivalent circuit: 1: resistor, 2: constant phase element.**

In region (II) the behaviour changes and in Figure 4-35 for VO_x/SiO_2 below $w = 25$ % long stretched semicircles appear. At very low frequency (down to 7 mHz) a small spike is visible. For Figure 4-34 and Figure 4-35 the high frequency arc is attributed to the bulk conductivity. The stretched arc and spike at low frequencies in Figure 4-35 is attributed to an electrode reaction, polarization at the platinum contacts and diffusion of charge carriers through the porous platinum layer [67]. Therefore the Randles-like circuit depicted in Figure 4-35 (b) is used.

(a)   (b)

Figure 4-35: **(a) Nyquist plot of VO$_x$/SiO$_2$ at 500 °C in O$_2$ in region (II). (b) Corresponding equivalent circuit: 1: Charge transfer resistance, 2: Warburg diffusion element, 3: constant phase element for electrode polarization, 4: bulk resistance, 5: bulk capacitance (constant phase element).**

The electrode reaction is described using the charge transfer resistance (1) and Warburg diffusion element (2). The polarization of charge carriers is represented by a constant phase element (3). The bulk resistance (4) is placed in series to the electrode and in parallel the bulk polarization (5). Best fit results gave the model with the bulk polarization parallel to bulk resistance as well as parallel to the electrode elements. The electrode reaction in the impedance plots is present in the entire region (II). But in region (III) with pure SiO$_2$ the Nyquist plot takes again the form of a perfect semicircle.

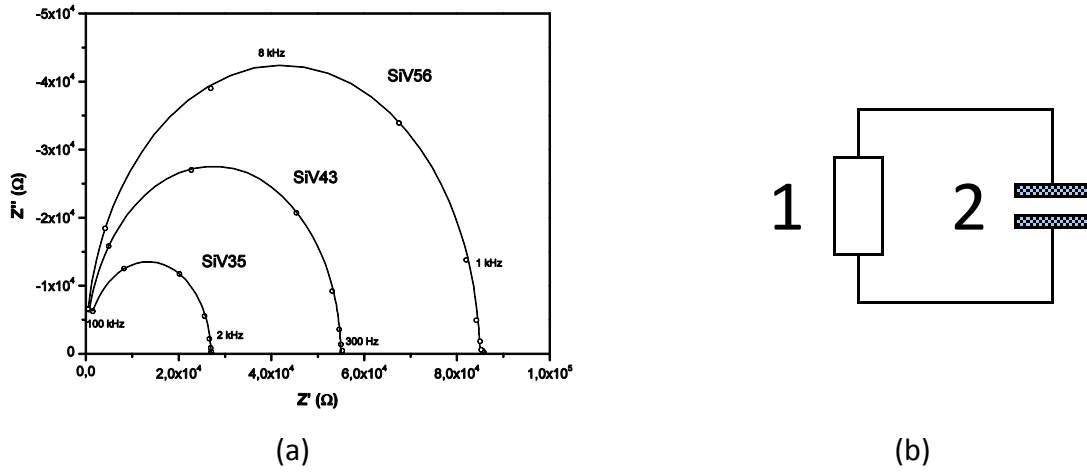(a)   (b)
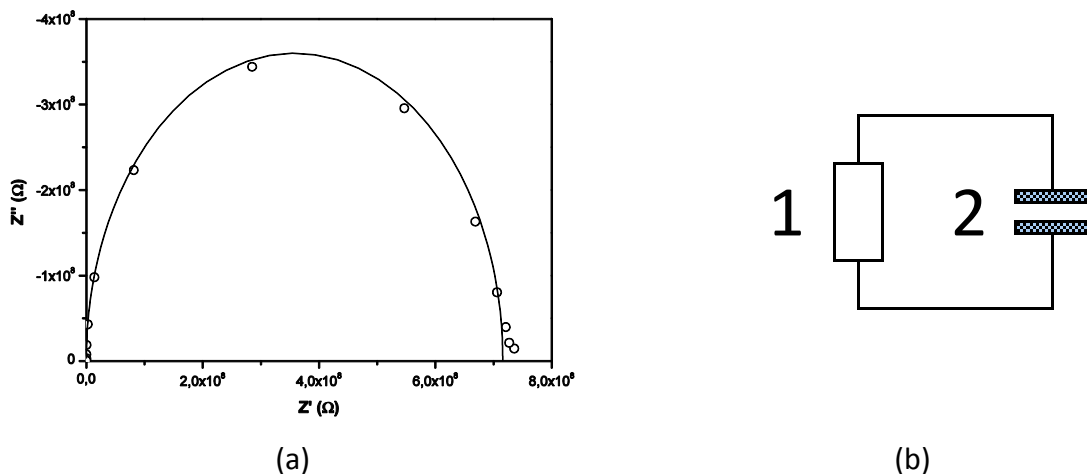
Figure 4-36: **(a) Nyquist plot of VO$_x$/SiO$_2$ at 500 °C in O$_2$ in region (III). (b) Corresponding equivalent circuit: 1: resistor, 2: constant phase element.**

Similar behaviour is observed for VO$_x$/m-ZrO$_2$ shown in Figure 4-37 to Figure 4-39. Above the threshold in region (I) perfect semicircles are present. At lower concentration in region (II) a

low frequency electrode arc starts to appear. But here in contrast to VO_x/SiO_2 without the electrode spike. Therefore, for modelling the circuit visualized in Figure 4-38 (b) is used.

(a)   (b)
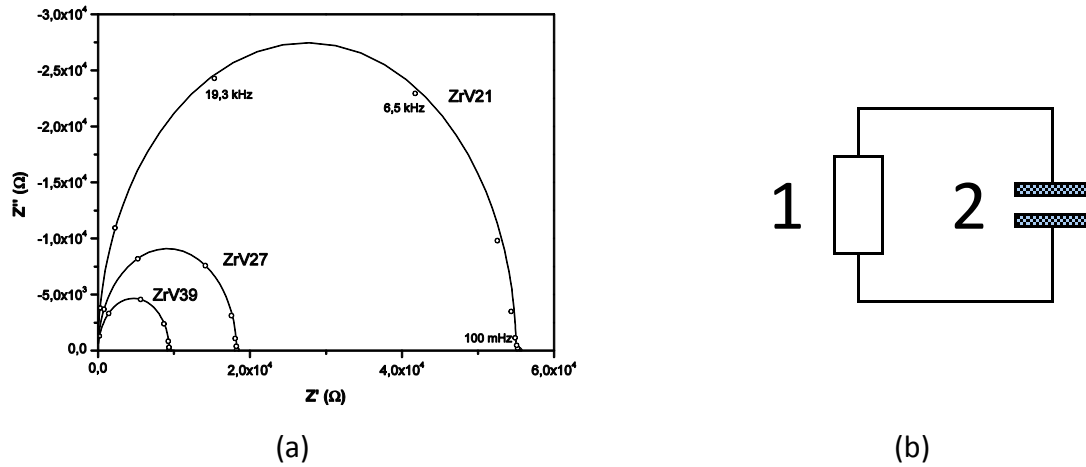
Figure 4-37: **(a) Nyquist plot of ZrV$_x$ at 500 °C in O$_2$ in region (I). (b) Corresponding equivalent circuit: 1: resistor, 2: constant phase element.**

It consists of the bulk response (bulk resistance (1) and bulk capacitance (2)) and of the electrode reaction (charge transfer resistance) (3) and electrode polarization (constant phase element) (4). Then in region (III) the electrode arc disappears and is replaced by a depressed arc that is best modelled using 2 RC-circuits in series (Figure 4-39 (b)).

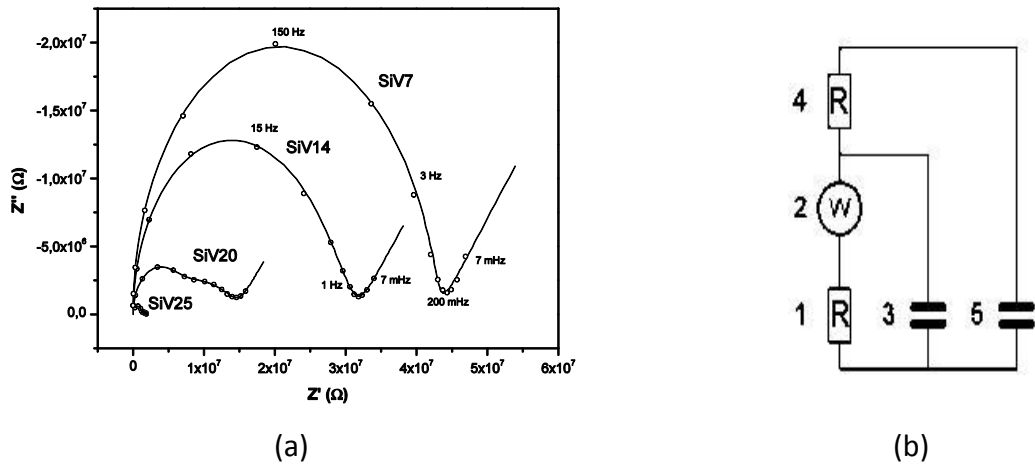(a)   (b)

Figure 4-38: **(a) Nyquist plot of ZrVx at 500 °C in O$_2$ in region (II). (b) Corresponding equivalent circuit: 1: Charge transfer resistance, 2: constant phase element for electrode polarization, 3: bulk resistance, 4: bulk capacitance (constant phase element).**
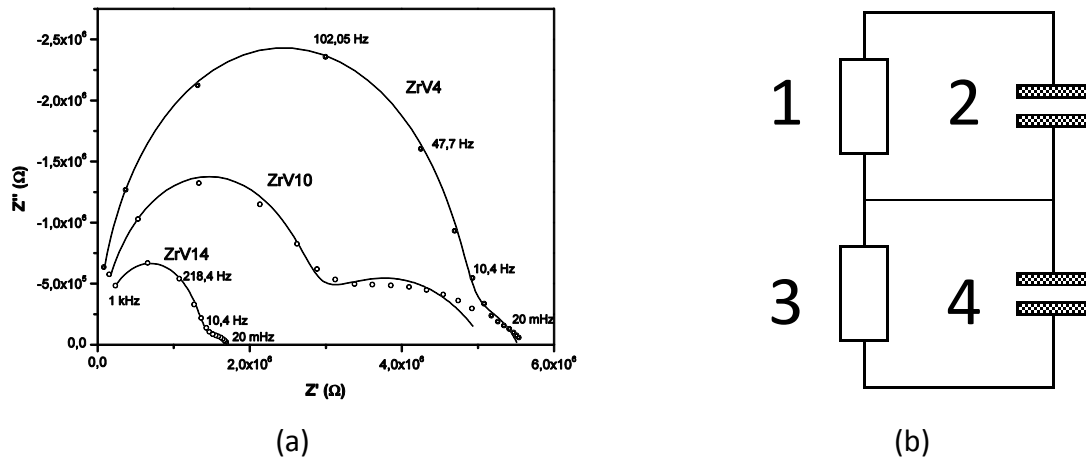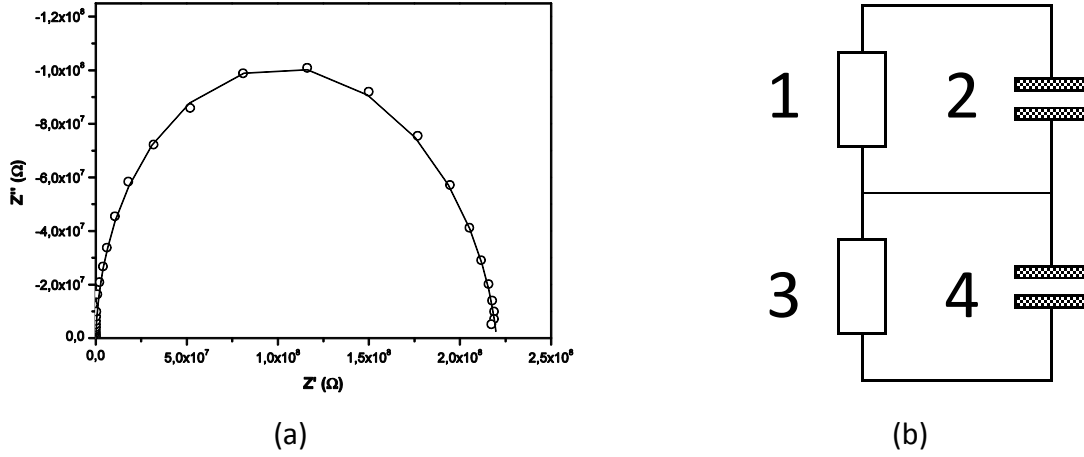
Figure 4-39: **(a) Nyquist plot of ZrVx at 500 °C in O$_2$ in region (III). (b) Corresponding equivalent circuit: 1: Charge transfer resistance, 2: constant phase element for electrode polarization, 3: bulk resistance, 4: bulk capacitance (constant phase element).**

The appearance of the impedance plots changes in correlation with the 3 regions in the conductivity plots and indicates changes in the transport mechanism. The absence of an electrode polarization in region (I), for both the VO$_x$/SiO$_2$ and VO$_x$/m-ZrO$_2$ catalyst, gives evidence for electronic conduction at high concentration through a V$_2$O$_5$ matrix, because platinum contacts reversible for electrons are used. The polarization apparent in Figure 4-35 and Figure 4-38 for compositions in region (II) is an indicator for ionic charge carriers blocked at the metal electrodes. In region (III) the polarization vanishes and shows again the change of transport mechanism. Again, this behaviour is in agreement with the proposed interface percolation model in Figure 4-31. A similar conductivity percolation of a mixed conductor is discussed in [87].

4.1.3.2. Defect Formation at the Interface Region

The interface exhibits properties other than the pure phases. Therefore the defect formation enthalpies were determined according to the approach in Chapter 4.1.1.3. Figure 4-40 and Figure 4-41 depict defect formation enthalpies ΔH_f as a function of V$_2$O$_5$ concentration together with the total conductivity. Figure 4-40 shows the results for VO$_x$/SiO$_2$. Region (I) exhibits a high defect formation enthalpy close to the value ΔH_f = 1.3 eV of pure V$_2$O$_5$. Then in region (II) at w = 13.7 % it drops to about 0.5 eV.
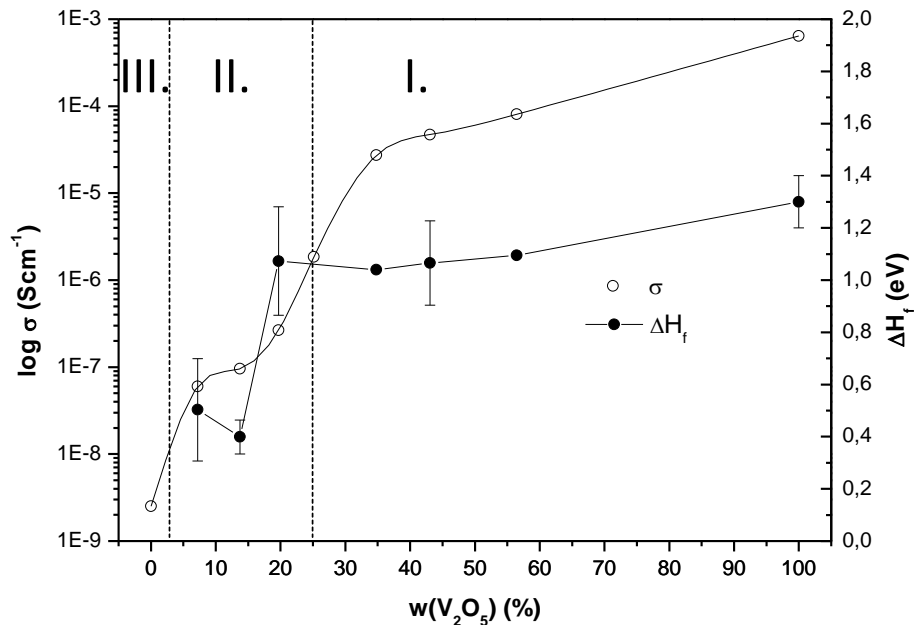
Figure 4-40: **Defect formation enthalpy and total conductivity of VO$_x$/SiO$_2$ catalysts at different concentrations.**

A similar behaviour is observed for VO$_x$/m-ZrO$_2$ in Figure 4-41. Region (I) shows a constant defect formation enthalpy of 1.3 eV and is lowered in region (II) at 14 and w = 11 % to approximately 0.7 eV. Then at w = 3.6 % a moderate decrease to 0.54 eV is observed.
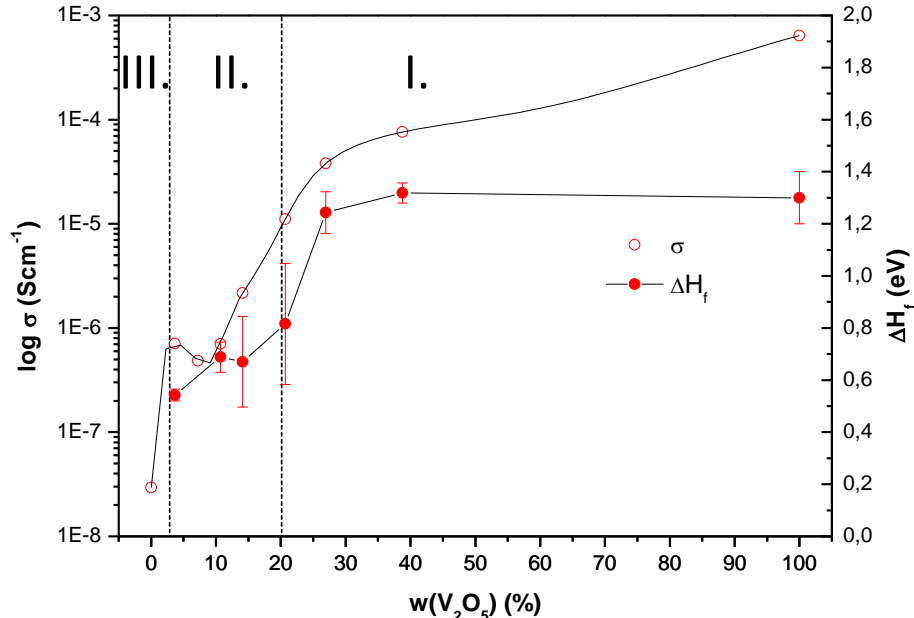
Figure 4-41: **Defect formation enthalpy and total conductivity of VO$_x$/m-ZrO$_2$ catalysts at different concentrations.**

The results are in agreement with observations in previous chapters. At high concentration the defect formation enthalpy is close to pure V$_2$O$_5$ because the matrix phase is characterized. In the interface region (II) the enthalpy changes and is lowered. It is expected,

that the defect formation enthalpy plateaus in region (II). The results indicate such behaviour, but more data points are necessary especially for VO_x/SiO_2.

4.1.3.3. Redox Behaviour and VO_x-Species

It was shown that the transport properties change at the interface of vanadium pentoxide and the support. In this chapter the redox properties of theses catalysts are discussed.
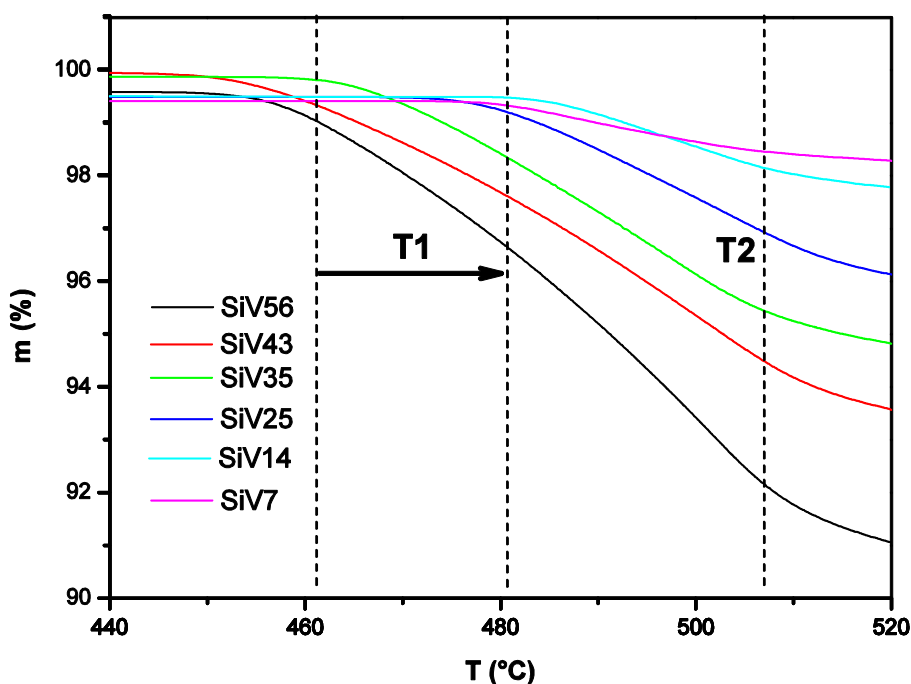
Figure 4-42: TGA in diluted reaction gas (90% N_2/8% Propane/2% O_2) at 2 K/min for VO_x/SiO_2. The mass loss shows a shift to higher reduction temperature (T1) at lower loading.

Figure 4-42 depicts the vanadium pentoxide concentration dependent change of mass loss in reaction gas. In Figure 4-43 the corresponding 1st derivatives are shown. In Figure 4-42 the onset of reduction is labelled as T1 and a shift to higher temperature is evident for lower loading.
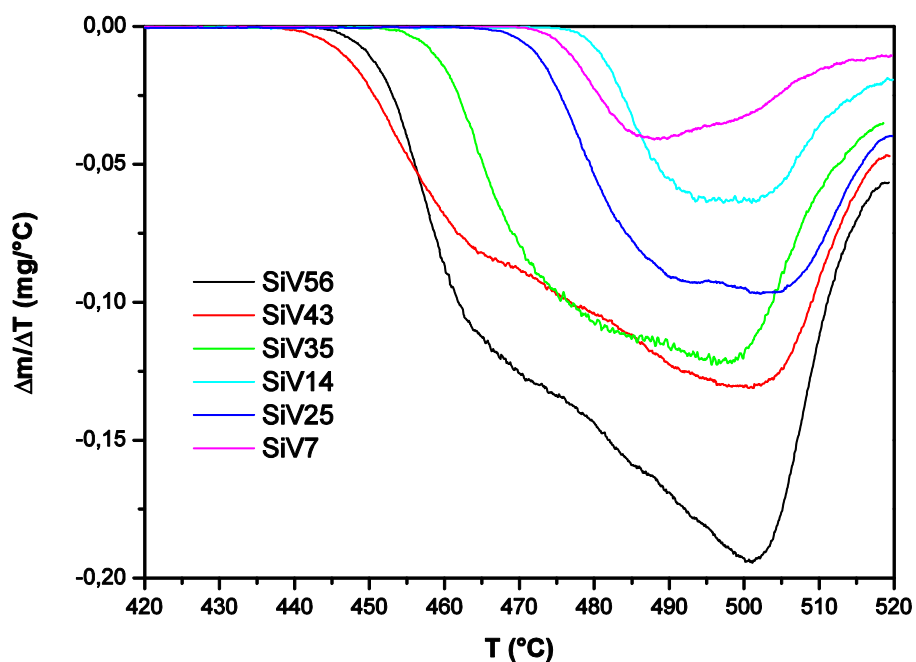
Figure 4-43: TGA in reaction gas at 2 K/min for VO$_x$/SiO$_2$. The 1st derivative shows that several processes are superimposed.

The derivative depicted in Figure 4-44 shows a very complex temperature dependency. Because the ODP is a redox reaction, several processes are superimposed and as a result the interpretation is difficult. Furthermore, the catalyst in the thermo balance was exposed to the atmosphere in a crucible. Therefore no gas flow through the sample was achieved and equilibration was hindered. Hence, the temperature dependency of the mass loss may originate in diffusion limitation and adsorption / desorption of gaseous species.
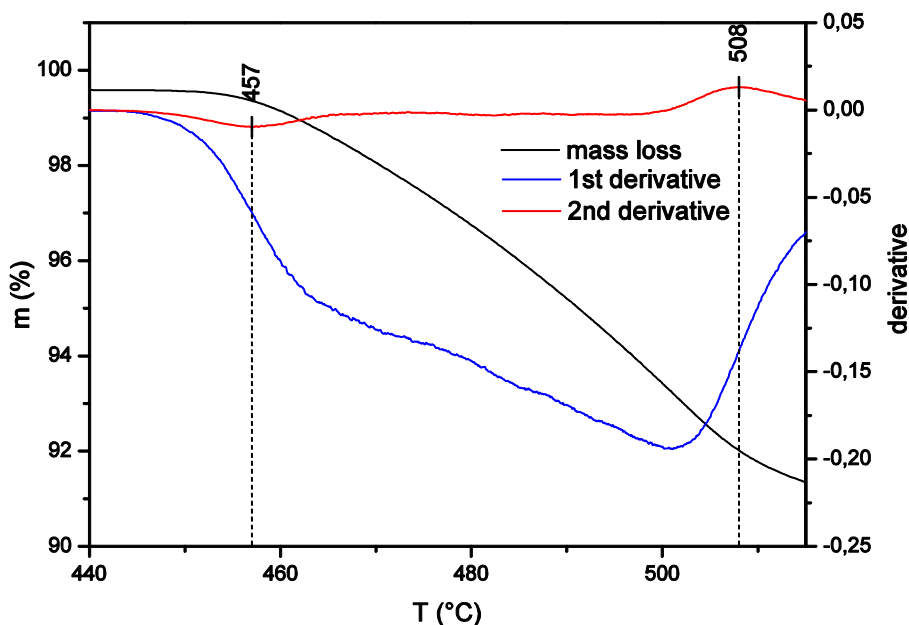
Figure 4-44: TGA of SiV56 in reaction gas. The first derivative (blue) indicates that several processes are overlapping. The second derivative (red) gives the inflection points of the mass loss with the strongest change which are used as reference points for the calculation of the stoichiometry.

Due to the complex reaction the onset point of reduction is deduced from the 2nd derivative of the mass loss as shown in Figure 4-44. The stoichiometry can be calculated using the mass loss. For this purpose two reference points are necessary and because all curves show the same shape (see Figure 4-42) the region T1 to T2 is chosen. It is assumed that the same processes are occurring in this temperature range. Furthermore, it is assumed that during reduction exclusively oxygen from vanadium pentoxide is taken and that it is present in the highest oxidation state 5+ at T1. Figure 4-45 depicts the change of T1 and stoichiometry as a function of vanadium pentoxide concentration.

At high concentration in region (I) the reduction already starts at 450 °C but the onset point shifts in region (II) to 480 °C. Vanadium pentoxide is present in the lowest stoichiometry at high loading. SiV56 has a composition of $V_2O_{3.25}$. When lowering the concentration the oxide releases smaller amounts of oxygen and the composition shifts in region (II) to $V_2O_{3.59}$ at $w = 13.74\,\%$ vanadium pentoxide but drops at $w = 7.2\,\%$ to $V_2O_{3.11}$. These results are summarized in Table 4-4.
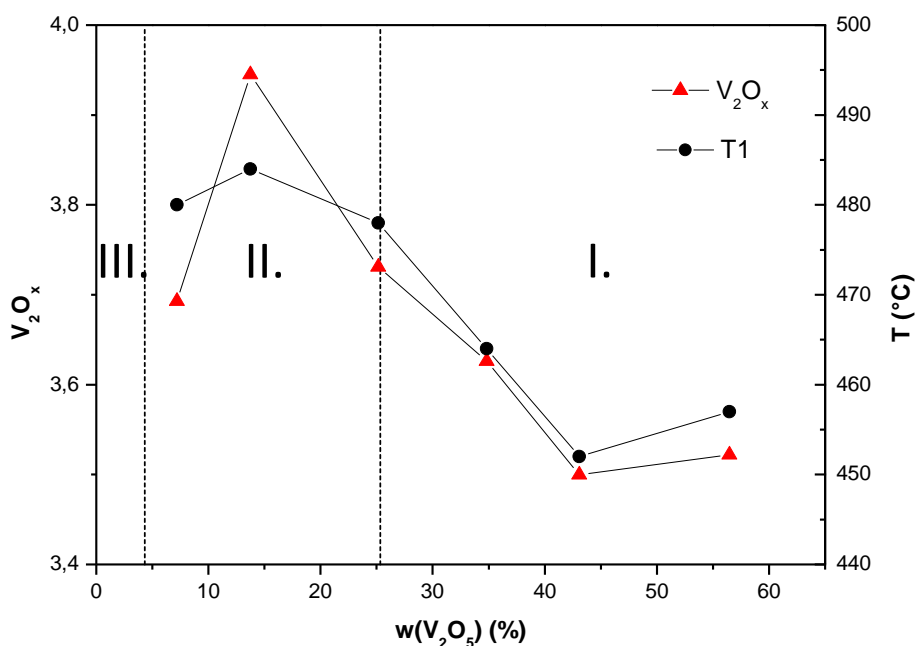
Figure 4-45: Change of the redox properties of VO_x/SiO_2 with concentration of V_2O_5 by TGA in reaction atmosphere

Table 4-4: TGA results of VO_x/SiO_2 catalysts. T1 is the reduction onset temperature and V_2O_x gives the stoichiometry of the VO_x phase. T2 is the reference temperature for the calculation of the stoichiometry. Δm is the mass loss in the range T1 – T2.

$w(V_2O_5)$ (%)	T1 (°C)	T2 (°C)	Δm (%)	V_2O_x
56.46	457	508	7.34151	3.25
43.07	452	510	5.68344	3.31
34.81	464	506	4.20714	3.37
25.16	478	512	2.80869	3.51
13.74	484	507	1.27486	3.59
7.20	480	504	0.82784	3.11

The change of the redox properties correlates with the transition from 3 dimensional crystalline V_2O_5 species in region (I) to 2 dimensional polymeric species in region (II). TPR experiments show different reduction behaviour of bulk V_2O_5 and polymeric VO_x species. Hydrogen TPR experiments usually exhibit a reduction peak of bulk like structures at higher temperature than 2-dimensinal structures [88]. However, the conditions of the experiments are different. The experiments in reaction gas involve reduction and reoxidation processes and therefore not only the reducibility influences the onset of mass loss. The change of

oxidation state in Figure 4-45 of the catalysts may be connected to its reoxidation capability. In Chapter 4.1.3.1 it was shown that a transition from electronic to ionic transport occurs from region (I) to (II). Therefore oxygen ions may readily migrate through the interface region and enhance the reoxidation kinetics. Hence, the final oxidation state in region (II) may be higher. The inverse trend observed for the lowest concentration may arise due to experimental error but needs further investigation. Other compounds like hydroxides or carbonates may also decompose and increase the observed weight loss. This would be a very small amount and thus negligible at high vanadium pentoxide concentrations - but significant at the lowest. Because all the mass loss is attributed to vanadia the calculation would yield a lower oxidation state.

Thus a change of redox and transport properties discussed in this chapter may arise due to the transition of bulk structures to 2-dimensional VO_x interface structures.

4.1.4. Amorphous Monolayer Catalysts

The catalysts investigated in this chapter consist of high surface area supports that comprise highly dispersed VO_x species. It was verified by UV-vis and other methods that these compounds exhibit only 2 dimensional VO_x structures and no bulk V_2O_5 [89]. Following samples were characterized: VO_x/γ-Al_2O_3, VO_x/m-ZrO_2 and VO_x/TiO_2.

4.1.4.1. Modelling of the Impedance Spectra

The conductivity of the catalysts was investigated in oxygen and nitrogen. The Nyquist plots exhibit atmosphere dependent differences that are discussed in this chapter.

Zirconia Supported Vanadium Oxide Catalysts

Figure 4-46 depicts the Nyquist plots of the m-ZrO_2 supported catalyst. The spectra show in oxygen (a) and nitrogen (b) substantial differences.
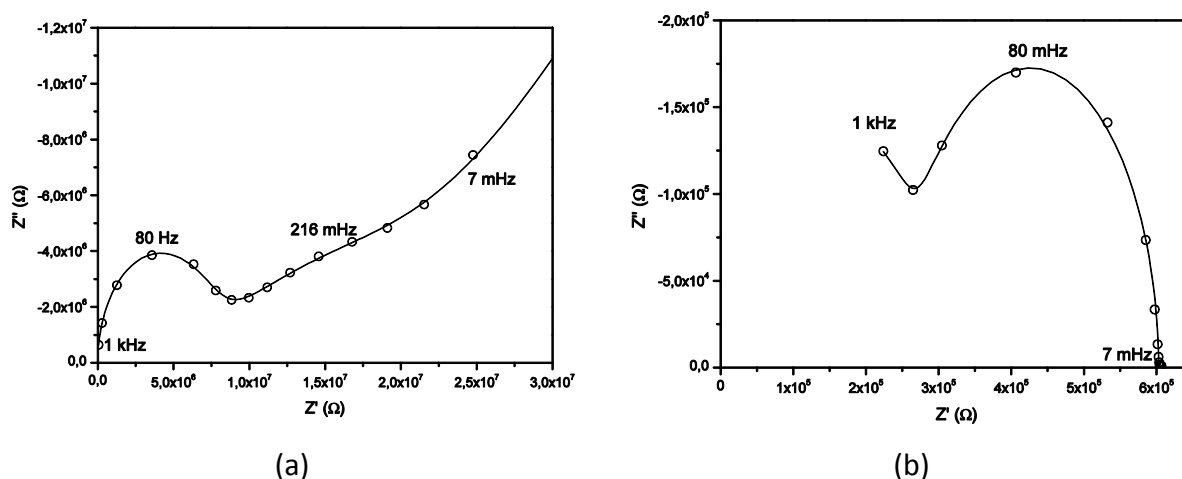
Figure 4-46: Nyquist plots of $VO_x/m\text{-}ZrO_2$ catalysts at 500 °C in (a) oxygen and (b) nitrogen.

In oxygen the spectrum consists of a high and low frequency arc and shows at very low frequency (down to 7 mHz) a 45° slope. The high frequency arc exhibits a capacity of $4.39*10^{-10}$ F and is thus attributed to the bulk relaxation (see Appendix: Table 7-1 on page 110). The low frequency arc shows with characteristic grain boundary behaviour (capacity of $8.23*10^{-8}$ F) and the spike at the lowest frequency exhibits a capacity of $4.44*10^{-7}$ F and shows additionally with the CPE exponent m equal to 0.49 Warburg diffusion characteristics. Therefore this is the electrode reaction [67]. In nitrogen the low frequency spike vanishes and the resistance is lowered. The high frequency relaxation is not completely resolved but is with $4.59*10^{-10}$ F the bulk relaxation. The well developed low frequency arc exhibits a grain boundary capacity of $7.17*10^{-9}$ F.

γ-Alumina Supported Vanadium Oxide Catalysts

Figure 4-47 displays the Nyquist plots for the γ-alumina supported catalyst. In oxygen two semi circles are evident and at very low frequency the onset of a small spike. The relaxation at about 22 Hz exhibits a bulk capacity of $2.45*10^{-10} \pm 1.54*10^{-11}$ F. At 1 Hz the grain boundaries yield a characteristic value of $5.53*10^{-9} \pm 1.48*10^{-10}$ F (Appendix: Table 7-2 on page 110). The spike at low frequency is too small to be fitted accurately but is most likely the electrode reaction. In nitrogen the two relaxations overlap but still contributions of the bulk and grain boundary process are evident.

(a)   (b)
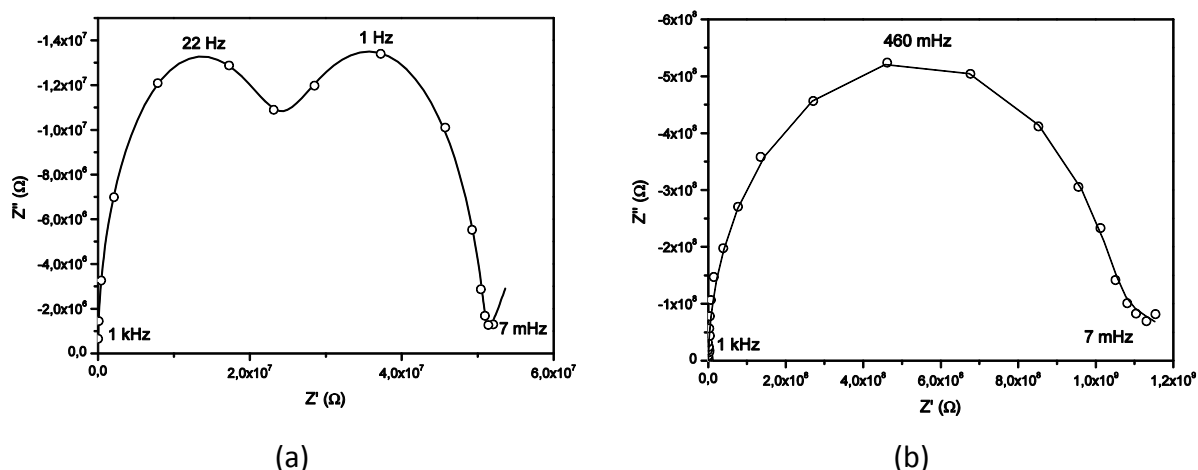
Figure 4-47:   Nyquist plots of VOx/γ-Al2O3 catalysts at 500 °C in (a) oxygen and (b) nitrogen.

Titania Supported Vanadium Oxide Catalysts

Like the other catalysts the titania supported compounds exhibit well resolved arcs in oxygen. At high frequency the bulk, then at 4 Hz the grain boundary, and at low frequency the electrode reaction is observed. They all show the expected capacities ($3.09*10^{-10}$ and $4.89*10^{-8}$ F) (Appendix: Table 7-3 on page 111). In nitrogen the bulk semi circle remains but no grain boundary relaxation is found.

(a)   (b)
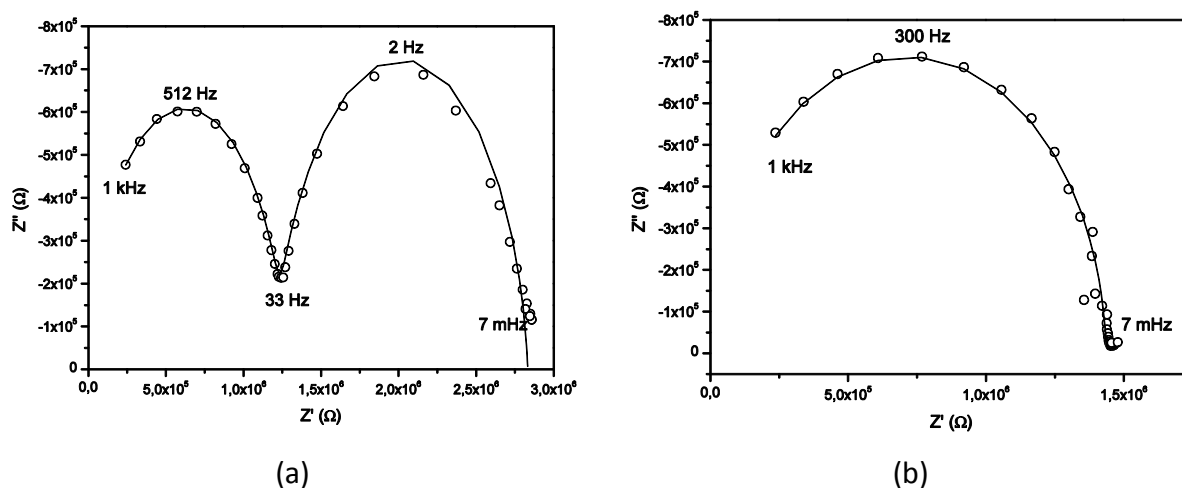
Figure 4-48:   Nyquist plots of VOx/TiO$_2$ catalysts at 500 °C in (a) oxygen and (b) nitrogen.

Influence of Partial Pressure

The electrical properties and impedance spectra may change due to the interaction of oxygen with the electrodes and grain surfaces. Due to adsorption of oxygen at the electrode a space charge layer may evolve that can increase the blocking effect of the metal. Similar effects are created by the grain boundary relaxations. Oxygen adsorbs at the surface layer binding electrons from the conduction band and thus creating a depletion layer. This space

71

charge zone at the grain boundary leads to a capacitive behaviour in the impedance spectra and is an oxygen pressure dependent barrier for negative charge carriers [90] (Figure 4-49).
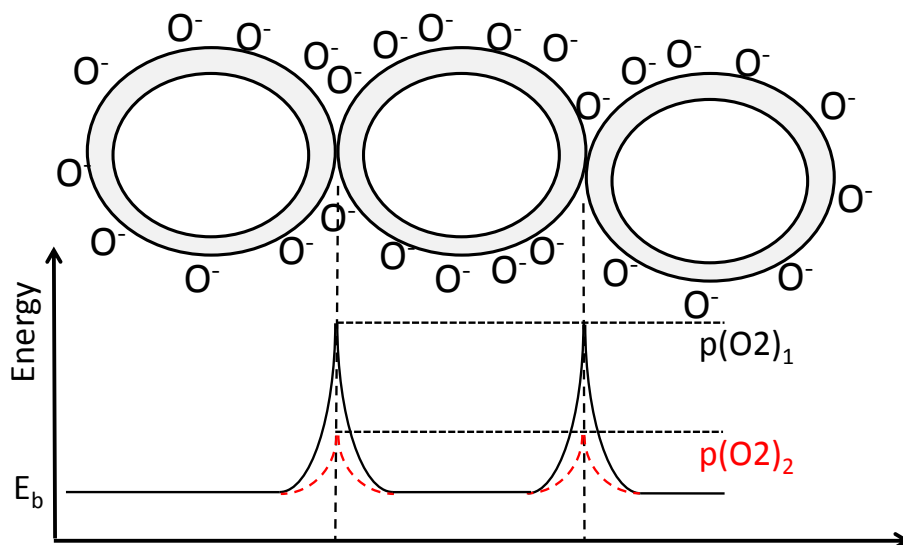
Figure 4-49: **Bulk electrons are drawn to the surface layer due to adsorption of oxygen. Electrons deplete at the boundary and a space charge region (grey) compensates the local deviation from charge neutrality. This layer blocks negative charge carriers (higher potential barrier at $p(O2)_1$) and causes a grain boundary relaxation in the impedance plot. At lower oxygen partial pressure less oxygen is adsorbed and thus the potential barrier is accordingly lowered ($p(O2)_2$). Hence the grain boundary relaxation may vanish. [90]**

4.1.4.2. Hysteresis Characteristics

The temperature dependent bulk conductivity exhibits different hysteresis characteristics that may not yield the defect formation enthalpy. For the discussion of the extent of the hysteresis, the factor Δh^* is used. This is also calculated according to equation (4-6) but does not represent the defect formation enthalpy.

Zirconia Supported Vanadium Oxide Catalysts

Conductivity experiments as performed in Chapter 4.1.1 to 4.1.3 were done using the highly dispersed VO_x catalysts. Figure 4-50 and Figure 4-51 depict the temperature dependency of the conductivity for $VO_x/m\text{-}ZrO_2$ in oxygen and nitrogen.
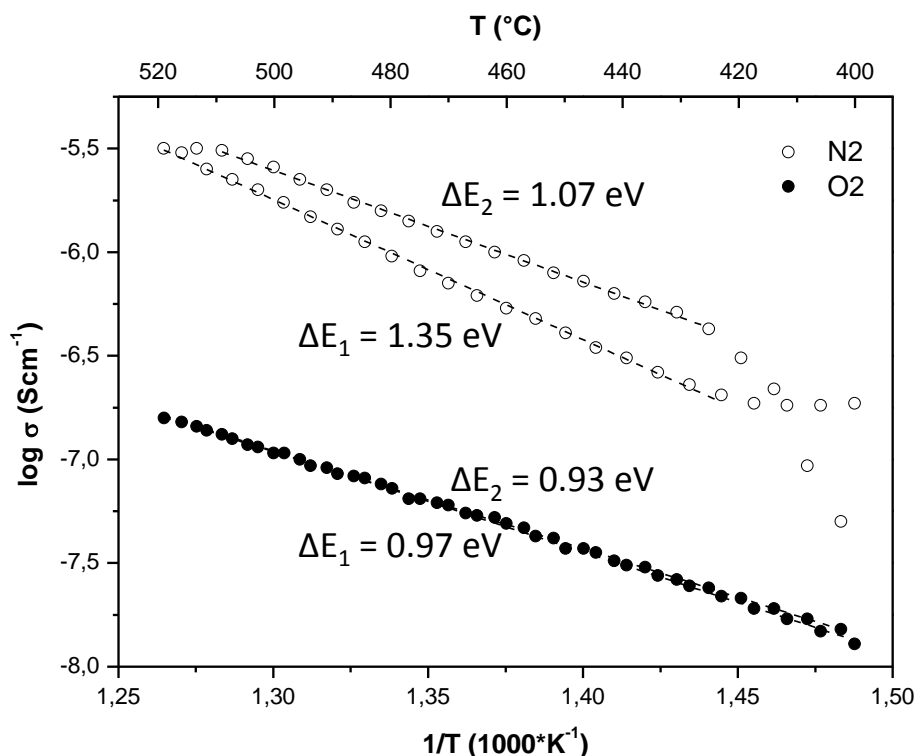
Figure 4-50: Arrhenius plots of monolayer catalyst VO$_x$/m-ZrO$_2$ in O$_2$ and N$_2$ at 0.1 K/min. ΔE$_1$ is the activation energy on heating, ΔE$_2$ is the activation energy on cooling.

VO$_x$/m-ZrO$_2$ in oxygen exhibits virtually no hysteresis on heating and cooling. The activation energies ΔE$_1$ = 0.97 eV and ΔE$_2$ = 0.93 eV are nearly equal and thus yield a small value of Δh* = 0.12 ± 0.06 eV. On lowering the oxygen partial pressure to pure N$_2$ the conductivity rises on heating from 7.2*10^{-6} to 2.0*10^{-6} Scm^{-1} at 500 °C. On cooling the hysteresis behaviour of the conductivity appears. The activation energy on heating changes to ΔE$_1$ = 1.35 eV and on cooling to ΔE$_2$ = 1.07 eV. Δh* rises to 0.84 ± 0.06 eV.

Table 4-5: Activation energies of VO$_x$/m-ZrO$_2$ on heating ΔE$_1$ and cooling ΔE$_2$ for oxygen and nitrogen. As a descriptor for the intensity of the hysteresis, the difference (Δh*) according to the calculation of the defect formation enthalpy is given: (ΔE$_1$-ΔE$_2$)*3.

	Gas	ΔE$_1$	ΔE$_2$	Δh*
VO$_x$/m-ZrO$_2$	O$_2$	0.97 ± 0.01	0.93 ± 0.01	0.12 ± 0.06
VO$_x$/m-ZrO$_2$	N$_2$	1.35 ± 0.01	1.07 ± 0.01	0.84 ± 0.06

γ-Alumina Supported Vanadium Oxide Catalysts

Figure 4-51 depicts the Arrhenius-plot of VO$_x$/γ-Al$_2$O$_3$ in oxygen and nitrogen. It shows similar behaviour, but already in oxygen a small hysteresis with Δh* = 0.51 ± 0.06 eV is visible. Activation energies on heating and cooling are ΔE$_1$ = 1.25 and ΔE$_2$ = 1.08 eV,

respectively. In nitrogen at 500 °C the conductivity drops from $3.1*10^{-7}$ in oxygen to $1.2*10^{-9}$ Scm^{-1} and the hysteresis is stronger. ΔE_1 on heating rises to 1.37 eV and ΔE_2 on cooling is lowered to 0.98 eV. Hence, Δh^* has more than doubled to 1.2 ± 0.1 eV. The activation energies are summarized in Table 4-6.
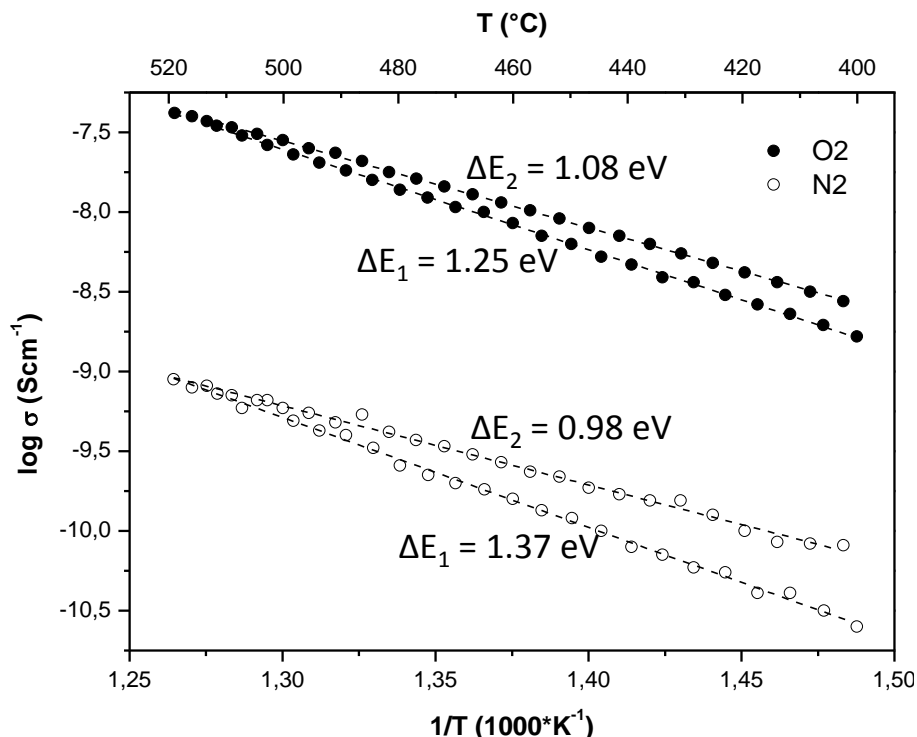
Figure 4-51: **Arrhenius plots of monolayer catalyst VO_x/γ-Al_2O_3 in O_2 and N_2 at 0.1 K/min. ΔE_1 is the activation energy on heating, ΔE_2 is the activation energy on cooling.**

Table 4-6: **Activation energies of VO_x/γ-Al_2O_3 on heating ΔE_1 and cooling ΔE_2 for oxygen and nitrogen. As a descriptor for the intensity of the hysteresis, the difference (Δh^*) according to the calculation of the defect formation enthalpy is given: $(\Delta E_1-\Delta E_2)*3$.**

	Gas	ΔE_1	ΔE_2	Δh^*
VO_x/γ-Al_2O_3	O_2	1.25 ± 0.01	1.08 ± 0.01	0.51 ± 0.06
VO_x/γ-Al_2O_3	N_2	1.37 ± 0.02	0.98 ± 0.02	1.2 ± 0.1

Titania Supported Vanadium Oxide Catalysts

Figure 4-52 shows the Arrhenius plots for VO_x/TiO_2 in oxygen and nitrogen at a heating rate of 0.1 K/min.
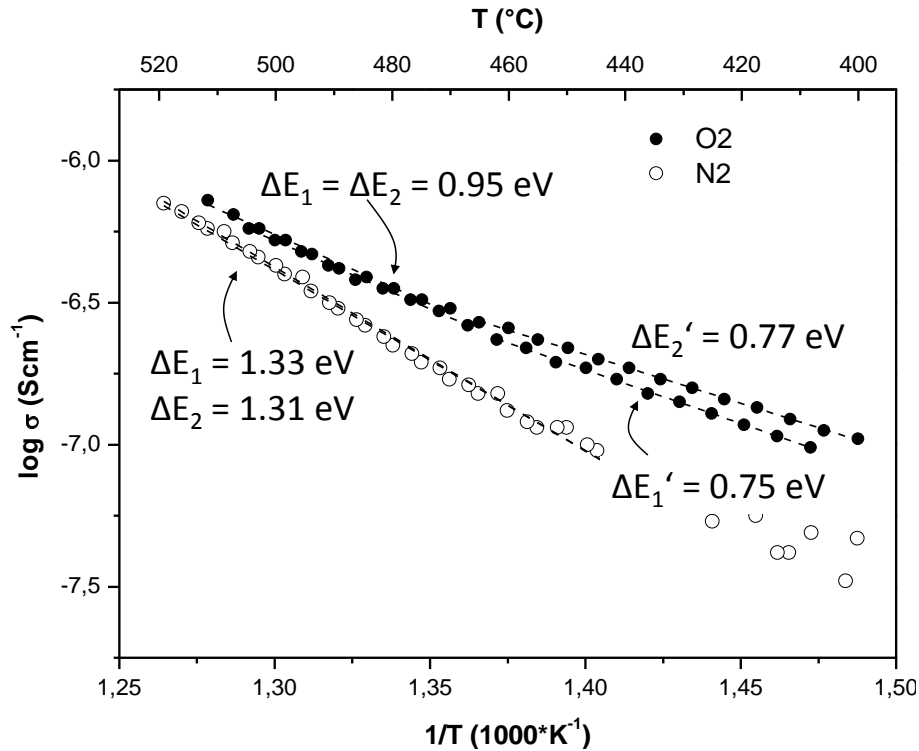
Figure 4-52: Arrhenius plot for VO$_x$/TiO$_2$ monolayer catalyst in O$_2$ and N$_2$ at 0.1 K/min. ΔE_1 is the activation energy on heating, ΔE_2 is the activation energy on cooling

In oxygen a low temperature region (400 – 460 °C) on heating and cooling is visible. On heating an activation energy of $\Delta E_1' = 0.77$ eV and on cooling $\Delta E_2' = 0.75$ eV is found. Above 460 °C a transition to higher activation energy is found (0.95 eV) exhibiting no hysteresis behaviour. In nitrogen the low temperature region vanishes and the activation energy shifts to $\Delta E_1 = 1.33$ eV on heating and $\Delta E_2 = 1.31$ eV cooling. This yields virtually no hysteresis with $\Delta h^* = 0.1 \pm 0.1$ eV. The conductivity at 500 °C exhibits a low partial pressure dependency and rises from 5.7×10^{-7} to 6.4×10^{-7} Scm^{-1} in nitrogen atmosphere.

In order to investigate the influence of reaction kinetics experiments were done at a higher cooling rate. In Figure 4-53 the conductivity in nitrogen with a heating rate of 0.1 K/min and cooling rate of 1 K/min is displayed. For comparison it is shown together with the experiment in nitrogen described in Figure 4-52.
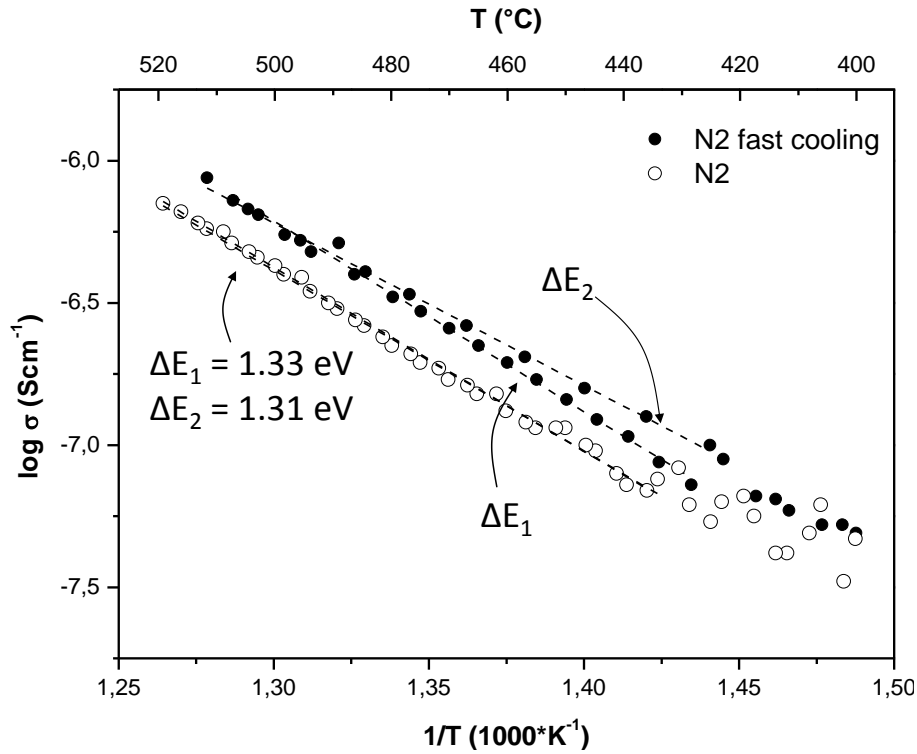
Figure 4-53: **Arrhenius plot for VO$_x$/TiO$_2$ monolayer catalyst in N$_2$ at 0.1 K/min and N$_2$ at 0.1 K/min on heating and 1 K/min on cooling. ΔE$_1$ is the activation energy on heating, ΔE$_2$ is the activation energy on cooling**

With a faster cooling rate the activation energy on heating stays constant but on cooling is lowered and a hysteresis appears. In order to investigate this behaviour, the sample was cycled 3 times (Table 4-7). In the 1st cycle ΔE$_1$ = 1.28 eV on heating and ΔE$_2$ = 1.13 eV on cooling is found. This hysteresis is characterized by Δh* = 0.5 ± 0.1 eV. For the 2nd cycle ΔE$_1$ = 1.34 eV and ΔE$_2$ = 1.10 eV is determined and Δh* = 0.7 ± 0.1 eV. In the 3rd cycle the hysteresis disappears and the activation energies are lowered to ΔE$_1$ = 1.23 eV and ΔE$_2$ = 1.21 eV and thus shows with Δh* = 0.1 ± 0.1 eV no hysteresis.

Table 4-7: Activation energies for VO_x/TiO_2 on heating (ΔE_1) and cooling (ΔE_2) for oxygen and nitrogen and for different heating rates (in $Kmin^{-1}$) and cycles. As a descriptor for the intensity of the hysteresis, the difference (Δh^*) according to the calculation of the defect formation enthalpy is given: $(\Delta E_1 - \Delta E_2)^*3$.

No.	Gas	Heating rate	Cooling rate	Cycle	ΔE_1	ΔE_2	Δh^*
1	O_2	0.1	0.1	1	0.95 ± 0.01	0.95 ± 0.01	0.00 ± 0.06
2	N_2	0.1	0.1	1	1.33 ± 0.01	1.31 ± 0.02	0.1 ± 0.1
3	N_2	0.1	1.0	1	1.28 ± 0.02	1.13 ± 0.02	0.5 ± 0.1
4	N_2	0.1	1.0	2	1.34 ± 0.02	1.10 ± 0.02	0.7 ± 0.1
5	N_2	0.1	1.0	3	1.23 ± 0.02	1.21 ± 0.02	0.1 ± 0.1

4.1.4.3. Defect formation

All the amorphous monolayer catalysts exhibit hysteresis characteristics that deviate from the behaviour of the crystalline samples. They need lower oxygen pressure for the development of a hysteresis and in the case of VO_x/TiO_2, additionally, a faster cooling rate is necessary.

In [60,61,62,63,64] redox properties of vanadia-based mixed oxides and supported catalysts were investigated using coulometric titration. It was found that the bulk oxides exhibit lower oxygen partial pressures for the onset of defect formation than pure vanadium pentoxide (Table 4-8):

Table 4-8: Oxygen partial pressure pO_2 (bar) for the onset of reduction in mixed vanadium bulk oxides determined by coulometric titration [61].

Mixed Oxide	$CeVO_4$	$Mg_3(VO_4)_2$	$AlVO_4$	V_2O_5
pO_2	10^{-22}	10^{-15}	10^{-7}	10^{-6}

This is in agreement with the partial pressure dependent hysteresis characteristics and with the increase of the activation energy on heating in nitrogen.

γ-Alumina Supported Vanadium Oxide Catalysts

$VO_x/\gamma-Al_2O_3$ (Figure 4-51) exhibits in O_2 a less pronounced hysteresis than in N_2. This indicates that vacancy formation on heating in oxygen is impeded. This in agreement with literature data for $AlVO_4$ bulk oxide (Table 4-8) that shows compared to V_2O_5 a lower oxygen

pressure for onset of reduction. Therefore in nitrogen defects readily are formed and no reoxidation on cooling is possible. The calculated defect formation enthalpy is $\Delta H_f = 1.2 \pm 0.1$ eV.

Zirconia Supported Vanadium Oxide Catalysts

This characteristic is also observed for $VO_x/m\text{-}ZrO_2$ - but even more distinct. In oxygen no lattice oxygen is released and thus no hysteresis of the conductivity is observed. Hence, even lower oxygen pressure is necessary. Therefore the activation energy on heating and cooling of $\Delta E_m = \Delta E_1' = 0.97$ eV and $\Delta E_m = \Delta E_2' = 0.93$ eV is ascribed to the migration of ionic charge carriers. In nitrogen the activation energy on heating rises and the hysteresis appears. The migration energy in nitrogen is close to that in oxygen with $\Delta E_m = \Delta E_2 = 1.07$ eV and therefore evidences the assumption above. Using the apparent activation energy of $\Delta E^* = \Delta E_1 = 1.35$ eV a defect formation enthalpy of $\Delta H_f = 0.84 \pm 0.06$ eV is calculated. This is very close to the values determined in Chapter 4.1.2 on polycrystalline samples of high loading (0.9 ± 0.1 eV) and in Chapter 4.1.3.2 at the interface region (0.7 ± 0.1 eV).

Titania Supported Vanadium Oxide Catalysts

Similar results are found for VO_x/TiO_2. In oxygen above 460 °C a migration energy for ions of $\Delta E_m = \Delta E_1 = 0.95$ eV is found and no defects are formed. In nitrogen the activation energy rises to $\Delta E^* = \Delta E_1 = 1.33$ eV (see Table 4-7) on heating and indicates an additional contribution due to defect formation. These findings are again in agreement with the lowered oxygen partial pressure – compared to V_2O_5 – for the onset of defect formation as found in [61] (Table 4-8). But on cooling this activation energy prevails ($\Delta E^* = \Delta E_1 = 1.31$ eV) and additionally no hysteresis is found. This might be due to reoxidation of vanadium pentoxide by the titania support as indicated by EPR experiments [91]. But the migration energy can be obtained by rapid cooling and thus freezing the defects as done in Figure 4-53. The hypothesis of reoxidation by titania is supported by the hysteresis characteristics in the cycling experiments. The second cycle still shows a hysteresis but in the third run the oxygen supply is depleted and no further defects are formed. Therefore the defect formation enthalpy is calculated using the average values of all apparent and migration energies which yields a value of $\Delta H_f = 0.44 \pm 0.1$ eV.

The defect formation enthalpies are summarized in Table 4-9.

Table 4-9: Defect formation enthalpies and activation energies for the supported monolayer catalysts. All values are in eV.

	ΔE^*	ΔE_m	ΔH_f
VO_x/TiO_2	1.32 ± 0.02	1.17 ± 0.02	0.45 ± 0.1
$VO_x/m\text{-}ZrO_2$	1.35 ± 0.01	1.07 ± 0.01	0.84 ± 0.06
$VO_x/\gamma\text{-}Al_2O_3$	1.37 ± 0.02	0.98 ± 0.02	1.2 ± 0.1

4.1.4.4. Transport Mechanism

As found in the percolation experiments the amorphous monolayer catalysts show ionic and electronic partial conductivities.

Electronic conduction

The observed changes on lowering the oxygen partial pressure indicate different partial electronic contributions. $VO_x/m\text{-}ZrO_2$ exhibits an increase in conductivity in N_2 atmosphere. This shows clearly n-type semiconducting properties at low pO_2. With a drop of conductivity in N_2 substantial p-type contribution is found for $VO_x/\gamma\text{-}Al_2O_3$ most likely dominating at high partial pressure. VO_x/TiO_2 exhibits only a small change but n-type conductivity. These findings are supported by the reoxidation experiments in the following chapter that clearly show the discussed electronic contributions.

Ionic conduction

Migration energies of about 1 eV are found as shown in the percolation experiments in previous chapters (Chapter 4.1.3, page 57) indicating similar ionic transport at the interface. Further evidence is given by the electrode reaction in the impedance plots. VO_x/TiO_2 shows in O_2 a low temperature region with a lowered migration energy $\Delta E_m = 0.77$ eV. Thus a transition from cationic to anionic conduction may occur at 460 °C in O_2.

4.1.4.5. Reoxidation Behaviour

In order to investigate the reoxidation behaviour conductivity relaxation experiments were done. The oxygen partial pressure was rapidly changed from 10^{-4} to 1 bar and the impedance spectra were recorded. On raising the partial pressure a decrease or increase of the conductivity is observe. The data is fitted using the exponential function:

$$\sigma = \sigma_0 + A \cdot \exp(rt) \tag{4-8}$$

σ is the conductivity at time t, σ_0 is the conductivity at t = 0 s, A is the pre-exponential factor and r the rate constant.

Zirconia Supported Vanadium Oxide Catalysts

Figure 4-54 depicts the conductivity relaxation behaviour of $VO_x/m\text{-}ZrO_2$:

Figure 4-54: **Conductivity relaxation experiments of $VO_x/m\text{-}ZrO_2$ from $1.04*10^{-4}$ to 1 bar O_2. The data is fitted using an exponential function.**

The calculated rate constant for $VO_x/m\text{-}ZrO_2$ is r = $-3.20*10^{-4}$ s^{-1}.

γ-Alumina Supported Vanadium Oxide Catalysts

The conductivity relaxation experiment (Figure 4-55) shows, that an increase of the oxygen partial pressure yields a higher conductivity. The fit gave a reoxidation rate of $-2.48*10^{-4}$ s^{-1}.
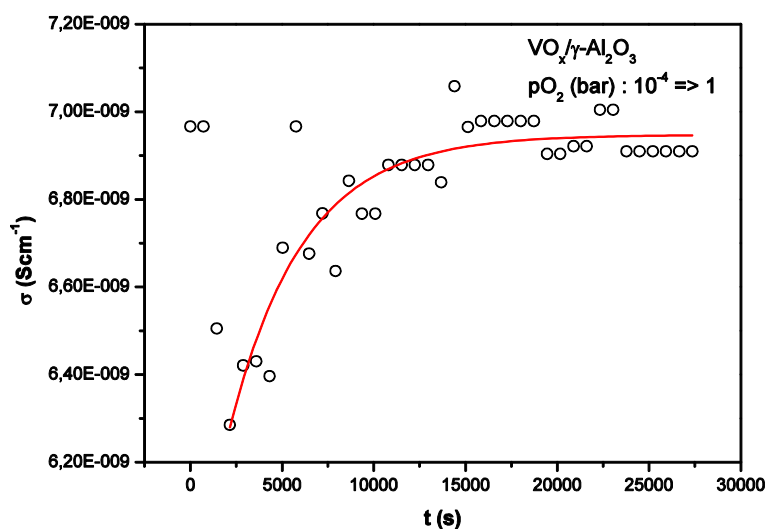
Figure 4-55: **Conductivity relaxation experiments of $VO_x/\gamma\text{-}Al_2O_3$ from $1.04*10^{-4}$ to 1 bar O_2. The data is fitted using an exponential function.**

VO$_x$/TiO$_2$

On increasing the oxygen partial pressure the conductivity shows n-type behaviour and drops. The rate for equilibration is found to be -1.04*10^{-3} s^{-1}.
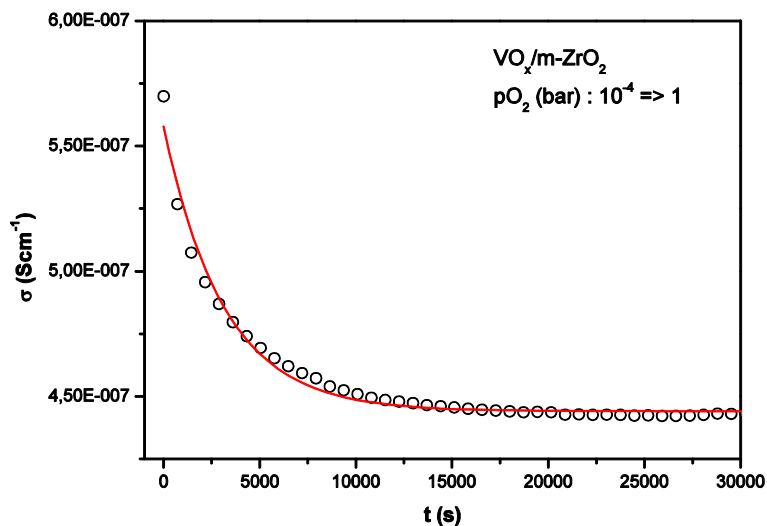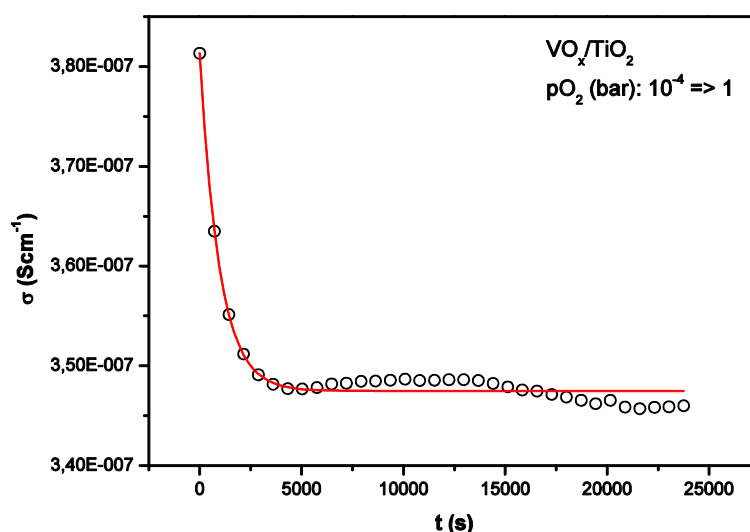

Figure 4-56: **Conductivity relaxation experiments of VO$_x$/TiO$_2$ from 1.04*10^{-4} to 1 bar O$_2$. The data is fitted using an exponential function.**

The calculated rate constants for the reoxidation process are shown in Table 4-10.

Table 4-10: **Reoxidation kinetics of VO$_x$/m-ZrO$_2$, VO$_x$/TiO$_2$ and VO$_x$/γ-Al$_2$O$_3$ from 1.04*10^{-4} to 1 bar O$_2$ derived from the exponential fit. The rate r is in s^{-1}.**

sample	r	error	R^2
VO$_x$/TiO$_2$	-1.04*10^{-3}	6.01*10^{-5}	0.97751
VO$_x$/m-ZrO$_2$	-3.20*10^{-4}	1.30*10^{-5}	0.98377
VO$_x$/γ-Al$_2$O$_3$	-2.48*10^{-4}	4.39*10^{-5}	0.81627

The conductivity relaxation experiments have shown different reoxidation kinetics for the catalysts. Following sequence is found:

$$r(VO_x/TiO_2) > r(VO_x/m\text{-}ZrO_2) > r(VO_x/\gamma\text{-}Al_2O_3) \qquad \text{4-9}$$

Furthermore, VO$_x$/TiO$_2$ exhibits a rate that is nearly 1 order of magnitude higher than for the other compounds (Table 4-10). Due to the closed porous structure of the pellets the rate will probably be controlled by two mechanisms: oxygen diffusion in the solid and oxygen surface exchange within the pore volume. However, this rate shows, that the samples with the

fastest rate constant exhibit also the highest rate constant for the ODH [89] stressing the importance of the exchange reaction and defect formation.

4.2. Origin of Enhanced Transport Properties

In the previous chapters I have shown, that the supporting metal oxides change the conduction mechanism of vanadium pentoxide from electronic to ionic and that the defect formation properties are influenced. The enhancement of ionic conductivity in a 2 phase mixture can have several origins. The most obvious reason is a reaction of both compounds creating a better ion conducting phase. But also in the absence of a global phase transition strong interactions can lead to modified transport properties [92]:

1. The phase transition may restrict to the interface,

2. or due to 2-phase-interactions, like interfacial stress, higher-dimensional defects are formed (surfaces, dislocations, grain-boundaries, etc.) and hence yield a kinetic path with enhanced mobility.

3. Space charges may arise below the interface

4. and homogeneous bulk doping may occur.

A mechanism comprising option 1. or 2. creates entirely new kinetic paths and therefore the migration enthalpies are independent of the bulk value. Consequently 3. and 4. show migration enthalpies close to the original data.

4.2.1. Micro-Structural Investigation

Figure 7-2 and Figure 7-3 in the Appendix show the XRD pattern for the percolation samples. Only vanadium pentoxide and the support oxides are present and thus proof that no global phase transition is observed.

Neutron diffraction on supported catalysts comprising a mole fraction of 10 % V_2O_5 gave evidence for highly non-linear thermal expansion behaviour (Figure 4-57).
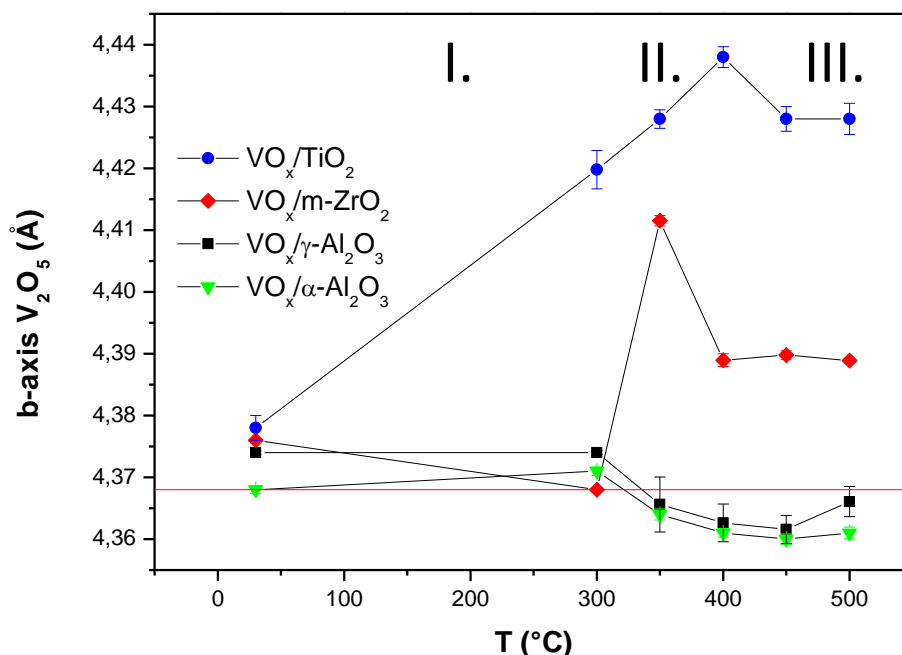
Figure 4-57: Temperature dependency of b-axis of 10 mol% V_2O_5 on different supports in oxygen. The red line indicates the theoretical lattice parameter of the b-axis. The expansion behaviour can roughly be divided into 3 domains: I. increase of strain, II. relaxation and III. stagnation.

The lattice parameters of vanadium pentoxide and support show that the interface support/VO_x results into lattice strains at 30 °C (Figure 4-58) and an increase with rising temperature is expected. On all supports, except for γ-Al_2O_3, vanadium pentoxide exhibits an expansion of the b-axis and compression in a-c direction. The active compound is strained in various degrees giving following ranking: TiO_2 > m-ZrO_2 > γ-Al_2O_3 > α-Al_2O_3. The supports show mainly compressed lattice parameters, except γ-Al_2O_3, which extends to small degrees in a-b direction. On heating the catalysts (Figure 4-57) the lattice shows anomalies in thermal expansion. The length of the vanadium pentoxide b-axis changes non-linearly and for all supports this behaviour can be divided into three regions. Region (I) extends up to 300 – 400 °C and is characterized by an increase or stagnation in b-axis lattice parameter. Region (II) shows at 300 – 400 °C a sudden drop followed by a nearly constant value in region (III).
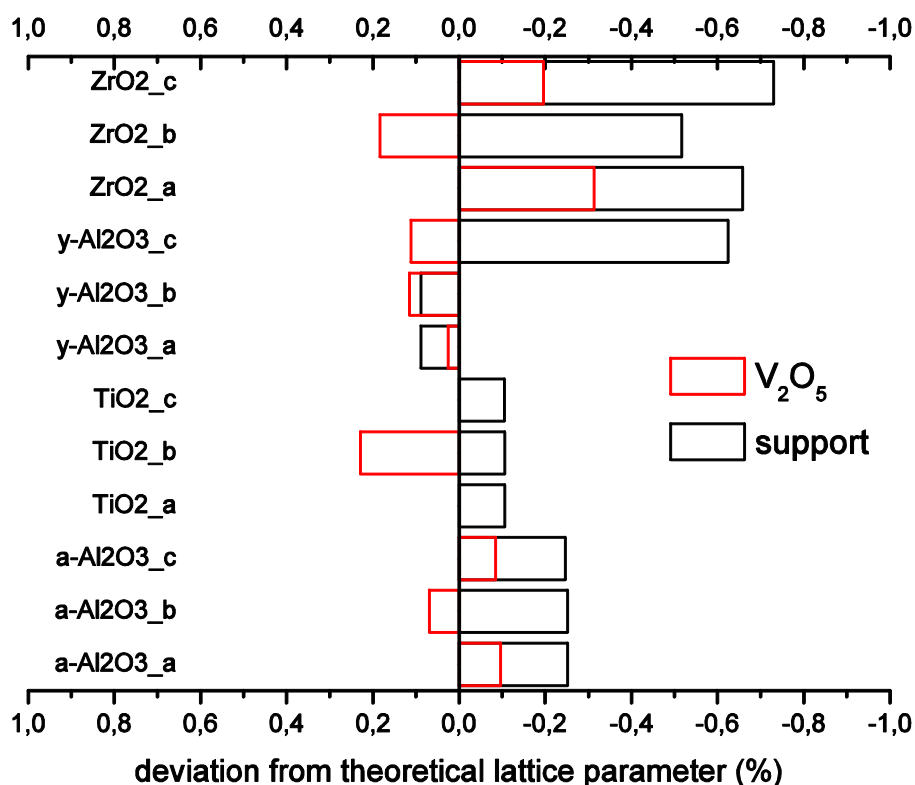
Figure 4-58: Deviation from theoretical lattice parameters of supported catalysts at 30 °C in oxygen. The V_2O_5 phase is depicted in red – the support in black.

On calcination at 500 °C an interface VO_x/support is formed due to an esterification reaction of the basic hydroxyl groups at the metal oxide surface [2]. At this temperature the system is stress free. The presence of an interface is supported by high resolution TEM images that show wetting of vanadium pentoxide on silica (Figure 4-60). The compounds exhibit different thermal expansion coefficients compared to V_2O_5 [93] which additionally expands strongly anisotropic. Therefore on cooling, support and active compound shrink to different extents. But due to the interface a strain hindrance is present and thermal stress results (Figure 4-59).
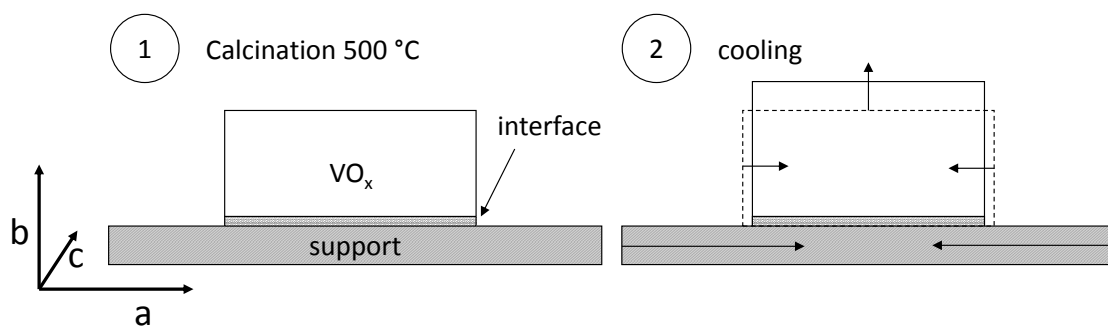
Figure 4-59: **Evolution of strain in supported catalysts. On calcinations an interface is formed (1). Vanadium pentoxide and support exhibit a thermal misfit and on cooling (2) the active compound is strained.**

Very large stress may develop even exceeding the yield stress of vanadium pentoxide and thus creating a defect rich nano-crystalline mosaic structure (Figure 4-60). When heating the powder samples (Figure 4-57) stress affects the thermal expansion due the interface structure.
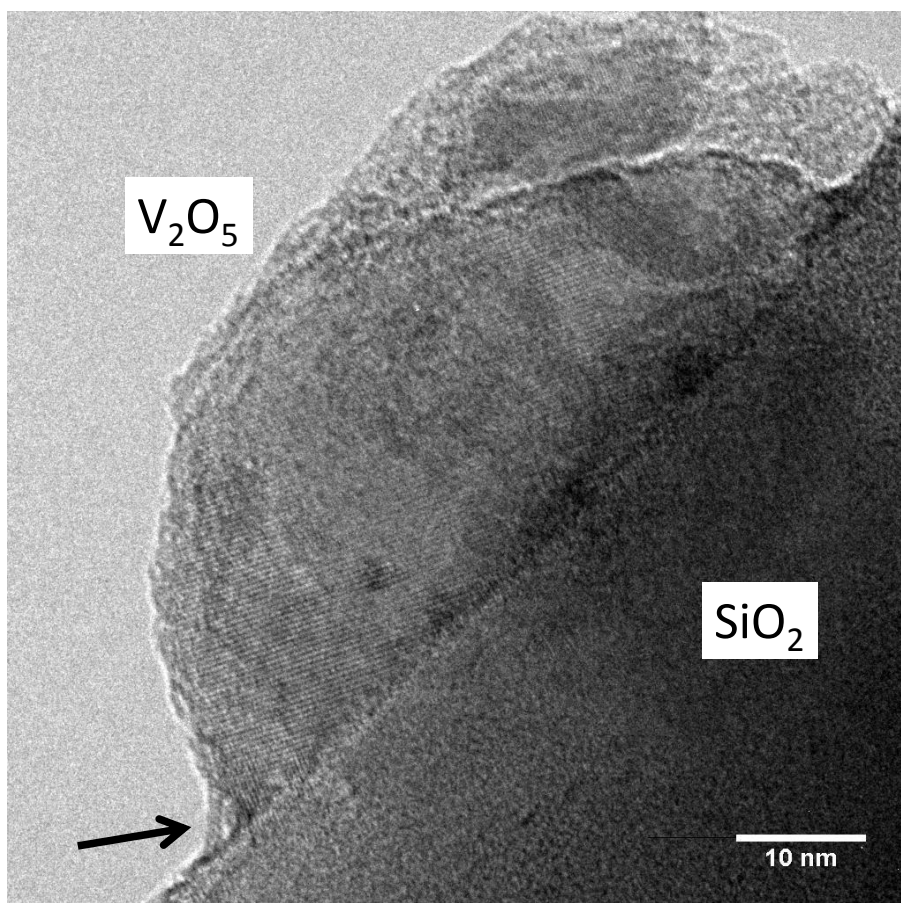
Figure 4-60: TEM micrograph of VO$_x$/SiO$_2$. The image shows the contact of vanadium pentoxide grain to the support. On calcinations wetting of vanadia is observed (arrow shows good wetting angle). Very small grains are present with a thickness of ca. 20 nm that exhibit a mosaic structure with ~5 nm grains in various orientations. Grains of this size exhibit a very high surface to volume ratio and show thus the enhanced diffusion properties of the surface.

Thus depending on the support different behaviour is observed. Interestingly, the supports that give the best catalysts (TiO$_2$ and m-ZrO$_2$) exhibit the strongest expansion of the b-axis in region I. Region II coincides with the onset of defect formation determined by conductivity experiments and shows a relaxation of the b-axis what is in agreement with calculated lattice relaxations on reduction [94] and partial pressure dependent XRD experiments discussed on page 41. The experiments indicate the formation of new grain boundaries (mosaic structure [95]) on calcination and cooling due to a thermal misfit. Therefore the transport properties can change due to the new microstructure but mechanical stress can itself alter the defect formation properties as discussed for ceria in [96,97,98,99,100] as chemical strain effect.

4.2.2. The Chemical Strain Effect

In the literature a connection between externally applied stress and defect interaction is discussed [96,98,100]. It is called the "chemical strain effect" and describes the conversion of elastic energy into chemical energy of point defects. This relaxation process requires a finite time to equilibrate and thus if a solid is strained fast enough, only linear elastic behaviour is observed. Therefore, the strain causes an unrelaxed stress, σ_{el}, with an elastic modulus E_{el}.

$$\sigma_{el} = E_{el} \cdot \varepsilon_{el} \qquad\qquad 4\text{-}10$$

This results into an elastic energy, U_{el}:

$$U_{el} = E_{el} \cdot 1/2 \left(\varepsilon_{el} \right)^2. \qquad\qquad 4\text{-}11$$

The elastic energy is the driving force for a reversible defect interaction reaction that results into a change of volume, β, and a change of defect concentration or other kind of defect interaction, ΔC. The strain caused by this interaction is the chemical strain ε_{ch}:

$$\varepsilon_{ch} = \beta \cdot \Delta C \qquad\qquad 4\text{-}12$$

Hence, a material may be able to partially compensate the applied mechanical strain by a thermodynamic relaxation process. This gives a relaxed strain, ε_{rel}:

$$\varepsilon_{rel} = \varepsilon_{el} - \varepsilon_{ch} \qquad\qquad 4\text{-}13$$

and with that a relaxed modulus E_{rel}:

$$\sigma_{rel} = E_{rel} \cdot \varepsilon_{rel}. \qquad\qquad 4\text{-}14$$

Hence, the elastic energy in the relaxed state is given by:

$$U_{el} = E_{rel} \cdot 1/2 \left(\varepsilon_{el} - \varepsilon_{ch} \right)^2. \qquad\qquad 4\text{-}15$$

Spontaneous release of mechanical stress yields therefore a sudden relaxation of elastic strain, but the chemical strain will decline over a period of time corresponding to the time constant of the defect reaction. The chemical strain is characterized by the stress-reduction factor, f, which is the ratio between the relaxed and unrelaxed modulus [99]:

$$f = \frac{E_{rel}}{E_{el}} < 1 \qquad\qquad 4\text{-}16$$

The chemical strain effect is often discussed for the defect complex association and dissociation reaction in gadolinium doped ceria [97,101,96,99,98]:

$$Gd'_{Ce} + V_O^{\bullet\bullet} \leftrightarrow \left[Gd_{Ce} V_O \right]^{\bullet}. \qquad\qquad 4\text{-}17$$

The pairing of defects leads to a decreased volume with $\beta > 15$ Å. Thus, extensive chemical relaxations are observed with stress-reduction factors of 0.07 [96]. Further interactions of point defects like:

- clustering
- and reduction/oxidation

are also discussed. The strain effect induced by reduction shows a volume change in the same order of magnitude as the defect association reaction. On reduction an oxygen vacancy and two electrons that are localized at two ceria sites are generated:

$$2Ce_{Ce}^{x} + O_{O}^{x} \xrightarrow{\text{reduction}} 2Ce_{Ce}^{'} + \bigcup_{O}^{\bullet\bullet} + 1/2\,O_2. \qquad\qquad 4\text{-}18$$

The oxygen vacancy exhibits a volume 16 % smaller than the oxygen ion [102] and the ionic radius of Ce^{3+} compared to Ce^{4+} is about 18 % larger. Therefore, the lattice parameter of micro-crystalline ceria increases linearly with increasing oxygen deficiency [101]. In [103] the influence on the volume change on reduction is investigated and it is found, that composition, crystal structure and doping change the resulting volume relaxation.

The chemical strain effect should also apply for other materials than doped ceria. These should exhibit large amounts of point defects ($> 10^{21}$ cm^{-3}), a substantial change in volume on interaction (a few Å³) and the rate constant for the reaction must be high enough to achieve equilibration within reasonable time [100,98]. Lubomirsky suggests in [99] that materials with a high tolerance for deviations from stoichiometry like V_2O_{5-x} may exhibit chemical strain due to oxidation or reduction.

Temperature has an important influence on the chemical strain effect, because mobile point defects are necessary and activation of the interaction reaction e. g. association or dissociation. The strain effect will be most distinct at medium temperature, because at high temperature the defect equilibrium shifts to mostly dissociated species. At low temperature the point defects will be mostly present as associated complexes and the strain effect will be negligible. [100]

It was found that materials exhibiting a strong chemical strain effect also show anomalies in thermal expansion [100]. Experiments on Gd-doped ceria show 2 thermal expansion domains. The first domain with linear expansion at high oxygen partial pressure and the

second exhibiting abnormal expansion at low pressure. This is attributed to chemical strain due to formation of oxygen vacancies at low pressure. Doping with gadolinium lowers the transition temperature because the oxygen bond is weakened [104]. Further evidence is given by Kossoy et al. [105]. They found for Gd-doped ceria a hysteresis of lattice parameters on heating and cooling that is caused by large concentrations of interacting point defects. On heating the complexes dissociated and recombine at low temperature. But the association process exhibits very slow kinetics.

Vanadium pentoxide exhibits a high potential for the chemical strain effect. It is highly redox active, shows very large anisotropic expansion, and volume relaxation effects on defect formation.

$$2V_V^x + O_O^x \leftrightarrow 2V_V^{'} + \cup_O^{\bullet\bullet} + 1/2O_2 \qquad \text{4-19}$$

Furthermore, the thermal expansion shows anomalies that indicate stress and strain influences (Figure 4-57) on the defect formation. Hence, interfacial stress might be the driving force for the enhanced oxygen release in the supported catalysts.

4.3. Impact on Catalysis

The conductivity experiments have shown a support effect on the defect formation enthalpy and moreover a change of electronic to ionic transport is observed. The impact of these effects on the catalytic reaction is discussed in this chapter.

The reaction in equation 4-20 shows the overall reaction for the ODH:

$$V^{4+}V^{4+}O + 1/2 O_2(g) + C_3H_8(g) \rightarrow V^{4+}V^{4+}O + H_2O(g) + C_3H_6(g) \qquad \text{4-20}$$
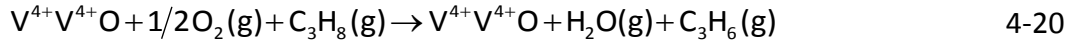
The educts are the reduced catalyst, oxygen and propane which react to water and propene. This is a multi step reaction and is discussed in the following. The catalyst for the ODH starts in the reduced state with 2 V^{4+} and the gas phase species oxygen and propane. The first step is the oxidation of the V^{4+}-centres followed by adsorption of propane (equation 4-21).

$$V^{4+}V^{4+}O \qquad \xleftarrow{\frac{1}{2}O_2} V^{5+}V^{5+}O_2 \qquad \text{4-21}$$

This is followed by the rate limiting hydrogen abstraction and vanadia reduction via the transition states TS1 and TS2 (equation 4-22).

$$\xleftarrow{C_3H_8} V^{4+}V^{4+}(OH)_2 - C_3H_6 \qquad \text{4-22}$$

The energy for reaching TS1 is the propane activation energy E_A but experimentally only the apparent activation energy $E_{A,app}$ is measured that includes the adsorption enthalpy ΔH_{ad}. Finally, in the last two steps the products propene and water desorb (equation 4-23) and the next cycle starts again with the oxidation.

$$\xleftarrow{-H_2O, C_3H_6} V^{4+}V^{4+}O + H_2O + C_3H_6 \qquad \text{4-23}$$
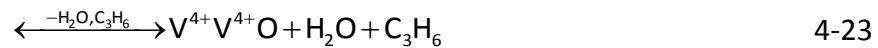
The overall energy difference from beginning to the end of the cycle gives the reaction enthalpy ΔH_R. The lower the reaction enthalpy the higher the reaction rate should be. Figure 4-61 depicts a reaction profile for the oxidative dehydrogenation from Beck et al. together with the elementary reaction steps [89].
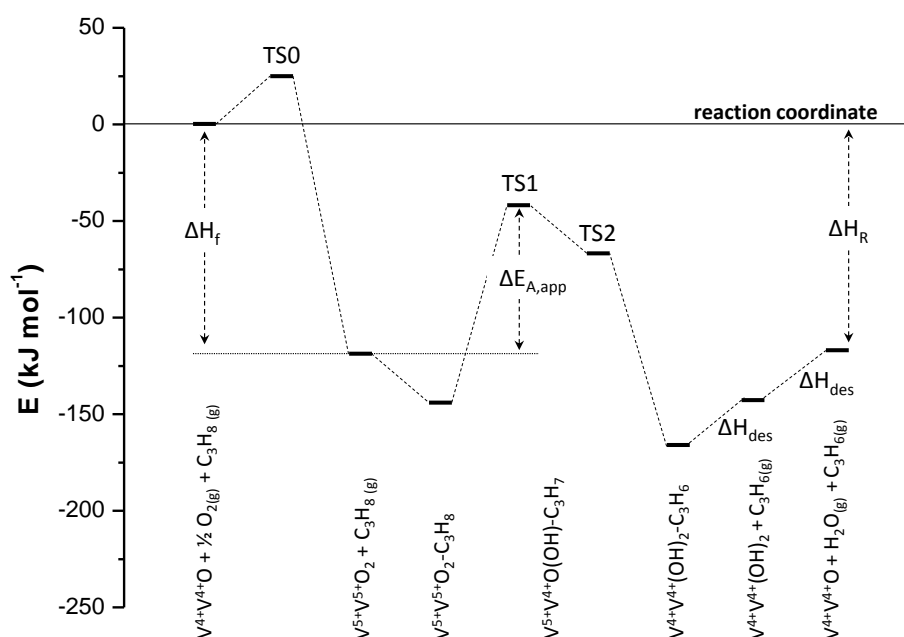
Figure 4-61: Energy reaction profile for the ODP on vanadium pentoxide. [89]

A connection to the solid state properties is made by the first oxidation step in equation 4-21 which corresponds to the back reaction of the oxygen vacancy formation investigated in previous chapters:

$$2V_V^x + O_O^x \xrightarrow{\text{reduction}} 2V_V' + \cup_O^{\bullet\bullet} + 1/2O_2. \qquad\qquad 4\text{-}24$$

4.3.1. Supported Catalysts at High Loading – Correlation to Catalytic Reaction

In order to correlate the defect formation enthalpies with catalytic properties catalytic tests were done in separate experiments. The propane activation energy was derived from an Arrhenius plot of propane conversion X(propane) and temperature. Figure 4-62 depicts this diagram together with the linear regression of the measured data.
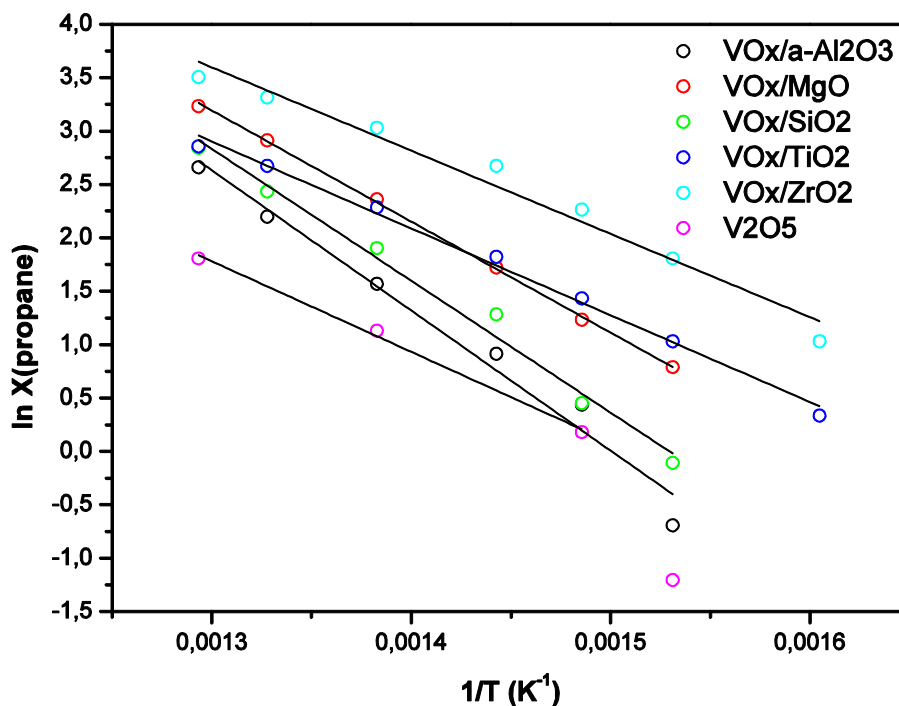
Figure 4-62: **Catalytic test results for the VO_x/M_xO_y. Calculation of the propane actiation energy E_a from an Arrhenius plot of propane conversion X(propane) vs. temperature.**

Different propane activation energies are found for each catalyst and are summarized in Table 4-3 on page 50. $VO_x/m\text{-}ZrO_2$ shows with 0.67 ± 0.05 eV the lowest activation energy followed by VO_x/TiO_2 and V_2O_5 with 0.70 ± 0.02 and 0.73 ± 0.04 eV, respectively. VO_x/MgO exhibits a value of 0.90 ± 0.01 eV for propane activation. The highest activation energies are found for the catalyst VO_x/SiO_2 and $VO_x/\alpha\text{-}Al_2O_3$ (1.06 ± 0.06 and 1.13 ± 0.09 eV).

In order to investigate the impact of defect formation on the catalytic reaction the Brönsted-Evans-Polanyi (BEP) relation was used, that correlates the activation energy and the most important thermodynamic property in the system. For different surface reactions on transition metal surfaces linear relations between e.g. activation energies and reaction energies are found [106]. The correlation plot for the apparent propane activation energy and the defect formation enthalpy is shown in Figure 4-63. It is evident, despite of the strong scatter, that the catalysts exhibiting a small defect formation enthalpy also show low propane activation energies and thus show BEP behaviour.
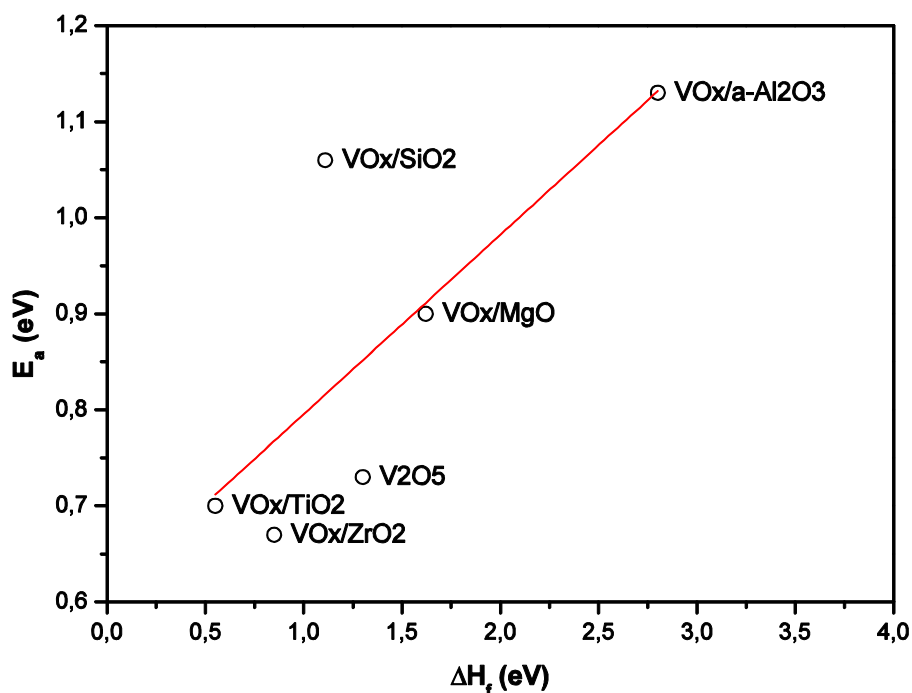
Figure 4-63: **Brönsted-Evans-Polanyi relation of the apparent propane activation energy E_a and defect formation enthalpy ΔH_f.**

The catalysts applied for the experiments comprise large amounts of vanadium pentoxide. This is an advantage for the conductivity experiments due to the lower resistivity of the samples. But with loadings above 30 m% there will be a vanadium pentoxide phase not in interaction with the support. This may influence the results of the conductivity experiments by changing the kinetic path from interface to bulk V_2O_5. Nevertheless, a support effect on the defect formation is found. The catalytic tests have also shown a support effect despite of the high loading. This can be explained by diffusion of gas molecules to the interface region that exhibits properties different from the pure vanadium pentoxide phase. But vanadium pentoxide is also in contact with the gas phase and contributes therefore to the reaction. Thus the determined propane activation energies do not reflect purely the interface properties.

4.3.2. Amorphous Monolayer Catalysts – Correlation to ODH

Figure 4-64 depicts the catalytic test results for the monolayer catalysts that were used to calculate the apparent propane activation energy E_a.
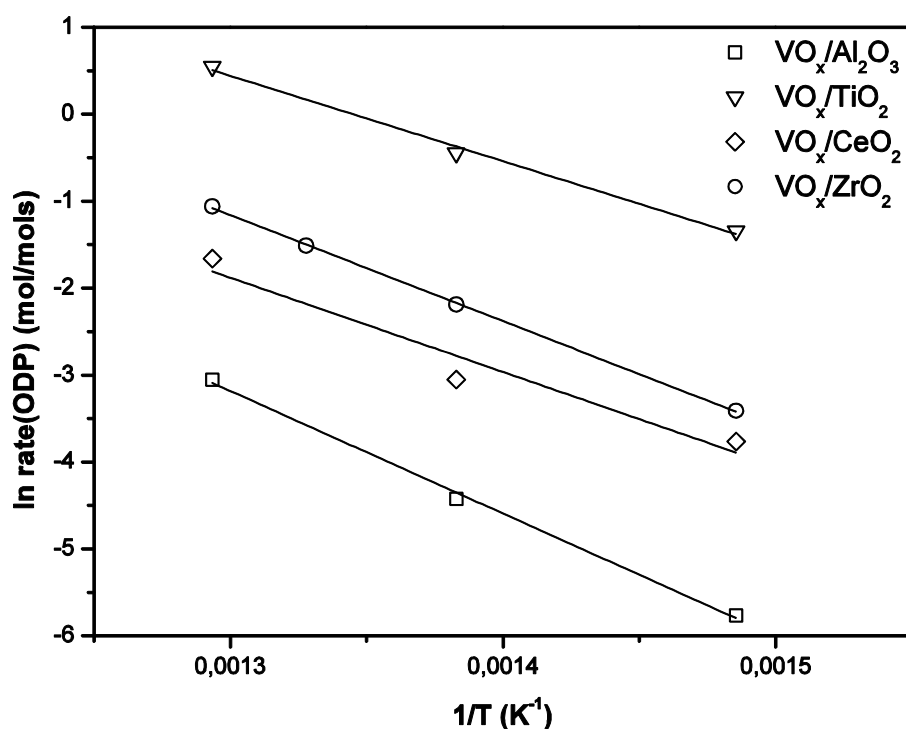
Figure 4-64: **Catalytic test results for the monolayer catalysts. Calculation of the propane actiation energy E_a from an Arrhenius plot of propane conversion X(propane) vs. temperature.**

Table 4-11 shows the porpane activation energies of the monolayer catalysts together with the defect formation enthalpies determined in Chapter 4.1.3.3.

Table 4-11: **Ethanol activation energies ΔE_a of the amorphous monolayer catalysts [89] and the defect formation enthalpies ΔH_f.**

	ΔE_a (kJmol^{-1})	ΔH_f (kJmol^{-1})
VO$_x$/TiO$_2$	66 ± 5	43 ± 10
VO$_x$/m-ZrO$_2$	80 ± 5	81 ± 6
VO$_x$/γ-Al$_2$O$_3$	91 ± 5	116 ± 10
V$_2$O$_5$	77 ± 5	119 ± 10

Figure 4-65 depicts the BEP correlation diagram for the propane activation energy and the defect formation enthalpy and for the supported catalysts a very good linear correlation with r = 0.999 is found. The deviation of the pure vanadium pentoxide might originate from the different experimental conditions for the defect formation enthalpies. The pure oxide was thermally reduced in oxygen but the monolayer catalysts needed a lower oxygen partial pressure for defect formation and were thus measured in nitrogen. The defect formation

enthalpy can be a function of partial pressure and thus the value for the pure vanadium pentoxide might deviate.
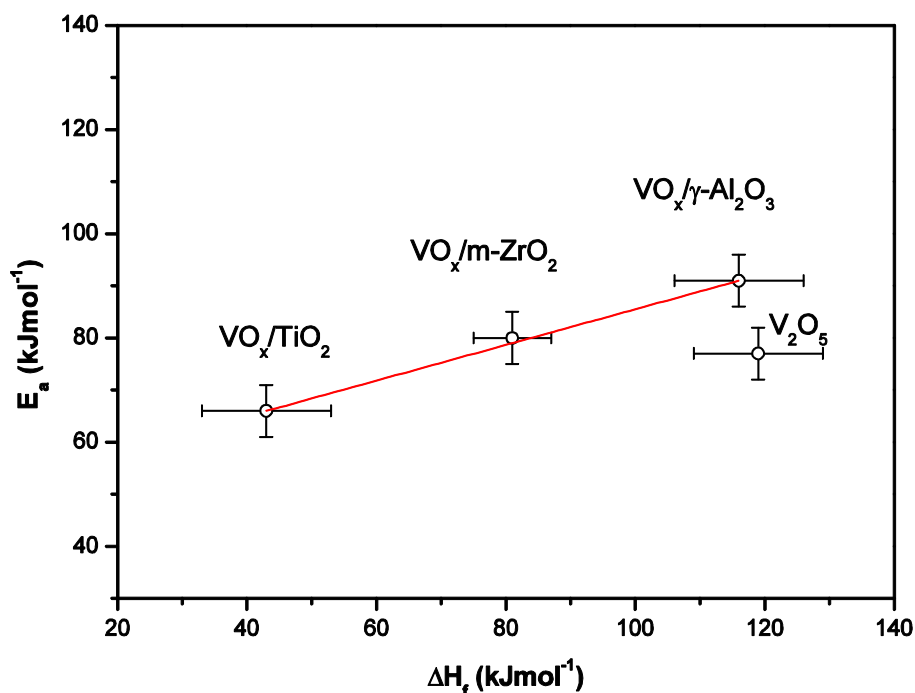
Figure 4-65: BEP correlation plot E_a and ΔH_f. **The supported catalysts give a very good correlation. The displacement of vanadium might originate in the different experimental conditions. The formation enthalpies of the monolayer catalysts were determined in nitrogen while the pure oxide was measured in oxgen.**

The correlation shows that the reducibility of the oxygen site has a direct connection to the catalytic reaction and can therefore be used as a reactivity descriptor. This connection is further discussed in the following chapter.

4.3.3. Defect Formation and ODH Reaction Profile

The oxidation step corresponds to the defect formation enthalpy. Thus, the higher the formation enthalpy the deeper the minimum in the energy profile and the higher the propane activation energy. This is observed in the correlation plot Figure 4-65 and is shown in the reaction energy profiles shown in Figure 4-66.

Figure 4-66: **Energy reaction profile for the ODP with the corresponding defect formation enthalpies. [89]**

These results indicate that the oxygen defect formation enthalpy is a suitable reactivity descriptor as proposed by Sauer et al. [13].

5. Summary and Conclusion

A reduction of polycrystalline vanadium pentoxide powder samples was observed under high oxygen partial pressure starting at 380 °C. RBS analysis and UV-Vis spectroscopy provides evidence for a reduction from V^{+5} to V^{+4}. It is possible to assign the reduction to the vanadyl oxygen site, as partial pre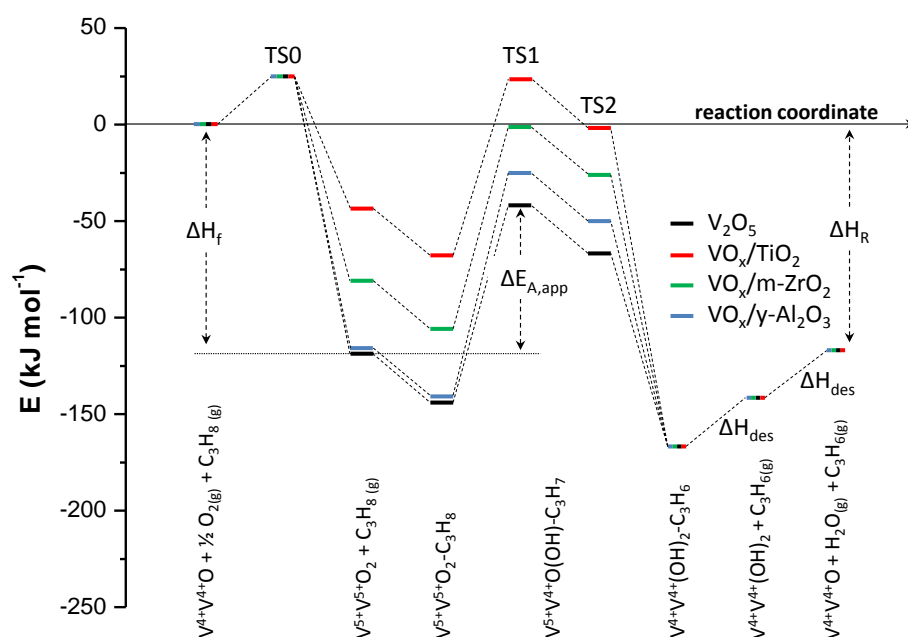ssure dependent XRD experiments at 500 °C revealed a lattice relaxation on vacancy formation in c-direction, which is in agreement with calculations done by [13]. The enthalpy to form the defect site is 1.3±0.1 eV. This value could be derived from the Arrhenius-plot using the activation energy on heating and cooling. Due to dissociation on heating and slow reoxidation on cooling, the energies for electron activation and vacancy formation could be separated.

The reducibility of the vanadyl oxygen site is a key feature for the catalytic activity and therefore the method was applied to metal oxide supported catalysts in order to investigate the "support effect" that enhances the catalytic performance. Making use of percolation effects in 2-phase mixtures, it was possible to show the importance of the interface between support and vanadium oxide that revealed a "support effect" on the transport properties. The conduction mechanism of vanadium pentoxide changes from electronic to ionic at the interface and the defect formation enthalpy is lowered. The presence of ionic and electronic transport is an important aspect, because for reduction and oxidation the catalyst needs to transport electrons. Moreover, it is assumed, that the reoxidation of the catalyst can occur at a different site than it was reduced [48] and via lattice diffusion oxygen is transported to the according site. This mechanism is supported by the presence of ionic conductivity.

In-situ neutron diffraction experiments gave evidence for a highly strained interface that is attributed to a thermal misfit between vanadium pentoxide and the supporting oxide. A highly disordered and defect rich micro-structure was found that itself can enhance the transport properties. Furthermore, the function of lattice strain as driving force for the formation of oxygen vacancies is discussed in connection to the chemical strain effect that can furthermore enhance the evolution of oxygen vacancies.

Well defined amorphous monolayer catalysts have been used for the correlation to catalytic properties. Compared to crystalline compounds the evolution of point defects starts at lower

oxygen partial pressure which is attributed to the presence of highly dispersed vanadium species. Correlation to the alkane activation energy for the ODH show that the defect formation enthalpy is a good reactivity descriptor and that the support influences the reducibility of the oxygen and hence the catalytic performance.

In order to gain further insight, future research should comprise modification of the catalyst's transport properties and investigation of the influence on the catalytic performance. Together with detailed micro-structural analysis this will give more information about the origin of the support effect. It will be necessary to develop new well defined sample geometries like meso-porous structures and coatings. These will facilitate the gas equilibration process and may therefore enhance the speed and accuracy of the experiments. Furthermore, the interface properties are very important and the influence of strain on the defect formation properties is a promising task.

6. References

[1] S. F. Hakonsen and A. Holmen, "Oxidative Dehydrogenation of Alkanes," in *Handbook of Heterogeneous Catalysis*, G. Ertl et al., Eds. Weinheim: Wiley-VCH Verlag GmbH & Co. KGaA, 2008, ch. 14.11.2, pp. 3384 - 3400.

[2] B. M. Weckhuysen and D. E. Keller, "Chemistry, spectroscopy and the role of supported vanadium oxides in heterogeneous catalysis," *Catalysis Today*, no. 78, pp. 25-46, 2003.

[3] G. C. Bond and F. Tahir, "Vanadium oxide Monolayer Catalysts Preparation, characterization and catalytic activity," *Applied Catalysis*, no. 71, pp. 1-31, 1991.

[4] A. Dinse, B. Frank, C. Hess, D. Habel, and R. Schomäcker, "Oxidative dehydrogenation of propane over low-loaded vanadia catalysts: Impact of the support material on kinetics and selectivity," *Journal of Molecular Catalysis A: Chemical*, no. 289, pp. 28-37, 2008.

[5] T. Blasco and J. M. López Nieto, "Oxidative dyhydrogenation of short chain alkanes on supported vanadium oxide catalysts," *Applied Catalysis A: General*, no. 157, pp. 117-142, 1997.

[6] P. Mars and D. W. van Krevelen, "Oxidations carried out by means of vanadium oxide catalysts," *Special Suppplement to Chemical Engineering Science*, no. 3, pp. 41-59, 1954.

[7] J. Haber, "Fundamentals of Hydrocarbon Oxidation," in *Handbook of Heterogeneous Catalysis*, G. Ertl et al., Eds. Weinheim: Wiley-VCH Verlag GmbH & Co. KGaA, 2008, ch. 14.11.1, p. 3367.

[8] G. Deo and I. E. Wachs, "Reactivity of Supported Vanadium Oxide Catalysts: The Partial Oxidation of Methanol," *Journal of Catalysis*, no. 146, pp. 323-334, 1994.

[9] I. E. Wachs, "Recent conceptual advances in the catalysis science of mixed metal oxide catalytic materials ," *Catalysis Today*, no. 100, pp. 79-94, 2005.

[10] M. A. Bañares, M. V. Martínez-Huerta, X. Gao, J. L. G. Fierro, and I. E. Wachs, "Dynamic behavior of supported vanadia catalysts in the selective oxidation of ethane: In situ Raman, UV–Vis DRS and reactivity studies," *Catalysis Today*, no. 61, pp. 295-301, 2000.

[11] A. Khodakov, B. Olthof, A. T. Bell, and E. Iglesia, "Structure and Catalytic Properties of Supported Vanadium Oxides: Support Effects on Oxidative Dehydrogenation

Reactions," *Journal of Catalysis*, no. 181, pp. 205-216, 1999.

[12] A. A. Lemonidou, L. Nalbandian, and I. A. Vasalos, "Oxidative dehydrogenation of propane over vanadium oxide based catalysts Effect of support and alkali promoter," *Catalysis Today*, no. 61, pp. 333-341, 2000.

[13] J. Sauer and J. Döbler, "Structure and reactivity of V2O5: bulk solid, nanosized clusters, species supported on silica and alumina, cluster cations and anions," *Dalton Transactions*, pp. 3116 - 3121, 2004.

[14] T. K. Todorova, M. V. Ganduglia-Pirovano, and J. Sauer, "Vanadium Oxides on Aluminum Oxide Supports. 1. Surface Termination and Reducibility of Vanadia Films on α-Al2O3(0001)," *The Journal of Physical Chemistry B*, no. 109, pp. 23523–23531, 2005.

[15] V. Brázdová, M. V. Ganduglia-Pirovano, and J. Sauer, "Vanadium Oxides on Aluminum Oxide Supports. 2. Structure, Vibrational Properties, and Reducibility of V2O5 Clusters on r-Al2O3(0001)," *The Journal of Physical Chemistry B*, no. 109, pp. 23532-23542, 2005.

[16] T. K. Todorova, M. V. Ganduglia-Pirovano, and J. Sauer, "Vanadium Oxides on Aluminum Oxide Supports. 3. Metastable K-Al2O3(001) Compared to a-Al2O3(0001)," *The Journal of Physical Chemistry C*, no. 111, pp. 5141-5153, 2007.

[17] R. Fortrie, T. K. Todorova, M. V. Ganduglia-Pirovano, and J. Sauer, "Nonuniform temperature dependence of the reactivity of disordered VOx / k-Al2O3(001) surfaces: A density functional theory based Monte Carlo study," *The Journal of Chemical Physics*, no. 129, p. 224710, 2008.

[18] V. Brázdová, M. V. Ganduglia-Pirovano, and J. Sauer, "Vanadia Aggregates on an Ultrathin Aluminum Oxide Film on NiAl(110)," *The Journal of Physical Chemistry C*, no. 114, pp. 4983-4994, 2010.

[19] M. V. Ganduglia-Pirovano et al., "Role of Ceria in Oxidative Dehydrogenation on Supported Vanadia Catalyst," *Journal of the American Chemical Society*, no. 131, pp. 2345-2349, 2010.

[20] R. J. Brook, "Defect Structure of Ceramic Materials," in *Electrical Conductivity in Ceramics and Glass*, N. M. Tallan, Ed. New York: Marcel Dekker, INC., 1974, ch. 3, pp. 179-266.

[21] P. Knauth and H. L. Tuller, "Solid-State Ionics: Roots, Status, and Future Prospects,"

Journal of the American Ceramic Society, no. 85, pp. 1654-1680, 2002.

[22] H. Schmalzried, "Ionen- und Elektronenleitung in binären Oxiden und ihre Untersuchung mittels EMK-Messungen," *Zeitschrift für Physikalische Chemie*, no. 38, pp. 87-102, 1963.

[23] E. C. Subbarao and H. S. Maiti, "Solid Electrolytes with Oxygen Ion Conduction," *Solid State Ionics*, no. 11, pp. 317-338, 1984.

[24] D. L. Douglass and C. Wagner, "The Oxidation of Oxygen-Deficient Zirconia and Its Relationship to the Oxidation of Zirconium," *Journal of The Electrochemical Society*, no. 113, pp. 671-676, 1966.

[25] A. Kumar, D. Rajdev, and D. L. Douglass, "Effect of Oxide Defect Structure on the Electrical Properties of ZrO2," *Journal of the American Ceramic Society*, no. 55, pp. 439-445, 1972.

[26] F. A. Kröger, "Electronic Conductivity of Calcia-Stabilized Zirconia," *Journal of the American Ceramic Society*, no. 49, pp. 215-218, 1966.

[27] F. A. Kröger and H. J. Vink, *Solid State Physics*, F. Seitz and D. Turnbull, Eds. New York: Academic Press , 1956, p. 310.

[28] H. Rickert, *Electrochemistry of Solids*. Berlin: Springer-Verlag, 1982.

[29] M. F. Lasker and R. A. Rapp, "Mixed Conduction in ThO2 and Tho2-Y2O3 Solutions," *Zeitschrift für Physikalische Chemie Neue Folge*, no. 49, pp. 198-221, 1966.

[30] J. Maier, *Festkörper - Fehler und Funktion*, C. Elschenbroich, F. Hensel, and H. Hopf, Eds. Leipzig: Teubner Studienbücher Chemie, 2000.

[31] E. Barsoukov and J. R. Macdonald, Eds., *Impedance Spectroscopy Theory, Experiment, and Applications*, 2nd ed.: John Wiley & Sons Inc., 2005.

[32] J. R. MacDonald, "Note on the Parameterization of the Constant-Phase Admittance Element," *Solid State Ionics*, no. 13, pp. 147-149, 1983.

[33] R. L. Hurt and J. R. Macdonald, "Distributed circuit elements in impedance spectroscopy: A unified treatment of conductive and dielectric systems," *Solid State Ionics*, no. 20, pp. 111-124, 1986.

[34] R. Enjalbert and J. Galy, "A Refinement of the Structure of V2O5," *Acta Crystallographica*, vol. C42, pp. 1467-1469, 1986.

[35] J. H. Perlstein, "A dislocation model for two-level electron-hopping conductivity in V2O5: Implications for catalysis," *Journal of Solid State Chemistry*, no. 3, pp. 217-226, 1971.

[36] D. S. Volzhenskii and M. V. Pashkovskii, "Conduction Mechanism in Vanadium Pentoxide," *Soviet Physics-Solid State*, no. 11, pp. 950-953, 1969.

[37] V. A. Ioffe and I. B. Patrina, "Comparison of the Small-Polaron Theory with the Experimental Data of Current Transport in V2O5," *Physica Status Solidi*, no. 40, pp. 389-395, 1970.

[38] P. Nagels and M. Denayer, "Electronic Conduction in V2O5 Single Crystals," in *Proceedings of the Tenth International Conference on the Physics of Semiconductors*, 1970, pp. 321-327.

[39] J. Haemers, E. Baetens, and J. Vennik, "On the Electrical Conductivity of V2O5 Single Crystals," *Physica Status Solidi (a)*, no. 20, pp. 381-386, 1973.

[40] C. Sanchez, M. Henry, J. C. Grenet, and J. Livage, "Free and bound polarons in vanadium pentoxide," *Journal of Physics C: Solid State Physics*, no. 15, pp. 7133-7141, 1982.

[41] S. Kachi, T. Takada, and K. Kosuge, "Electrical Conductivity of Vanadium Oxides," *Journal of the Physical Society of Japan*, no. 18, pp. 1839-1840, 1963.

[42] I. B. Patrina and V. A. Ioffe, "Electrical Properties of Vanadium Pentoxide," *Soviet Physics-Solid State*, no. 18, pp. 2581-2585, 1965.

[43] T. Allersma, R. Hakim, T. N. Kennedy, and J. D. Mackenzie, "Structure and Physical Properties of Solid and Liquid Vanadium Pentoxide," *Journal of Chemical Physics*, no. 46, pp. 154-160, 1967.

[44] J. Nováková, "Isotopic Exchange of Oxygen 18O Between the Gaseous Phase and Oxide Catalysts," *Catalysis Reviews - Science and Engineering*, no. 4, pp. 77-113, 1971.

[45] J. Haber, M. Witko, and R. Tokarz, "Vanadium pentoxide I. Structures and properties," *Applied Catalysis A: General*, no. 157, pp. 3-22, 1997.

[46] T. S. Zolyan and A. R. Regel, "Electrical conductivity and thermo-emf of solid and liquid vanadium pentoxide," *Soviet Physics-Solid State*, no. 6, p. 1189, 1964.

[47] G. L. Simard, J. F. Steger, and R. J. Arnott, "Vanadium Oxides as Oxidation Catalysts,"

Industrial and Engineering Chemistry, no. 47, pp. 1424-30, 1955.

[48] J. Haber, "Fundamentals of Hydrocarbon Oxidation," in *Handbook of Heterogeneous Catalysis*, G. Ertl et al., Eds. Weinheim: Wiley-VCH Verlag GmbH & Co. KGaA, 2008, ch. 14.11.1, p. 3364.

[49] I. E. Wachs, "Raman and IR studies of surface metal oxide species on oxide supports: Supported metal oxide catalysts," *Catalysis Today*, no. 27, pp. 437-455, 1996.

[50] F. Arena, F. Frusteri, and A. Parmaliana, "Structure and dispersion of supported-vanadia catalysts. Influence of the oxide carrier," *Applied Catalysis A: General*, no. 176, pp. 189-199, 1999.

[51] H. Tian, E. I. Ross, and I. E. Wachs, "Quantitative Determination of the Speciation of Surface Vanadium Oxides and Their Catalytic Activity," *Journal of Physical Chemistry B*, no. 110, pp. 9593–9600, 2006.

[52] Y.-M. Liu et al., "Highly efficient VOx/SBA-15 mesoporous catalysts for oxidative dehydrogenation of propane," *Chemical Communications*, pp. 2832-2833, 2002.

[53] Y.M. Liu et al., "Vanadium oxide supported on mesoporous SBA-15 as highly selective catalysts in the oxidative dehydrogenation of propane," *Journal of Catalysis*, no. 224, pp. 417-428, 2004.

[54] P. Gruene, T. Wolfram, K. Pelzer, R. Schlögl, and A. Trunschke, "Role of dispersion of vanadia on SBA-15 in the oxidative dehydrogenation of propane ," *Catalysis Today*, no. 157, pp. 137-142, 2010.

[55] P. Kuśtrowski et al., "VOx supported SBA-15 catalysts for the oxidative dehydrogenation of ethylbenzene to styrene in the presence of N2O," *Catalysis Today*, no. 114, pp. 307-313, 2006.

[56] G. Martra, F. Arena, S. Coluccia, F. Frusteri, and A. Parmaliana, "Factors controlling the selectivity of V2O5 supported catalysts in the oxidative dehydrogenation of propane," *Catalysis Today*, no. 63, pp. 197-207, 2000.

[57] N. Magg et al., "Vibrational spectra of alumina- and silica-supported vanadia revisited: An experimental and theoretical model catalyst study," *Journal of Catalysis*, no. 226, pp. 88-100, 2004.

[58] M. Baltes et al., "MCM-48-Supported Vanadium Oxide Catalysts, Prepared by the

Molecular Designed Dispersion of VO(acac)2: A Detailed Study of the Highly Reactive MCM-48 Surface and the Structure and Activity of the Deposited Vox," *Journal of Catalysis*, no. 197, pp. 160-171, 2001.

[59] C. Hess, "Characterization of the synthesis and reactivity behavior of nanostructured vanadia model catalysts using XPS and vibrational spectroscopy," no. 600, pp. 3695-3701, 2006.

[60] P. R. Shah, J. M. Vohs, and R. J. Gorte, "Probing the Effect of Local Structure on the Thermodynamic Redox Properties of V+5: A Comparison of V2O5 and Mg3(VO4)2," *Journal of Physical Chemistry B*, no. 111, pp. 5680–5683, 2007.

[61] P. R. Shah, M. M. Khader, J. M. Vohs, and R. J. Gorte, "A Comparison of the Redox Properties of Vanadia-Based Mixed Oxides," *Journal of Physical Chemistry C*, no. 112, pp. 2613–2617, 2008.

[62] P. R. Shah, I. Baldychev, J. M. Vohs, and R. J. Gorte, "Comparison of redox isotherms for vanadia supported on zirconia and titania," *Applied Catalysis A: General*, vol. , no. 361, pp. 13-17, 2009.

[63] I. Baldychev, R. J. Gorte, and J. M. Vohs, "The impact of redox properties on the reactivity of V2O5/Al2O3 catalysts," *Journal of Catalysis*, no. 269, pp. 397-403, 2010.

[64] I. Baldychev, J. M. Vohs, and R. J. Gorte, "The effect of support on redox properties and methanol-oxidation activity of vanadia catalysts," *Applied Catalysis A: General*, no. 391, pp. 86-91, 2011.

[65] R. Mitdank et al., "Ion beam analysis of a structural phase transition in porous TiO2/V2O5 ceramics with rough surfaces," *Nuclear Instruments and Methods in Physics Research Section B: Beam Interactions with Materials and Atoms*, no. 269, pp. 345-352, 2011.

[66] J. Boros, "Elektrische und optische Eigenschaften von Vanadiumpentoxyd-Kristallen," *Zeitschrift für Physik A: Atoms and Nuclei*, no. 126, pp. 721-724, 1949.

[67] J. T. S. Irvine, D. C. Sinclair, and A. R. West, "Electroceramics: Characterization by Impedance Spectroscopy," *Advanced Materials*, no. 2, pp. 132-138, 1990.

[68] C. Wang, Y. Cai, and I. E. Wachs, "Reaction-Induced Spreading of Metal Oxides onto Surfaces of Oxide Supports during Alcohol Oxidation: Phenomenon, Nature, and Mechanisms," *Langmuir*, no. 15, pp. 1223-1235, 1999.

[69] P. Boch and J.-C. Niepce, *Ceramic Materials: processes, properties and applications*. London: ISTE, 2007.

[70] R. Merkle and J. Maier, "On the Tammann-Rule," *Zeitschrift für anorganische und allgemeine Chemie*, no. 631, pp. 1163-1166, 2005.

[71] P. Clauws and J. Vennik, "Opcital Absorption of Defects in V2O5 Single Crystals: As-Grown and Reduced V2O5," *Physica Status Solidi*, no. 66, pp. 553-560, 1974.

[72] L. Fiermans, P. Clauws, W. Lambrecht, L. Vandenbroucke, and J. Vennik, "Single Crystal V2O5 and Lower Oxides: A Survey of Their Electronic, Optical, Structural, and Surface Properties," *Physica Status Solidi (a)*, no. 59, pp. 485-504, 1980.

[73] J. Goclon, R. Grybos, M. Witko, and J. Hafner, "Oxygen vacancy formation on clean and hydroxylated low-index V2O5 surfaces: A density functional investigation," *Physical Review B*, no. 79, p. 075439, 2009.

[74] J. B. MacChesney and H. J. Guggenheim, "Growth and electrical properties of vanadium dioxide single crystals containing selected impurity ions," *Journal of Physics and Chemistry of Solids*, no. 30, pp. 225-234, 1969.

[75] M. Benmoussa, E. Ibnouelghazi, A. Bennouna, and E. L. Ameziane, "Structural, electrical and optical properties of sputtered vanadium pentoxide thin films," *Thin Solid Films*, no. 265, pp. 22-28, 1995.

[76] I. E. Wachs, L. E. Briand, J.-M. Jehng, L. Burcham, and X. Gao, "Molecular structure and reactivity of the group V metal oxides," *Catalysis Today*, no. 57, pp. 323-330, 2000.

[77] W. Lambrecht et al., "The energy band structure of V2o5: II. Analysis of the theoretical results and comparison with experimental data," *Journal of Physics C: Solid State Physics*, no. 13, pp. 2503-2517, 1980.

[78] C. V. Ramana, O. M. Hussain, B. Srinivasulu Naidu, and P. J. Reddy, "Spectroscopic characterization of electron-beam evaporated V2O5 thin films," *Thin Solid Films*, no. 305, pp. 219-226, 1997.

[79] F. Vratn and F. Micale, "Reflectance Spectra of Non-Stoichiometric Titanium Oxide, Niobium Oxide, and Vanadium Oxide," *Transactions of the Faraday Society*, no. 59, pp. 2739-2749, 1963.

[80] M. V. Ganduglia-Pirovano, A. Hofmann, and J. Sauer, "Oxygen vacancies in transition

metal and rare earth oxides: Current state of understanding and remaining challenges," *Surface Science Reports*, no. 62, pp. 219-270, 2007.

[81] G. C. Bond, "Supported Metal Catalysts: Some Unsolved Problems," *Chemical Society Reviews*, no. 20, pp. 441-475, 1991.

[82] D. C. Sayle, S. C. Parker, and J. H. Harding, "Calculated defect formation energies as a function of distance from the BaO/MgO interface compared with image theory predictions," *Philosophical Magazine A*, no. 69, pp. 787-792, 1994.

[83] D. C. Sayle, C. R. A. Catlow, M.-A. Perrin, and P. Nortier, "Computer Modeling of the V2O5/TiO2 Interface," *Journal of Physical Chemistry*, no. 100, pp. 8940-8945, 1996.

[84] A. Said and M. El-Wahab, "Structures accompanying the solid-solid interactions in the V2O5-MgO system," *Thermochimica Acta*, no. 249, pp. 313-323, 1995.

[85] A. Said and M. El-Wahab, "Oxidative Dehydrogenation of Ethyl Alcohol over Vanadium Pentoxide Supported on Magnesia," *Journal of Chemical Technology and Biotechnology* , no. 63, pp. 78-84, 1995.

[86] D. Habel et al., "Phase development in the catalytic system V2O5/TiO2 under oxidising conditions," *Journal of the European Ceramic Society*, no. 26, pp. 3287-3294, 2006.

[87] J. H. Kim and G. M. Choi, "Mixed ionic and electronic conductivity of [(ZrO2)0.92(Y2O3)0.08]1−y·(MnO1.5)y," *Solid State Ionics*, no. 130, pp. 157-168, 2000.

[88] N. Steinfeldt, D. Müller, and H. Berndt, "VOx species on alumina at high vanadia loadings and calcination temperature and their role in the ODP reaction," *Applied Catalysis A: General*, no. 272, pp. 201-213, 2004.

[89] B. Beck et al., "Scaling relations in the partial oxidation of ethanol on vanadia based catalysts," *to be published*.

[90] N. Barsan and U. Weimar, "Conduction Model of Metal Oxide Gas Sensors," *Journal of Electroceramics*, no. 7, pp. 143-211, 2001.

[91] A. Dinse, A. Ozarowski, C. Hess, R. Schomäcker, and K.-P. Dinse, "Potential of High-Frequency EPR for Investigation of Supported Vanadium Oxide Catalysts," *Journal of Physical Chemistry C*, no. 112, pp. 17664-17671, 2008.

[92] J. Maier, "Heterogeneous Solid Electrolytes," in *Recent Trends in Superionic Solids and Solid Electrolytes*, A. L. Laskar and S. Chandra, Eds. New York: Academic Press, 1989,

pp. 137-184.

[93] D. Habel et al., "Micro straining in titania-, alumina- and silica- supported v2o5-catalysts," *Journal of the European Ceramic Society*, no. 29, pp. 1093-1099, 2009.

[94] M. V. Ganduglia-Pirovano and J. Sauer, "Stability of reduced V2O5(001) surfaces," *Physical Review B*, no. 70, p. 045422, 2004.

[95] D. Habel et al., "Micro straining in titania-, alumina- and silica- supported v2o5-catalysts," *Journal of the European Ceramic Society*, no. 29, pp. 1093-1099, 2009.

[96] M. Greenberg, E. Wachtel, I. Lubomirsky, J. Fleig, and J. Maier, "Elasticity of Solids with a Large Concentration of Point Defects," *Advanced Functional Materials*, no. 16, pp. 48-52, 2006.

[97] I. Lubomirsky, "Mechanical properties and defect chemistry," *Solid State Ionics*, no. 177, pp. 1639-1642, 2006.

[98] A. Kossoy, Y. Feldman, E. Wachtel, I. Lubomirsky, and J. Maier, "Elasticity of solids with a large concentration of point defects II. The chemical strain effect in Ce0.8Gd0.2O1.9," *Advanced Functional Materials*, no. 17, pp. 2393-2398, 2007.

[99] I. Lubomirsky, "Stress adaptation in ceramic thin films," *Physical Chemistry Chemical Physics*, no. 9, pp. 3701-3710, 2007.

[100] I. Lubomirsky, "Practical applications of the chemical strain effect in ionic and mixed conductors," *Monatshefte für Chemie*, no. 140, pp. 1025-1030, 2009.

[101] A. Kossoy et al., "On the origin of the lattice constant anomaly in nanocrystalline ceria," *Physical Chemistry Chemical Physics*, no. 8, pp. 1111-1115, 2006.

[102] S. J. Hong and A. V. Virkar, "Lattice Parameters and Densities of Rare-Earth Oxide Doped Ceria Electrolytes," *Journal of the American Ceramic Society*, no. 78, pp. 433-439, 1995.

[103] A. Atkinson and T. M. G. M. Ramos, "Chemically-induced stresses in ceramic oxygen ion-conducting membranes," *Solid State Ionics*, no. 129, pp. 259-269, 2000.

[104] S. Wang, M. Katsuki, T. Hashimoto, and M. Dokiya, "Expansion Behavior of Ce1–yGdyO2.0–0.5y–delta under Various Oxygen Partial Pressures Evaluated by HTXRD," *Journal of the Electrochemical Society*, no. 150, pp. A952-A958, 2003.

[105] A. Kossoy et al., "Influence of Point-Defect Reaction Kinetics on the Lattice Parameter

of Ce0.8Gd0.2O1.9," *Advanced Functional Materials*, no. 19, pp. 634–641, 2009.

[106] A. Vojvodic et al., "On the behavior of Bronsted-Evans-Polanyi relations for transition metal oxides," *The Journal of Chemical Physics*, no. 134, p. 244509, 2011.

[107] R. K. Grasselli, "Fundamental Principles of Selective Heterogeneous Oxidation Catalysis," *Topics in Catalysis*, no. 21, pp. 79-88, 2002.

[108] J. M. López Nieto, "The selective oxidative activation of light alkanes. From supported vanadia to multicomponent bulk V-containing catalysts," *Topics in Catalysis*, no. 41, pp. 3-15, 2006.

[109] O. Ovsitser, M. Cherian, and E. V. Kondratenko, "In-Situ UV/vis and Transient Isotopic Analysis of the Role of Oxidizing Agent in the Oxidative Dehydrogenation of Propane over Silica-Supported Vanadia Catalysts," *The Journal of Physical Chemistry C*, no. 111, pp. 8594–8602, 2007.
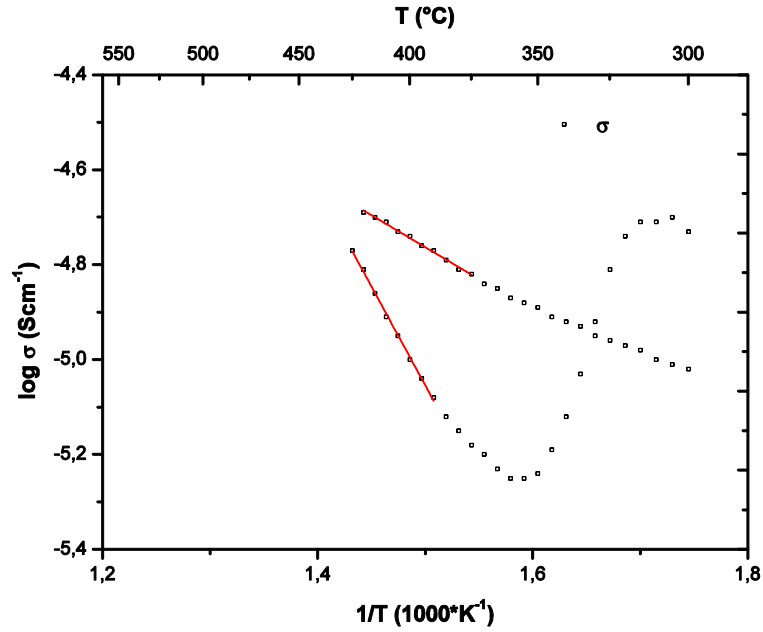
7. Appendix

Figure 7-1: Conductivity of VO_x/MgO. The experiment was conducted below the transition temperature to spinel phases in order to investigate the influence of phase transition on the defect formation enthalpy.

Table 7-1: Fit parameter of VO_x/m-ZrO_2 in oxygen and nitrogen.

	Oxygen				Nitrogen		
	Value	Error	Unit		Value	Error	Unit
R_1	5,80E+06	1,71E+05	Ω	R_1	2,80E+05	8,77E+03	Ω
C_1	4.39E-10	± 3.55E-11	F	C_1	4,59E-10	2,11E-10	F
m_1	9,38E-01	1,38E-02	a.u.	m_1	9,42E-01	5,18E-02	a.u.
R_2	5,32E+06	2,20E+06	Ω	R_2	3,08E+05	9,15E+03	Ω
C_2	8,23E-08	1,19E-08	F	C_2	7,17E-09	4,13E-10	F
m_2	6,29E-01	8,11E-02	a.u.	m_2	1,02E+00	1,49E-02	a.u.
R_3	4,98E+07	4,35E+07	Ω	R_3	-	-	-
C_3	4,44E-07	2,44E-07	F	C_3	-	-	-
m_3	4,89E-01	1,43E-01	a.u.	m_3	-	-	-

Table 7-2: Fit parameter of $VO_x/\gamma-Al_2O_3$ in oxygen and nitrogen.

	Oxygen				Nitrogen		
	Value	Error	Unit		Value	Error	Unit
R_1	1,85E+07	5,18E+05	Ω	R_1	1,02E+09	2,06E+07	Ω
C_1	2,45E-10	1,54E-11	F	C_1	2,52E-10	2,26E-12	F
m_1	1,03E+00	1,37E-02	a.u.	m_1	1,00E+00	7,41E-03	a.u.
R_2	2,22E+07	7,50E+05	Ω	R_2	2,25E+08	4,29E+07	Ω
C_2	5,53E-09	1,48E-10	F	C_2	2,21E-08	9,03E-09	F
m_2	9,34E-01	1,84E-02	a.u.	m_2	6,18E-01	9,12E-02	a.u.
R_3	5,00E+08	3,40E+10	Ω	R_3	-	-	-
C_3	6,80E-07	2,77E-07	F	C_3	-	-	-
m_3	2,66E-01	7,15E-02	a.u.	m_3	-	-	-

Table 7-3: Fit parameter of VO_x/TiO_2 in oxygen and nitrogen.

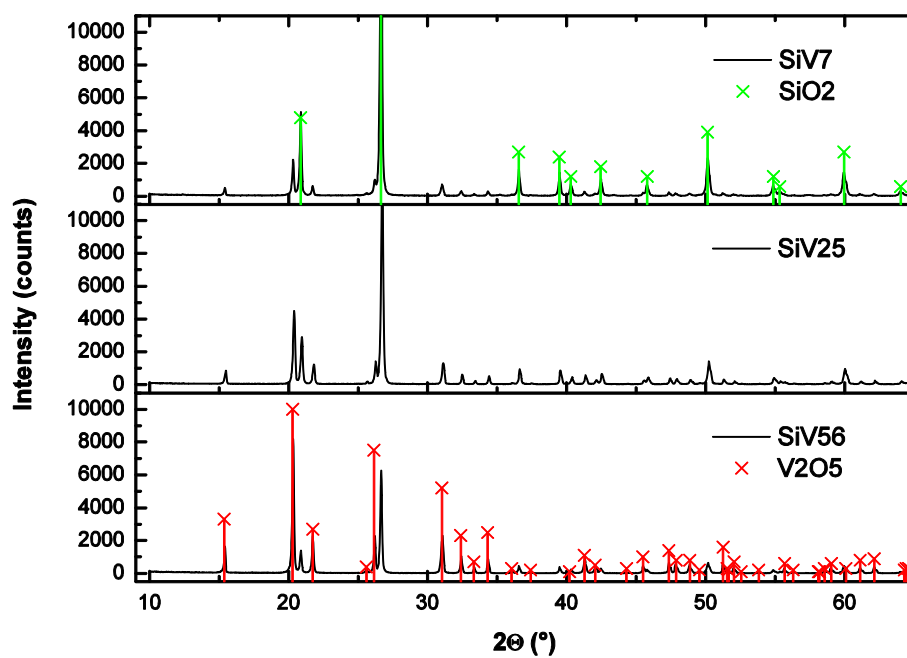|	Oxygen				Nitrogen		
	Value	Error	Unit		Value	Error	Unit
R_1	1,22E+06	1,76E+04	Ω	R_1	1,42E+06	2,23E+04	Ω
C_1	3,09E-10	4,74E-11	F	C_1	2,56E-10	1,28E-11	F
m_1	9,84E-01	1,93E-02	a.u.	m_1	1,00E+00	8,81E-03	a.u.
R_2	1,61E+06	2,49E+04	Ω	R_2	-	-	-
C_2	4,89E-08	2,22E-09	F	C_2	-	-	-
m_2	9,25E-01	1,72E-02	a.u.	m_2	-	-	-

Figure 7-2: XRD phase analysis of VO$_x$/SiO$_2$ catalysts. No global phase transition is observed.
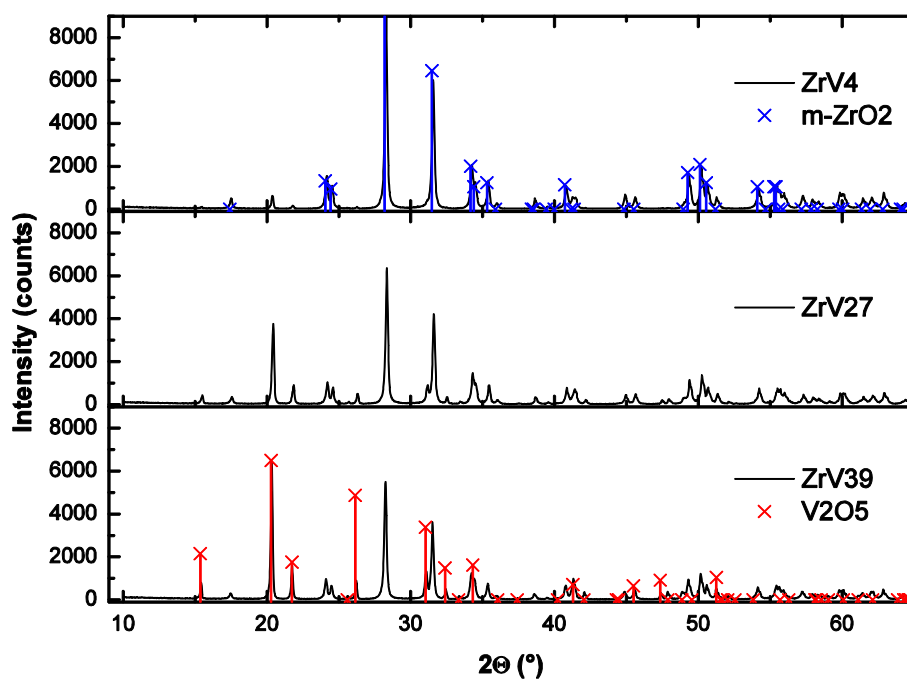

Figure 7-3: XRD phase analysis of VO$_x$/ZrO$_2$ catalysts. No global phase transition is observed.
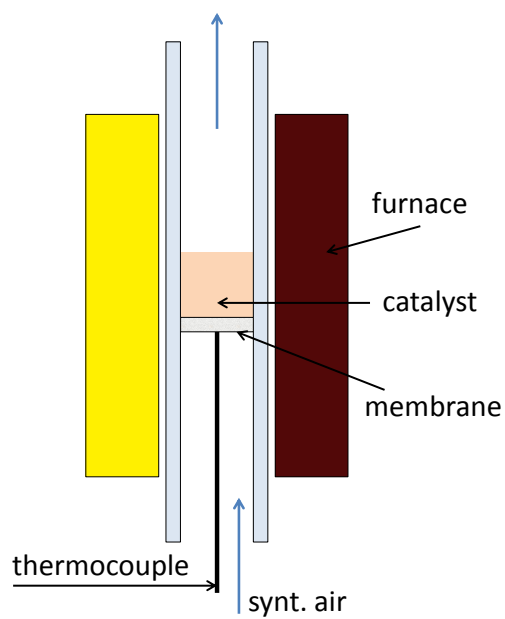
Figure 7-4: Calcination furnace. A setpoint temperature of 427 °C gives a temperature at the sample of 500 °C.